TRANSFER PROCESSES ACROSS THE FREE WATER SURFACE

als Habilitationsschrift

zur Erlangung der venia legendi

der

Fakultät für Physik und Astronomie

der Ruprecht-Karls-Universität Heidelberg

vorgelegt von

Bernd Jähne

aus Pirmasens

1985

doi: 10.5281/zenodo.12202

CONTENTS

1. INTRODUCTION

Such different quantities like momentum, energy, sensible and latent heat, and mass are involved in exchange processes between the gaseous and liquid phase. They are an ubiquitous phenomenon in our world. On the one hand, we have the complex field of air-sea interactions being of central importance for global climate and mass cycling. On a smaller scale, similar processes occure in lakes and rivers. On the other hand, gas-liquid exchange processes are widely used in technical and chemical engineering.

Momentum, energy, heat, and mass, all these quantities, can be transported both by turbulent and by molecular mechanisms. Besides strongly stratified systems, the turbulent transport exceeds the molecular by several orders of magnitude. But this condition changes near the surface. Turbulent motions cannot penetrate the interface, they can only approach it and are attenuated by viscous forces. So the turbulent transport gradually decreases towards the surface and there is a layer at the surface in which molecular diffusion will exceed the effect of turbulent transport. The thickness of this layer depends on the diffusion coefficient and the intensity of the turbulent motions at the very surface and is roughly in the order of 10 μm to 10 mm.

Because of the decrease of the turbulence intensity towards the surface, the transport resistance is concentrated at the surface. Again, the value of the diffusion coefficient of the tracer controls the extent to which the resistance is concentrated at the surface.

In any case, the interaction of turbulent and molecular diffusion critically determines the transfer across interfaces. This thesis discusses the interaction of turbulent and molecular transport at the very surface. Despite the widespread importance of the process and the large number of experimental and theoretical investigations a deeper knowledge of the physics of this process is still lacking.

On the one hand, this is due to the complex coupling of the transfer processes at a free surface. It can easily be imagined that at a rigid surface there must be a strong analogy between all exchange processes. The velocity shear is the source for the turbulence; buoyancy forces

act as additional sources or as a sink. The turbulence adjusts itself so that an equilibrium between these forces is achieved. For a given boundary condition (i.e. surface roughness, velocity and density gradients), the fluxes for all exchange processes are fixed.

At a free surface the situation is much more complex, since the exchange processes now cause changes in the structure of the surface. Wind blowing over the surface or turbulent eddies moving towards the water surface can generate surface waves. These surface motions provide an additional degree of freedom for a free surface compared to a rigid surface. So the turbulent wind field over the water surface puts energy not only into the mean water velocity by shear stress, but also into the waves. This energy input triggers a complex additional energy cycling: Energy is carried away with the group velocity of the wave field. By nonlinear wave-wave interaction energy is exchanged between different wave components. Finally, steep waves become instable and produce near-surface turbulence.

It is a trivial fact to any observer of the sea state that the wave field is not only a function of the wind speed, but also of the fetch and the duration of the wind. If we further consider that the wave generation, amplification, and attenuation is critically influenced by monomolecular films on the water surface, we get an idea how many parameters influence this complex system.

It is even more complex, since the wave field reacts upon the air flow. Small scale ripples increase the surface roughness and enhance the momentum transfer into the water. Steep gravity waves cause flow separation in the air flow. So the exchange processes are coupled in a complicated manner.

It is far beyond the scope of this thesis to analyse this complex system in detail. Our point of view rather shall be the near-surface turbulence finally resulting from all these processes. The transfer processes across the boundary layer on the water side will reflect its structure and intensity. We therefore pursue the idea to use the transfer as a monitoring device for this turbulence.

It can easily be imagined that it is very difficult to investigate experimentally such thin layers at a free moving surface. This is an-

other reason why the knowledge about the transfer processes at free surfaces is so poor. This lack of detailed experimental information, on the other side, has hindered the development of theory considerably and has led to the unpleasant situation that many speculative papers have been published.

The study of the exchange processes is a typical bordering field between many sciences in view of the various parameters involved and the quite different systems in which they take place: hydrodynamics, oceanography (small scale air-sea interaction), micro meteorology, limnology, and environmental, chemical and biochemical engineering. Deplorably, the knowledge often evolves independently and without much interchange, especially in the more applied engineering sciences and in the more theoretical and basis-orientated sciences, despite the fact that there are so many similarities between the technical and the natural systems. I therefore shall try to identify these connections at several points.

It has just been the joint consideration of the various aspects of the problem that stimulated considerable progress. After some basic considerations und the discussion of the state of the art, the thread through this thesis will be the description of new experimental methods carrying to a deeper insight into the structure of the near-surface water turbulence in conjunction with the corresponding theoretical considerations.

2. BASIC CONSIDERATIONS

2.1 The transport equations

Unsteady diffusive transport of a scalar tracer like mass or heat is described by Fick's second law

$$\frac{dc}{dt} = \frac{\partial c}{\partial t} + \underline{u}\nabla c = \nabla j = D\Delta c \qquad (2.1)$$

where D is the molecular diffusion coefficient of the tracer; vectors are underlined. For heat the concentration is given by $\varrho c_p T$ and the diffusion coefficient D_H is $\lambda/\varrho c_p$, where c_p, ϱ, and λ are the specific heat, density, and thermal conductivity respectively. The turbulent transport is included in the term $\underline{u}\nabla c$. The turbulent velocity field is a solution of the Navier-Stokes' differential equation, which for a incompressible liquid reads

$$\frac{\partial \underline{u}}{\partial t} + (\underline{u}\nabla)\underline{u} = f - \frac{1}{\varrho}\nabla p + \nu\Delta\underline{u} \qquad (2.2)$$

The right hand side of the equation contains the accelerations caused by external force densities f, pressure gradients, or viscous shear forces. The equations for a passive tracer and for momentum are quite similar. But there is one basic difference: The transport equation for a tracer is linear in the concentration, whereas in the momentum equation there is a nonlinear term in $\underline{u}$, since the transported tracer is the velocity itself. The importance of this term can be seen from the equations for the mean values in a turbulent field. These equations can be derived from (2.1) and (2.2) by splitting into a mean and a fluctuating component

$$\underline{u} = \underline{U} + \underline{u}' \quad c = C + c', \qquad (2.3)$$

where large and primed letters denote the mean and fluctuating component respectively. For case of flow into x-direction on both sides of an interface the mean components in y and z direction, V and W, are zero (surface lying in the x,y-plane) and the velocity component in x-direction, U, depends only on z

Figure 2.1: Schematic graph of the mass boundary layers on both sides of a gas-liquid interface for a tracer solubility $\alpha = 3$

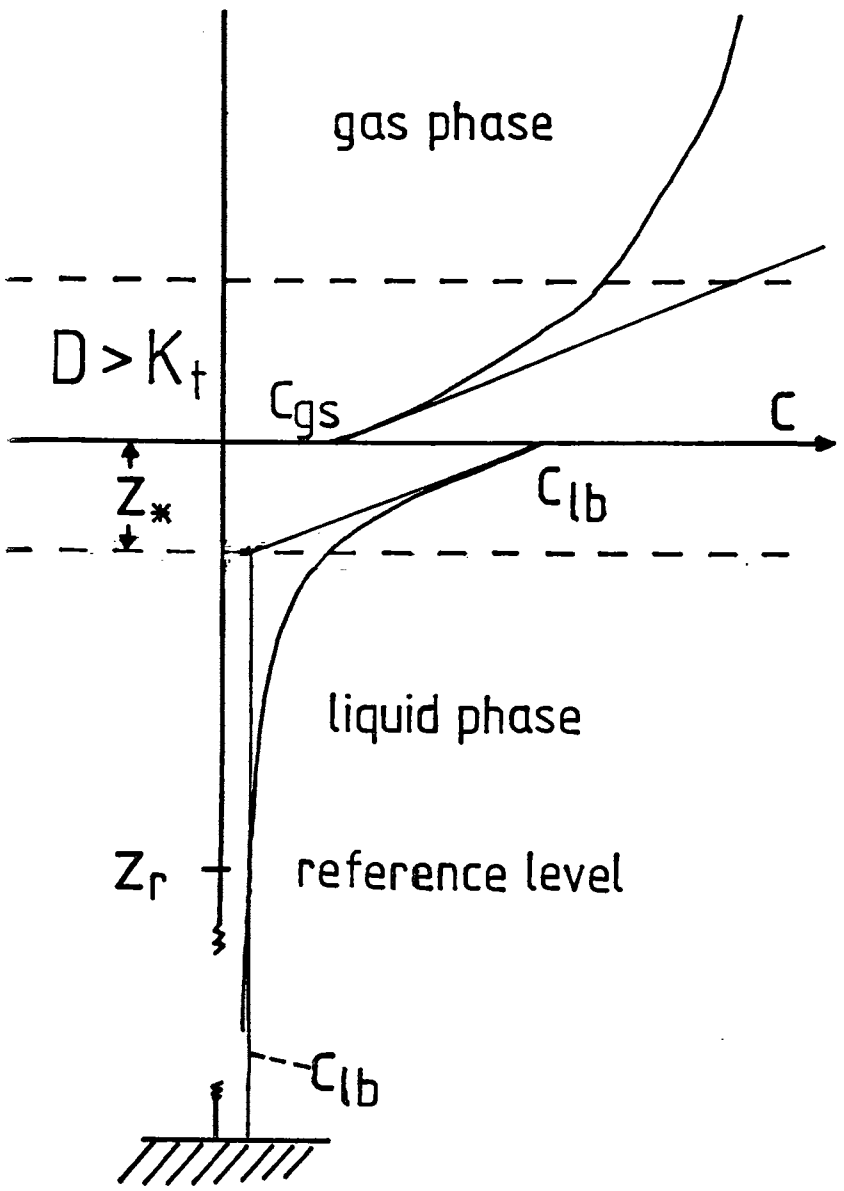

$$\frac{\partial C}{\partial t} = \frac{\partial}{\partial z}\left(D\frac{\partial C}{\partial z} - \langle c'w'\rangle\right), \tag{2.4}$$

$$\frac{\partial U}{\partial t} = \frac{\partial}{\partial z}\left(\nu\frac{\partial U}{\partial z} - \langle u'w'\rangle\right), \tag{2.5}$$

where the brackets < > denote mean values.

It turns out that the turbulent flux term in the momentum equation is exclusively caused by the nonlinear term in (2.2). Consequently, the nonlinearity of (2.2) is essential for the turbulent transport.

2.2 The scaling parameters for the transfer across the surface

As already mentioned in the previous paragraph, the transport equation for a passive tracer is linear in the concentration. So it is very useful to scale the flux across the surface with the concentration. The flux density divided by the concentration difference between the surface and the bulk (resp. some reference level) is defined as the transfer velocity k

$$k = j / (C_s - C_b) \tag{2.6}$$

The indices s and b denote the surface and bulk. The transfer velocity represents the velocity with which a tracer is pushed (by an imaginary piston) across the surface.

The thickness of the mass boundary layer, i.e. the region where molecular diffusion is the dominating process, can now be defined with the aid of the fact that at the surface the turbulent transport is zero. Then the flux density at the surface is given by

$$j_v = D\,\partial C / \partial z\,|_0, \quad j_c = \nu\,\partial U / \partial z\,|_0, \tag{2.7}$$

where the indices v and c refer to momentum and mass transfer respectively. The boundary layer thickness z^* is defined as the thickness of a fictive layer in which only molecular transport takes place with the gradient (2.7):

$$z^* = D / k. \tag{2.8}$$

Geometrically, z_* is given as the intercept of the tangent to the concentration profile at the surface and the bulk concentration, as illustrated in Fig. 2.1. The gradual decrease of the concentration gradient from the value at the surface given by (2.7) is caused by the increasing influence of turbulent transport.

Finally, the time constant t_* for the transport across the boundary layer is given by

$$t_* = z/k = D/k^2 \tag{2.9}$$

Now we have defined all scaling parameters for the transport across the boundary layer. Two basic conclusions are emphasized: First, the definition of the parameters does not depend on model considerations about the structure of the turbulence. We only make use of the linearity of the transport equation and the fact that the turbulent transport decreases to zero at the surface. Second, the parameters are not independent. They are coupled by the molecular diffusion coefficient. Therefore only one of these parameters needs to be measured in order to determine all scaling parameters of the transport across the boundary layer.

2.3 The ratio of gas-phase and liquid-phase transfer velocity

As shown in Fig. 2.1, we have a boundary layer on each side of the interface. At the surface itself the solubility equilibrium between the tracer concentration in the gas phase, c_g, and in the liquid phase, c_l, is established

$$c_{ls} = \alpha c_{gs}, \tag{2.10}$$

where α is the dimensionless (Ostwald's) solubility. The solubility causes a concentration jump at the surface. We must therefore adjust the concentrations when calculating the resulting transfer velocity across both layers by summing up the concentration differences. The resulting transfer velocity can be viewed from the gas phase or the liquid phase. In the gas phase it is given by

$$k_{gr}^{-1} = \Delta c_g/j = (C_{gb}-C_{gs})/j + 1/\alpha(C_{ls}-C_{lb})/j = k_g^{-1}+(\alpha k_l)^{-1} \tag{2.11}$$

Table 2.1: Ostwald's solubility for important tracers in pure water. The solubilities in salt water are 10 to 30% lower depending on the tracer and the water temperature. For chemical reactive tracers as SO_2, H_2S, and pentachlorophenol the physical solubilities are listed (Table from Jähne, 1982).

tracer	solubility				
temperature [°C]	0	10	20	30	40
He	0.0092	0.0090	0.0089	0.0090	0.0094
CO	0.034	0.028	0.025	0.021	0.019
O_2	0.047	0.038	0.032	0.029	0.026
NO	0.071	0.057	0.049	0.043	0.039
Kr		0.076	0.061	0.052	0.046
Xe		0.16	0.11	0.092	0.077
Rn	0.49	0.33	0.24	0.18	0.16
N_2O	1.26	0.88	0.65	0.50	0.40
CO_2	1.66	1.20	0.91	0.65	0.52
H_2S	4.5	3.4	2.5	2.2	1.8
SO_2	80	54	38	30	21
ethylene	0.22	0.16	0.13	0.10	0.09
trichloroethylene			1.9		
benzene			4.4		
hexachlorobenzene			5.4		
trichlorobenzene			6.8		
ethyl acetate			200		
pentachlorophenol			$1.2\ 10^3$		
DDT			$1.5\ 10^3$		
methanol			$7.0\ 10^3$		
aniline			$8.5\ 10^3$		
chloroaniline			$1.6\ 10^4$		
phenol			$2.3\ 10^4$		
atrazine			$2.0\ 10^4$		
DEHP			$2.5\ 10^4$		
momentum	787	813	847	877	900
heat			3,900		
water vapour	207,000	106,000	57,000	31,000	18,000

and correspondingly in the liquid

$$k_{lr}^{-1} = \alpha k_g^{-1} + k_l^{-1}. \qquad (2.12)$$

Mathematically, we just shift the multiplication with α from the concentration to the transfer velocity. Indeed, if we make the concentration in the water steady to the air concentration by dividing through α, as done in (2.11), the same flux is obtained, when we multiply the transfer velocity by α.

Consequently, the resulting transfer velocities in air and water differ by the factor α. The ratio $\mathfrak{H} = \alpha k_l / k_g$ determines which boundary layer controls the transfer process. Thus the solubility is a key parameter. High solubilities shift the control of the transfer process to the gas-phase boundary layer, and low solubilities to the aqueous layer. The solubility value for a transition from air-sided to water-sided control depends on the ratio of the transfer velocities. Tab. 2.1 shows the solubilities for important tracers including momentum and heat for which the "solubility" is defined analogously to (2.10) as

$$\alpha_\nu = \varrho_w / \varrho_a, \alpha_h = \varrho_w c_{pw} / \varrho_a c_{pa}. \qquad (2.13)$$

2.4 Friction velocity and energy dissipation velocity

The characterization of the momentum transfer is more complicated because of the quadratic term in the transport equation. According to (2.5) the flux density is proportional to the square of a scaling velocity, consequently defined as

$$\varrho u_*^2 = j_\nu = \nu \frac{\partial u}{\partial z} - \langle u'w' \rangle \qquad (2.14)$$

This is the definition for the friction velocity, characterizing the vertical momentum flux.

There is also the possibility to characterize the turbulent transport by energy considerations. The turbulent energy transferred to or across the interface will finally dissipate by molecular viscous forces ($\nu \Delta \underline{u}$ term in 2.2). So a certain energy flux density j_e is

necessary to maintain the turbulent transport. If this flux will be dissipated in a characteristic length scale l_e, the average energy dissipation in this length scale is

$$e = j_e/l_e \tag{2.15}$$

and the energy dissipation velocity u_e can be defined as

$$u_e^3 = l_e e = j_e. \tag{2.16}$$

This definition is especially useful if no momemtum is transferred across the interface (no stress at the surface), so that the transfer process cannot be described by a friction velocity. But even at a stress free boundary layer energy will be dissipated, so that the concept of the energy dissipation velocity is more general (Plate and Friedrich, 1984).

In a more practical, engineering point of view, also the energy flux density (equal to the power per unit surface) itself may be used as a parameter for the transfer velocity, since this comparison results in direct conclusions about the efficiency of the transfer process.

2.5 Sources of turbulence at a free gas-liquid interface

The basic parameters for all transfer processes now being established, the sources for the turbulence at the surface will be discussed next. The summary in Tab. 2.2 again illustrates the complexity of the turbulence phenomena at a free surface.

Instable stratification

Even if there is no mean flow both in the liquid and in the gas, free turbulent convection in both phases can be generated by buoyancy forces. Instable density stratification may be caused by vertical temperature and/or concentration gradients and thus are closely related to the corresponding flux (heat or tracer concentration). Considering environmental systems, instable stratifications are generated both in air and water by upward latent and sensible heat fluxes. In the ocean stratification is also influenced by salinity.

Table 2.2: Summary of the sources of turbulence at a free gas-liquid interface

source	caused by	examples
instable stratification	density gradients	atmosphere: gradients of temperature and water vapour water: surface cooling by upward heat fluxes
surface instability	change of surface tension with tracer concentration	absorption of reactive gases in water
shear instability	bottom shear	rivers, stirred vessels, open channel flows, falling films
	surface shear	oceans, lakes, rivers, falling films with countercurrent gas flow, bubbles, droplets, packed and bubble columns
wave instability	dissipation of steep waves into turbulence	oceans, lakes, rivers, oscillating bubbles, falling films
surface breaking	gravitational instability	breaking waves, bursting bubbles, boiling liquids

Surface instability

There exists a two dimensional analogue to the tree dimensional instabilities described above, the Marangoni instability. There a gradient of the surface tension is the driving force for the instabilities. This occurs, if a tracer which decreases the surface tension of the liquid is being transported across the surface. Then small concentration fluctuations can be amplified, since a region of higher tracer concentration and therefore lower surface tension spreads over the surface sweeping additional water with higher concentration to the surface. This kind of instability is less important in environmental systems, but significant in many gas-liquid reactions.

Shear instability

Surface and stratification instability become less important with increasing mean velocity. Then turbulence is primarily created by shear instability. Due to the Reynolds criterion transition from laminar to turbulent flow occurs if the velocity gradient exceeds a certain length scale (i.e. ul/ν or $\partial u/\partial l * l^2/\nu > Re_c$).

Bottom shear

First we shall consider the case where momentum flux across the surface (surface stress τ_s) is much lower than the flux from the bulk liquid flow to the bottom (and to the walls), τ_l. In this case, turbulence is created by bottom shear and turbulent eddies penetrate towards the free surface from below. There is a large number of technical systems of this kind due to the many possibilities to generate a liquid flow: stirred vessels, open channel flow, falling films (comp. Tab. 2.2). Rivers are the only natural system to which this case applies, since in lakes and the ocean the water velocities generally are too low.

Surface shear

When the surface stress becomes dominant over the bottom stress, additional small scale turbulence is generated directly in the surface layer. If the surface stress is the only momentum input into the liquid then the whole liquid system is determined by the air flow above and stress continuity is preserved troughout the whole system. It is a basic characteristic of this condition that due to the high "solubility" of momentum the momentum transport into the liquid is controlled by the transport mechanisms in the air (see next chapter).

Therefore the water velocity is much smaller than the wind speed in the atmosphere (typically a few %) and the momentum flux only depends on the wind speed, the stability in the air, and the roughness of the surface, but does not depend on any other parameter in the liquid. This is different for any kind of bottom turbulence, since the shear stress being transferred from the bulk to the wall or any kind of stirrers in this case depends on the viscosity of the liquid.

In addition, it is important to note that the waves on the free water to a first approximation can be considered to be static roughness elements for the air flow, as long as their phase speed is small compared to the wind speed. The dimensionless ratio of the phase speed of the dominant wave and the windspeed U, the wave age

$$a = c / U \tag{2.16}$$

is an important parameter to characterize the conditions for the air flow besides the small scale roughness of the water surface by small scale gravity and capillary waves.

Generation of turbulence by waves

Considering the liquid flow the waves cannot be regarded as static roughness elements at all. Their characteristic velocity is of the same order of magnitude as the velocity in the shear layer at the surface. This fact causes a basic asymmetry between the turbulent processes on the air and on the water side of the interface. It can be concluded that the wave effect on the turbulent transfer in the water may be much stronger and of quite different quality than in the air.

At first glance, it is surprising that waves shall contribute to turbulent transport. A single sinusoidal wave cannot contribute to the turbulent flux, since the closed orbitals move a water packet periodically up and down, but not towards or away from the surface. The correlation terms $\langle u'w' \rangle$ and $\langle c'w' \rangle$, which are the turbulent transport terms in (2.4) and (2.5) are zero for periodic motion.

But the real waves on liquid surfaces are far away from being a linear superposition of sinusoidal waves. The nonlinearity of the Navier-Stokes' equation (2.2) already reveals that a sinusoidal wave can only be an approximative solution for waves with low steepness and that a

superposition of two waves or of waves and a turbulent shear flow is no longer a solution of the equation and must cause interactions.

Waves store a considerable fraction of the energy flux across the surface. Considering that the energy flux from the air to the waves is of the same order of magnitude as to the shear flow, this can simply be concluded from the slow response of the waves to the wind. It takes minutes or hours for the dominant waves to develop to large wavelengths, whereas the shear flow in the viscous layer is generated within seconds. Thus even a weak interaction can give a considerable contribution to the near-surface turbulence.

The complex interactions need further considerations. Fig. 2.2 schematically outlines the turbulent fluxes across a free gas-liquid interface. If no waves are generated the shear stress at the surface produces small scale turbulence at the surface. In addition large scale eddies from the bulk can penetrate into the surface layer, sweep it directly back into the bulk or generate small scale turbulence. In any case, the turbulent energy is finally dissipated by viscous forces from the small scales.

When waves are generated a second energy cycling is established. Energy from the turbulent air flow is transferred to different wave lengths and by means of nonlinear interaction between waves of different scales. In addition, there are several possibilities of interaction with the turbulent shear flow.
First, waves propagating in a turbulent flow are scattered and damped by horizontal velocity fluctuations. Analogous phenomena occur by the propagation of electromagnetic and sound waves through turbulence (Monin and Yaglom, 1975). The basic difference is that water surface waves are two-dimensional and that the ratio of the velocity fluctuations to the phase speed is much higher than for acoustic or electromagnetic waves. So stronger effects can be expected for water waves.
Second, steep gravity waves become rotational and add a Stokes' drift to the turbulent shear flow.
Finally, and most important for the near-surface turbulence, with increasing steepness both gravity and capillary waves become more and more instable and decay to turbulence. The length scale into which

Figure 2.2: Schematic representation of the turbulent fluxes across a free air-water interface in the presence of surface waves

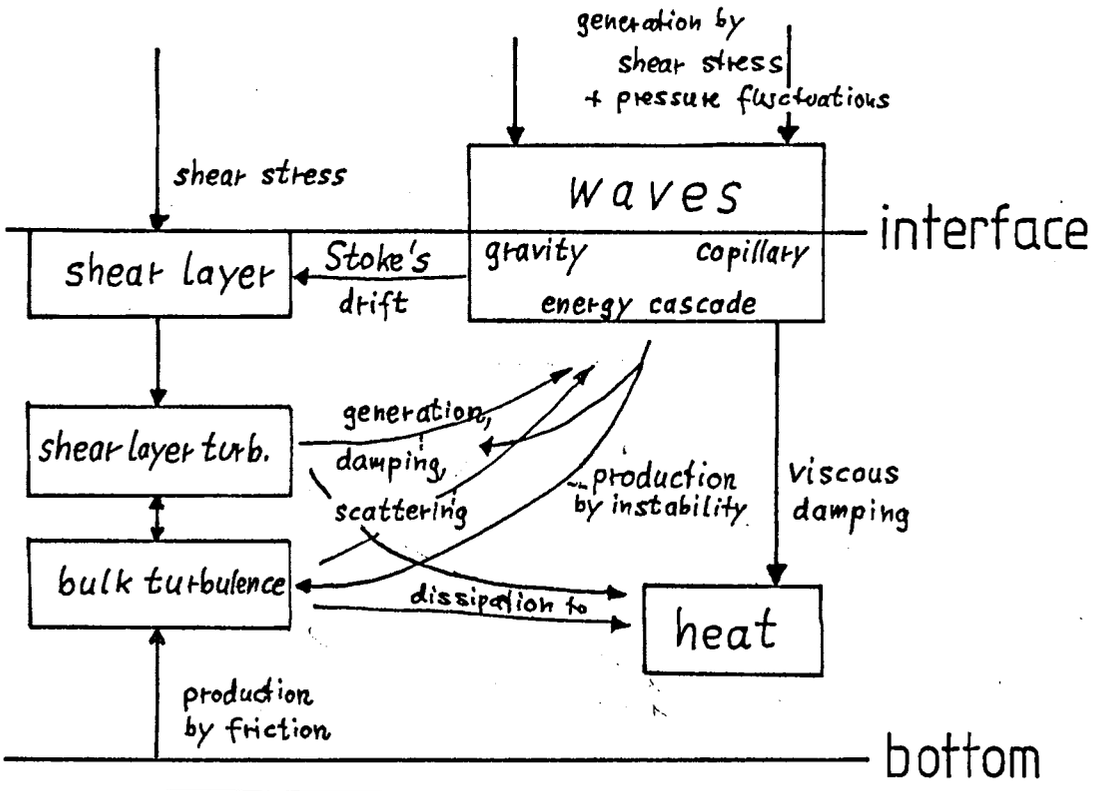

this turbulence is produced is critical for the transfer processes at the surface and as turbulent motion wave energy is finally dissipated by molecular viscosity. A dynamic equilibrium between all these energy fluxes is established in steady state wind conditions. Besides the surface stress and the physicochemical properties of the surface both the duration and the fetch of the wind are critical parameters for the equilibrium.

Surface breaking

The surface stress cannot be increased to infinity. At higher wind speeds the waves become so instable that they break. This happens when the acceleration of the wave motion exceeds the gravitational acceleration g, as pointed out by Phillips (1958). On the small scale end, the surface tension determines the breaking down of a continuous surface. There seems to be a critical point beyond which the turbulent transfer is dominantly enhanced by the surface increase.

2.6 Analogies between mass, heat, and momentum transport

After having briefly listed the possible sources of turbulence at both sides of the gas-liquid interface, we shall now discuss the analogies between mass, heat, and momentum transport across the interface. At the very surface the transport is dominated by the molecular diffusivities. So the (dimensionless) ratio of the kinematic viscosity (molecular diffusion coefficient for momentum) and the diffusion coefficient for the passive tracer, the Schmidt number Sc

$$Sc = \nu / D \qquad (2.17)$$

is an important parameter. (For heat the corresponding ratio is usually called the Prandtl number.) Again, there is a basic asymmetry between the gas and liquid phase. The Schmidt numbers in air are close to 1 for all tracers and nearly temperature independent. Two important conclusions result from this fact: First, the transfer resistance for all tracers (including momentum and heat) are roughly equal. Second, the resistances in the viscous and turbulent layer up to a reference level of 10 m are of same order (Jähne, 1982).

Table 2.3: Schmidt numbers of different tracers in water

TRACER	SCHMIDT NUMBER IN WATER							
temperatur [°C]	0	5	10	15	20	25	30	35
heat	13.5		9.5		7.0		5.4	
He		294	230	184	149	122	102	84
Ne		582	443	347	274	220	179	145
Kr		1490	1090	820	624	481	380	297
Xe		1944	1407	1046	791	605	471	365
Rn	3150		1600		870		500	
H_2		480	362	281	221	175	142	114
CH_4		1380	1030	781	605	473	376	299
CO_2		1420	1050	786	605	468	371	292

Due to the slow molecular diffusion of mass and heat in the water, the Schmidt numbers in water are high (Tab. 2.3). In addition, they strongly depend on the water temperature because of the opposite sign in the temperature dependence of the kinematic viscosity and the diffusion coefficient for mass. From 0 to 40 °C the Schmidt number typically decreases by one order of magnitude. In contrast to the transfer in air, the transfer velocity in water depends on the temperature due to this effect. Moreover, the high Schmidt number increases the transfer resistance across the surface layer, so that the transfer resistance through the turbulent layer in this case can be neglected: the bulk of the liquid is well mixed concerning mass transfer, unless mixing is suppressed by stratification.

The Schmidt number controls the ratio of the corresponding boundary layer thicknesses at the surface. For high Schmidt number, i.e. low molecular diffusivity, the layer in which the molecular transport is dominant is thinner

$$z*_v/z*_c = Sc^{1-n}. \tag{2.18}$$

This is an universal scaling law resulting from the fact that the transfer just at the interface takes place by molecular transport only. It can be seen immediately that the argument n characterizes the increase of the turbulence with the distance from the surface. n=1, for instance, means a stagnant diffusive layer at the surface with a sudden onset of the turbulence at the edge of this layer ("film model": Whitman, 1923; Liss and Slater, 1974).

For the special case of surface stress dominated transfer across the surface a dimensionless transfer resistance r can be defined as

$$r = u*/k, \tag{2.19}$$

which directly compares momentum and mass transfer. So with the aid of (2.18) and (2.8) r can be expressed in the following formula

$$r = \beta\, Sc^n + r'(z_r). \tag{2.20}$$

r' is the additional transfer resistance from the edge of the viscous layer to the reference level z_r, and can be neglected for high Schmidt

numbers. ß is the transfer resistance for momentum across the viscous boundary layer (Sc_V=1). ß is a function of many parameters reflecting the dynamic equilibrium of the near-surface turbulence with the momentum flux across the interface as discussed above. In addition, the exponent n depends on the boundary conditions at the surface, which are discussed in the next chapter.

The analogy between momentum and mass transfer is clearly expressed in (2.20). It is useful, since ß can be derived from velocity profiles at the surface (chapter 2.8). If, in addition, the Schmidt number exponent is known from the boundary conditions at the surface, (2.2) gives the transfer resistance for mass.

In the case of a stress free surface, the energy dissipation velocity must be used as a scaling parameter instead of the friction velocity.

2.7 The boundary condition at a free gas-liquid interface: the influence of surface films

The above considerations showed the basic fact that the mass and heat boundary layers are thinner than the viscous boundary layer. So the concentration gradient for mass and heat is mainly restricted to a region in which the momentum transfer is still dominated by the molecular viscosity. This justifies a Taylor expansion of the mean velocity profile at z=0 in order to obtain the z-dependence of the turbulent term in the mass boundary layer. The Taylor expansion for the concentration profile of mass and heat may be questionable, because for the same distance z from the surface the turbulent term already becomes dominant over the molecular diffusion.

In order to calculate the Taylor expansion the boundary conditions at a free gas-liquid interface must be discussed carefully. On a free water surface velocity fluctuations are possible, only the normal component w' must be zero

$$u' \neq 0,\ v' \neq 0,\ w' = 0. \qquad (2.21)$$

(In contrast, at a rigid surface all velocity fluctuations must be zero.) From the continuity equation for the velocity fluctuations we then get

$$\partial w'/\partial z\,|_0 = -\,(\,\partial u'/\partial x + \partial v'/\partial y\,)\,|_0 \neq 0 \qquad (2.22)$$

It is important to realize the physical meaning of this equation. $\partial w'/\partial z\,|_0 \neq 0$ means that there is a convergence or divergence zone at the surface, which is equivalent to the fact that two dimensional continuity $\partial u'/\partial x\,|_0 + \partial v'/\partial y\,|_0 = 0$ is valid at the surface. If continuity is not preserved at the surface, surface elements are dilated or contracted.

At a clean water surface dilation or contraction of a surface element does not cause restoring forces, since surface tension only tries to minimize the total free surface area, which is not changed by this process.

However, as soon as there are films on the water surface the film pressure works against the contraction. This is the very point at which the physicochemical structure of the surface essentially influences the structure of the near-surface turbulence and the generation of waves. Similarly to a rigid wall, a strong film pressure at the surface maintains two-dimensional continuity at the interface and consequently the first z-derivative of w' must be zero. More generally, an equilibrium between the kinetic energy of the turbulent eddies moving towards or away from the surface and the surface dilation is established in the mean. So for a given film pressure $\partial w'/\partial z\,|_0$ will gradually increase from zero to the value for a clean surface with increasing turbulent energy in the liquid.

The z-derivatives of the mean concentration and velocity can be calculated by differentiating (2.4) and (2.5) for z=0

$$\partial U/\partial z\,|_0 = -j\ /\!\!\gg,\ \partial^n U/\partial z^n\,|_0 = \partial^{n-1}/\partial z^{n-1}(\langle u'w'\rangle\,|_0)\quad n>=2 \qquad (2.23)$$

and

$$\partial C/\partial z\,|_0 = -j_C/D,\ \partial^n C/\partial z^n\,|_0 = \partial^{n-1}/\partial z^{n-1}(\langle c'w'\rangle\,|_0)\quad n>=2. \qquad (2.24)$$

Coantic (1985) made a careful analysis of the single derivatives and finally obtained the following Taylor expansions

$$U(z) = U_s - (u_*^2/\vartheta)\cdot z - \left\langle u' \frac{\partial v'}{\partial y} \right\rangle \Big|_0 z^2 + \frac{1}{2}\left\langle 2\frac{\partial u'}{\partial z}\frac{\partial w'}{\partial z} + u'\frac{\partial^2 w'}{\partial z^2} \right\rangle \Big|_0 z^3 + \frac{1}{6}\left\langle u'\cdot\frac{\partial^3 u'}{\partial z^3} + 3\frac{\partial w'}{\partial z}\frac{\partial^2 u'}{\partial z^2} + 3\frac{\partial u'}{\partial z}\frac{\partial^2 w'}{\partial z^2} \right\rangle \Big|_0 z^4 \qquad (2.25)$$

and

$$C(z) = C_s - (j_c/D)\cdot z + \left\langle \frac{\partial c'}{\partial z}\frac{\partial w'}{\partial z} \right\rangle \Big|_0 z^3 + \frac{1}{2}\left\langle \frac{\partial c'}{\partial z}\frac{\partial^2 u'}{\partial z^2} + \frac{\partial^2 c'}{\partial z^2}\frac{\partial u'}{\partial z} \right\rangle \Big|_0 z^4 \qquad (2.26)$$

The striking difference between the expansions of the velocity and concentration profiles arises from the three-dimensional nature of the velocity field. In fact, the z^2-term is zero, if a two-dimensional velocity field is assumed. Only in this case both profiles rise with the same power in z.

Now the influence of surface films is to be considered. If $\partial w'/\partial z \,|_0$ is gradually decreased to zero, the z^3-terms in both profiles will also decrease to zero and the influence of the turbulence in the boundary layer will finally change to a z^4-term. Coantic (1985) further proves that the z^4-term in the velocity expansion vanishes, if the turbulent field is two-dimensional.

Despite all these difficulties with the structure of the velocity field, we can safely conclude that surface films on a free surface increase the power in z of the turbulent transport term. Furthermore, the power expansions are the same for a free surface covered with a strong surface film and for a rigid wall, since in both cases $\partial w'/\partial z \,|_0 = 0$. Therefore a two-dimensional continuity at the surface is equivalent to the more restrictive conditions u'=0, v'=0 at a rigid wall as far as the turbulent structure below is concerned.

2.8 Simple models for the turbulence structure in the viscous layer

From the previous discussion we take the idea that the turbulent transport term increases with a certain power in z

$$\langle u'w' \rangle \sim z^i \text{ and } \langle c'w' \rangle \sim z^i. \qquad (2.27)$$

Even with such a formulation it is not possible to solve the transport equations (2.4,5) readily. So the classical assumptions are used to solve them. The turbulent transport term

$$\partial/\partial z\langle u'w'\rangle \text{ resp. } \partial/\partial z\langle c'w'\rangle$$

is approximated by two different terms, linear in U and C respectively, assuming different structures of the turbulence.

Large eddy, single-stage transport (SR-models)
On the one hand, large eddies may play the dominant role and statistically replace the whole or parts of the surface layer by volume elements from the bulk. Generally, the surface renewal rate λ is a function of the distance. A power law is assumed

$$\lambda = \lambda_p' z^p \quad \text{with } p\geq 0. \tag{2.28}$$

p=0 is the classical surface renewal model (Higbie, 1935; Danckwerts, 1951; Münnich and Flothmann, 1975) with no dependence of the renewal rate on the distance from the surface and $\lambda_0 = t_*^{-1}$. For p>0 the surface renewal rate approaches zero at the surface and thus takes care of the fact that convergences are not allowed at a dirty surface. With the surface renewal hypothesis the turbulent transport terms are given by

$$\partial/\partial z\langle u'w'\rangle = -\lambda_p' z^p\,(U-U_b) \quad \text{and} \quad \partial/\partial z\langle c'w'\rangle = -\lambda_p' z^p\, C, \tag{2.29}$$

where surface elements are replaced by elements with the bulk velocity U_b. The bulk concentration C_b is assumed to be zero.

Small eddy, multi-stage transport (D-models)
An alternative approach to the turbulent structure in the boundary layer is a small eddy, multi-stage model, where the turbulent transport is approximated by a local turbulent diffusion coefficient K being defined as

$$K_v\,\partial U/\partial z = \langle u'w'\rangle \quad \text{and} \quad K_c\,\partial C/\partial z = \langle c'w'\rangle \quad \text{resp.} \tag{2.30}$$

The indices v and c denote momentum and mass respectively. K_v and K_c are also assumed to follow a power law in z (King, 1966)

$$K_{v,c} = \nu\alpha_{v,c}\, z^m \quad \text{with } m>=2. \tag{2.31}$$

Consequently, the turbulent transport terms are

$$\partial/\partial z\langle u'w'\rangle = \partial/\partial z(\nu\alpha_v\, z^m\, \partial U/\partial z) \quad \text{and}$$

$$\partial/\partial z\langle c'w'\rangle = \partial/\partial z(\nu\alpha_c\, z^m\, \partial C/\partial z) \quad \text{resp.} \tag{2.32}$$

A comparison of (2.32), (2.29), and (2.27) shows that for p = m-1 = i-1 the same power dependence is given.

The transport equations can now be made dimensionless using the scaling parameters for the boundary layer transport as defined in chapter 2.2. We will make both transport equations dimensionless with the scaling parameters for momentum transport. The following dimensionless parameters are then obtained with

$$z_+ = zu_*/\nu, \quad t_+ = t/t_{*m} = tu_*^2/\nu, \quad C_+ = C/\Delta C \quad \text{and} \quad U_+ = U/u_* \tag{2.33}$$

surface renewal models	diffusion models
$\frac{\partial U_+}{\partial t_+} = \frac{\partial^2 U_+}{\partial z_+^2} - \lambda_p z_+^p (U_+ - U_{+b})$	$\frac{\partial U_+}{\partial t_+} = \frac{\partial}{\partial z_+}\left(1+\alpha_v z_+^m\right)\frac{\partial U_+}{\partial z_+}$
with $\lambda_p = \lambda'_p\,(\nu/u_*)^p$	resp. $\alpha_v = \alpha_v'\left(\frac{\nu}{u_*}\right)^m$
$\frac{\partial C_+}{\partial t_+} = Sc^{-1}\frac{\partial^2 C_+}{\partial z_+^2} - \lambda_p z_+^p C_+$	$\frac{\partial C_+}{\partial t_+} = Sc^{-1}\frac{\partial}{\partial z_+}\left(1+Sc\alpha_c z_+^m\right)\frac{\partial C_+}{\partial z_+}$
with $\lambda_p = \lambda'_p\,(\nu/u_*)^p$	resp. $\alpha_c = \alpha_c'\cdot\left(\frac{\nu}{u_*}\right)^m \cdot Sc_t^{-1}$

(2.34) (2.35)

where $Sc_t = K_v/K_c$ is the turbulent Schmidt number. It is the aim of the following calculations to prove that for both models the analogy between mass and momentum transfer can be expressed as in (2.20). The calculations will be done in the limit of high Schmidt numbers and result in a direct relation between the velocity profile at the very surface and the transfer resistance for mass including the Schmidt number exponent.

Diffusion models

The steady state concentration profiles for the diffusion models can be calculated by direct integration of (2.35)

$$C_+ = 1 - A \int_0^{z_+} (Sc^{-1}+\alpha_c Sc_t^{-1} z_+'^m)^{-1} dz_+'. \qquad (2.36)$$

For high Schmidt numbers the concentration C_+ is zero before the edge of the viscous boundary ($z_+<10$) so that it is allowed to extend the integration to infinity in order to calculate the constant A from the boundary condition $C_+(z_+\to\infty)=0$

$$A = m\sin(\pi/m)/\pi \; (Sc_t/\alpha_v)^{1/m} \; Sc^{-1+1/m}. \qquad (2.37)$$

Differentiating at $z_+=0$ and using (2.6), (2.7), and (2.19) finally yields the dimensionless transfer resistance

$$r = (Sc_t/\alpha_v)^{1/m} \; \pi/[m\sin(\pi/m)] \; Sc^{1-1/m}. \qquad (2.38)$$

The corresponding velocity profile at the surface is given by

$$U_+ = U_{s+} - z_+ + [\alpha_v/(m+1)] z_+^{m+1}, \qquad (2.39)$$

where α_v is the only free model parameter denoting the value of the turbulent diffusion coefficient at the surface. The turbulent Schmidt number is assumed to be 1.

Surface newal models (SR)

A numerical solution of transport equation (2.35) was carried out by Jähne et al. (1985b). Here we shall use an alternative approach. From the definition of the transfer velocity (2.6) and (2.7) the transfer velocity for momentum across the viscous layer is given by

$$k_v = u_*^2 / \Delta U. \qquad (2.40)$$

Consequently, the dimensionless transfer resistance reduces to

$$r_v = \Delta U_+. \qquad (2.41)$$

ΔU_+ is the velocity at the edge of the viscous boundary layer and can be obtained by adjusting the calculated model profile smoothly to the

measured surface velocity profile (Münnich and Flothmann, 1975). These formulas are also valid for the diffusion model. From the similarity between (2.34) and (2.35) follows

$$r_C = \Delta U_+ \, Sc^{(p+1)/(p+2)}. \qquad (2.42)$$

The velocity profile is given by

$$U_+ = U_{S+} - z_+ + O(z_+^{p+2}). \qquad (2.43)$$

Conclusions

The equations directly point out the different results for both kinds of models. For the same z_+ exponent i+1 in the deviation of the velocity at the very surface from a linear profile they result in different Schmidt number exponents n

$$n(SR) = i/(i+1) \qquad n(D) = (i-1)/i. \qquad (2.44)$$

Or expressing the same fact the other way round: The same Schmidt number exponent n is obtained for

$$m = p+2 \quad \text{and} \quad i(SR) = 1/(1-n),\ i(D) = (2-n)/(1-n). \qquad (2.45)$$

This important conclusion allows to differentiate both models from simultaneous measurements of the Schmidt number exponent n and the velocity profile at the very surface. Both models only coincide for $l, m \to \infty$ to the film model.

The above results can be checked with specific models. Deacon (1977), for instance, used Reichardt's universal profile at a smooth wall to calculate the mass transfer velocity. With a turbulent diffusion coefficient

$$K_t = \varkappa y z_V (z_+/z_V - \tanh(z_+/z_V)) \text{ with } z_V = 11.7,\ \varkappa = 0.4 \qquad (2.46)$$

he obtained

$$r = 12.1\ Sc^{2/3} + 2.7 \log Sc + 2.90 \quad \text{for } Sc > 10. \qquad (2.47)$$

Reichardt's formulation of the turbulent diffusivity means a cubic increase of the turbulent diffusion coefficient at the very surface

$$K_t/\nu = \varkappa\ell/(3z_v^2)z_+^3 \quad \text{for } z_+ << z_v. \tag{2.48}$$

This relation yields with (2.38)

$$r = 12.2\ Sc^{2/3} \qquad \text{for } Sc >> 1, \tag{2.49}$$

a result very close to (2.47).

One should, however, keep in mind that these models are not the only possible interpretation of the relation of the velocity profile at the surface and the mass transfer velocity. Both models are no exact solutions for the turbulent structure at the surface, they rather are linear approximations none of which may picture the physical reality.

The discussion about the boundary conditions at a free surface showed that only the turbulent transport term for momentum and not the one for mass depends on the dimensionality of the turbulence. This fact is a starting point for a general criticism of the analogy between turbulent mass and momentum transport in the viscous boundary layer as expressed by a constant turbulent Schmidt number. Different z-power dependences for the turbulent transport of both quantities suggest a significant z-dependence of the turbulent Schmidt number.

Nevertheless, the above models provide a useful formulation for the turbulence in the boundary layer. The discussion in the following chapters will show that many features of the transport across the surface do not depend strongly on the structure of the turbulence and can be well described by the above models.

3. THE MEAN TRANSFER VELOCITY

This chapter is about the mean parameters characterizing the transfer across the free surface. It will mainly deal with the mean transfer velocity and the parameters controlling it: wind stress at the surface, waves, and turbulence in the water. Indeed, most investigations do not exceed the measurement of mean parameters. So this chapter is also a brief report of the state of the art. We will mainly discuss the transport dominated by surface stress.

After a brief summary of the measuring methods with special regard to our circular wind-wave facilities, the available data from wind-wave tunnels are analysed and compared with the models from the previous chapter. A special paragraph deals with the dependence of the transfer velocity on the Schmidt number, since in our lab the first successful measurements of this kind in wind-wave tunnels have been carried out, allowing new conclusions about the transfer process.

3.1 Measuring methods for the mean gas transfer velocity

Mass balance methods

The most common method to determine the gas transfer velocity is based on mass balance considerations. By definition (2.6), the transfer velocity is given as the ratio of flux density and concentration difference and can be deduced from time traces of the tracer concentrations in air and water. The flux density is obtained from the tracer mass balance in the liquid

$$V_l \dot{c}_l = F_l j \quad \text{or} \quad j = h_l \dot{c}_l, \tag{3.1}$$

where V_l, F_l, and h_l are the volume, surface, and the effective height V_l/F_l of the water body. The transfer velocity is directly related to the concentration changes and yields the time constant τ with the aid of (2.6)

$$k = h_l \dot{c}_l/c_l = h_l/\tau. \tag{3.2}$$

Transfer velocities obtained in this way are, firstly, integrated over

the whole surface of the liquid phase and, secondly, are integrated over time scales in the order of τ. The first fact causes problems already in linear wind-wave facilities, where the wave field strongly depends on the fetch. If only one critical parameter controlling gas exchange significantly changes with fetch, any parameterization would be questionable. The circular facilities we used in our experiments (see below), avoid this disadvantage because of their steady-state and homogeneous wave field.

In field experiments there are two other problems in addition. Due to the large effective depth of the mixed layer (10 to 100 m deep in stratified lakes or the ocean), the time scales for changes of the water concentration scale up to several weeks. This makes the parameterization of the gas exchange rate with wind speed, waves, or other parameters very difficult, since their changes are by several orders of magnitude faster.

On the other side, it needs much effort to close the mass balance carefully. The most widely used method in the ocean is the ^{222}Rn deficit method, where the gas transfer velocity is contained in the deficit relative to the radioactive equilibrium with ^{226}Ra. From the detailed work of Roether and Kromer (Kromer and Roether, 1983; Roether and Kromer, 1984) it can be concluded that the complicated mass balance for radon including its instationarity and lateral divergences is responsible for a rather large uncertainty in the extensive GEOSECS data (Peng et al., 1979)

The situation is not as bad with the T-^{3}He-method widely used in lakes (Torgersen et al., 1977). Tritium, the source of the ^{3}He oversaturation in the lake, in the most cases is distributed homogeneously. During the summer stagnant phase high ^{3}He oversaturation in the hypolimnion is reached escaping during the winter convection. Here, the highly variable surface concentrations must be taken into account (caused by variations of the inner mixing due to changing meteorological conditions) in order to determine reliable transfer rates (Jähne et al., 1984b).

Direct flux determination in the air

In order to overcome the disadvantages of the large scale integrating mass balance methods several authors proposed to determine the air-sea

gas exchange rate by measuring the flux in the air. Jones et al. (1977) proposed an eddy correlation technique to measure the CO_2 air-sea flux. But up to now the measurements yield exchange rates being completely inconsistent with all previous knowledge: They suggest gas exchange rates one order of magnitude higher (Wesely et al., 1982). The discrepancy is not clearly understood, but may partly be caused by the fact that the CO_2 flux signal has to be corrected due to temperature and humidity fluctuations. These corrections are higher than the remaining signal (Smith and Jones, 1985) and may be more erroneous than expected.

In a recent paper Roether (1983) proposed to determine the air-sea gas flux of ^{222}Rn or methyliodide in air by a gradient method. This can be a promising way, if it is possible to measure the small concentration differences accurately enough. The experimental verification remains to be seen.

In conclusion, mass balance methods still are the state of the art.

3.2 The Heidelberg circular wind-wave facilities

Experimental set up

The Environmental Physics Institute, Heidelberg University, uses two circular wind-wave facilities of different diameter, as outlined in Fig. 3.1 and Fig. 3.2.

Tab. 3.1 summarizes the basic features of the tunnels. Both are gas-tight and in both the wind is produced by a rotating paddle-wheel. The small tunnel is a versatile instrument put into an isolated box for temperature control of the whole system from 3 to 40 °C.

These tunnels represent an approach alternative to the conventional linear facilities for the simulation of air-sea transfer processes. In contrast to the short fetch, non-steady wave field of linear tunnels they offer the advantage of an homogeneous steady-state wave field of unlimited fetch. Because of limited depth and circumference even with the circular systems oceanic wave scales cannot be reached. A detailed discussion of wave slope spectra from circular and linear facilities is found in chapter 5.3.

Table 3.1: Summary of the basic features of the Heidelberg circular wind-wave facilities

feature	small facility	large facility
range of wind speeds	0 to 10 m/s	0 to 12 m/s
outer diameter of the annular water channel	0.60 m	4.00 m
width of the water channel	0.10 m	0.30 m
maximum water depth	0.08 m	0.40 m
water surface	0.157 m^2	3.5 m^2
maximum water volume	12.6 l	1.4 m^3
maximum gas flushing rate	50 l/min	1.5 m^3/min

Figure 3.1: Outline of the small circular wind-wave facility. The gas-tight system can be flushed with dry nitrogen or any other gas.

Figure 3.2: Cross-section of the large circular wind-water tunnel

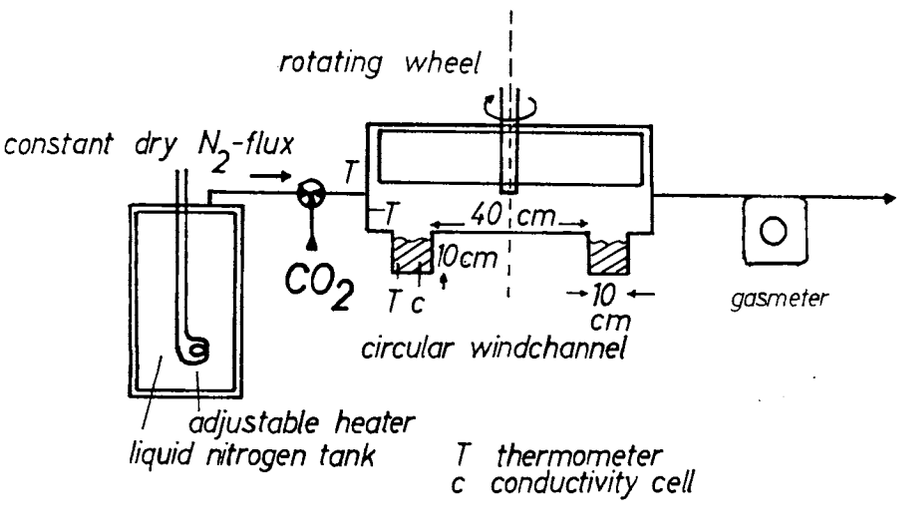

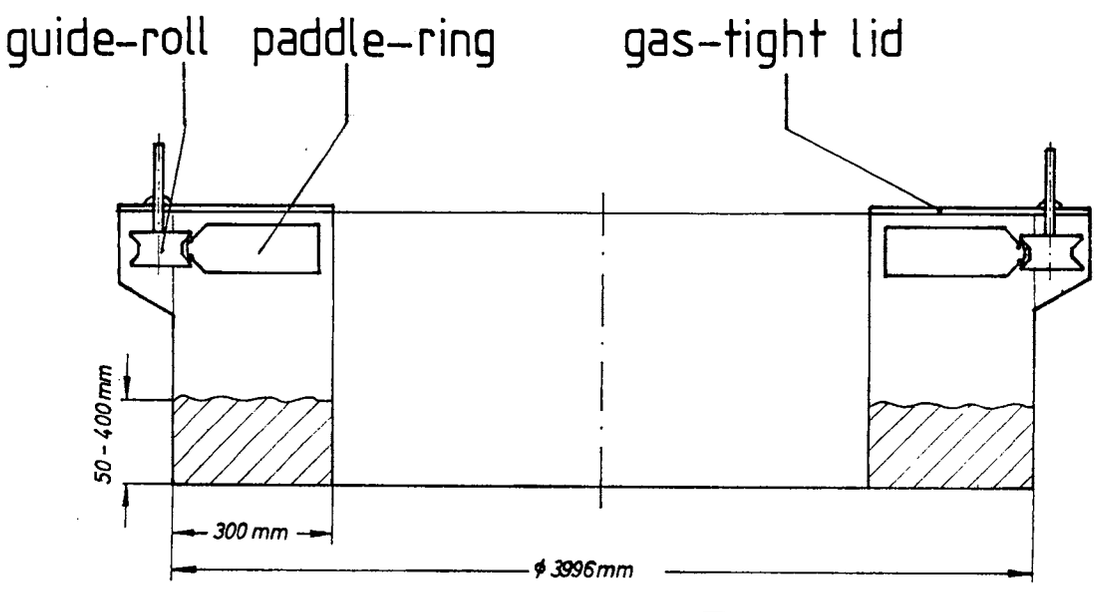

Figure 3.3: Humidity profiles in the small circular facility at 1.5 m/s wind, demonstrating the secondary currents (from Weißer, 1980).

Figure 3.4: Water velocity profiles at 1.2 m/s wind in the small circular facility. The radial positions are denoted as the distance from the inner wall (from Ilmberger, 1980).

Figure 3.5: Angular deviation of the water flow from the radial direction at several radial positions as indicated. Same wind speed as Fig. 3.4 (from Ilmberger, 1980).

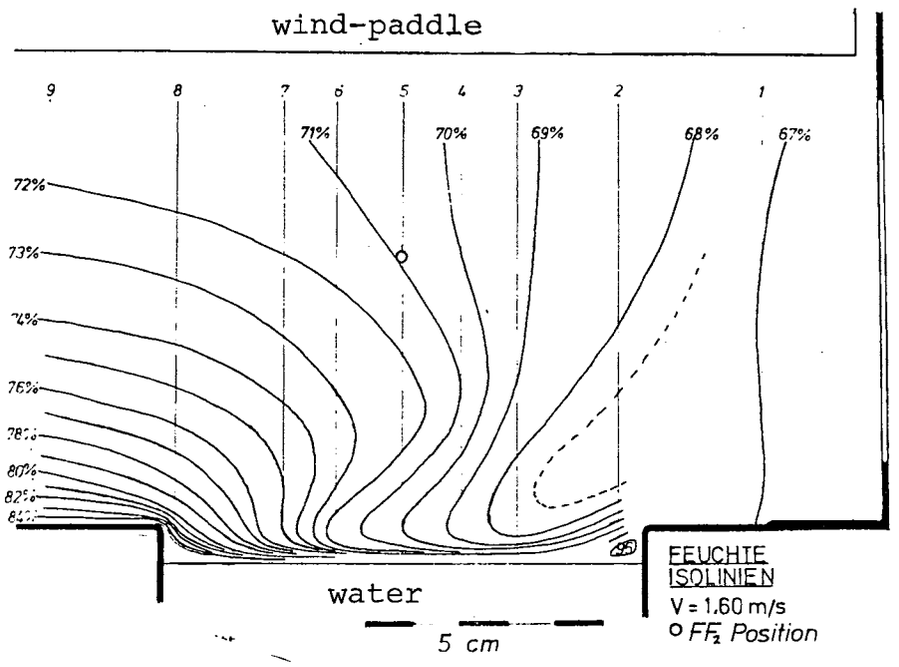

3.3

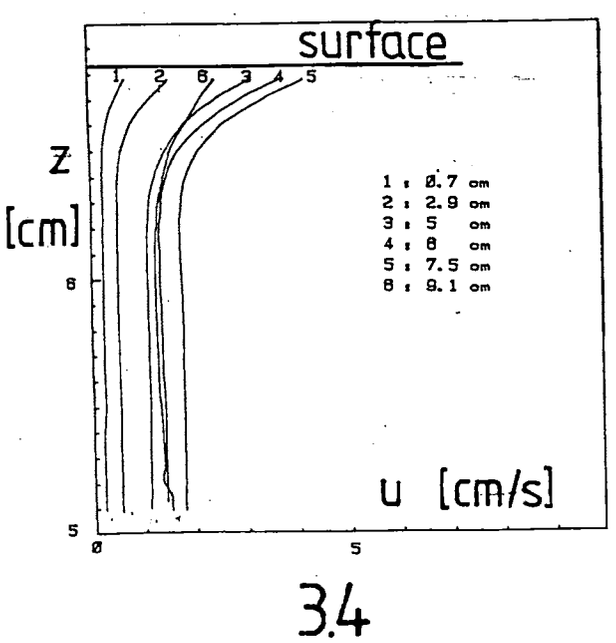

3.4

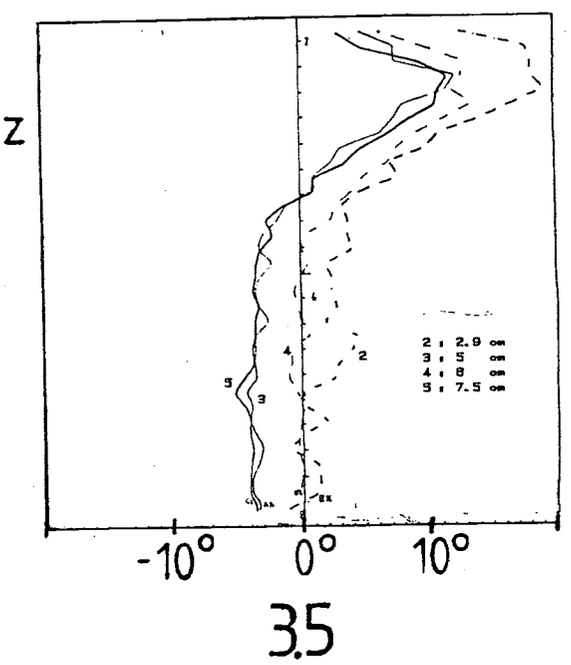

3.5

Influence of centrifugal forces on the transfer processes

One principle disadvantage of the circular tunnel geometry is the influence of centrifugal forces on the air and water flow. These effects have been studied in the small facility by Weißer (1980) for the air side and Ilmberger (1980) for the water side. Both turbulent layers are heavily influenced by secondary flow (Fig. 3.3), enhancing vertical mixing so that the logarithmic profiles on both sides of the interface are flattened to an almost constant velocity up the viscous boundary layer (Fig. 3.4). So the turbulent layers are not realistically simulated.

The viscous boundary layers, however, are much less affected, because of a compensation effect: In the air-sided boundary layer the velocity decreases towards the interface, so that the pressure gradient exceeds the decreasing centrifugal forces and turns the wind to the inner. Over a solid plate this effect causes the stress to attack under an inward angle of 45°.

This is not the case for a free surface, since there the effect of the centrifugal forces acts in the opposite direction. In agreement with similarity arguments (Jähne, 1980), the compensation is nearly perfect: The water surface flows only slightly into radial direction, the maximal outward angular deviation in the viscous boundary layer is 20° for low wind speeds (Fig. 3.5). From this results a 40 % increase of the mass transfer rate at 1.2 m/s wind speed is estimated (Jähne, 1980) in agreement with the measurements (see Fig. 3.10).

The effect is inversely proportional to the friction velocity. So the critical layer for the mass transfer processes is not dominated by the centrifugal forces, not even in the small facility. In the gas exchange rates of the large facility the influence of the centrifugal forces cannot be observed at all.

Figure 3.6: Demonstration of the method to determine the water bulk velocity in our circular facilities. At time zero a small amount of CO_2-saturated water is injected. The graphs show the time traces of the signal from a conductivity probe for 7.2 m/s (a) and 2.7 m/s (b) wind speed.

Figure 3.7: Response of the water surface temperature on changing evaporation caused by turning on and off the gas flow through the air space of the circular wind-wave facility. Solid line: water surface temperature (arbitrary zero point); thin lines: solid: bulk water temperature, broken line: dry bulb temperature; dotted line: wet bulb temperature.

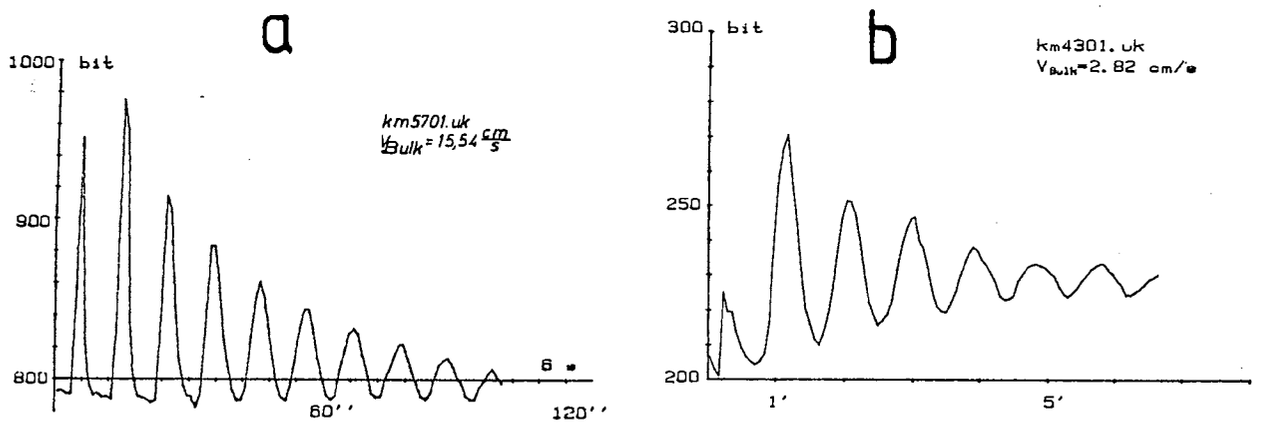

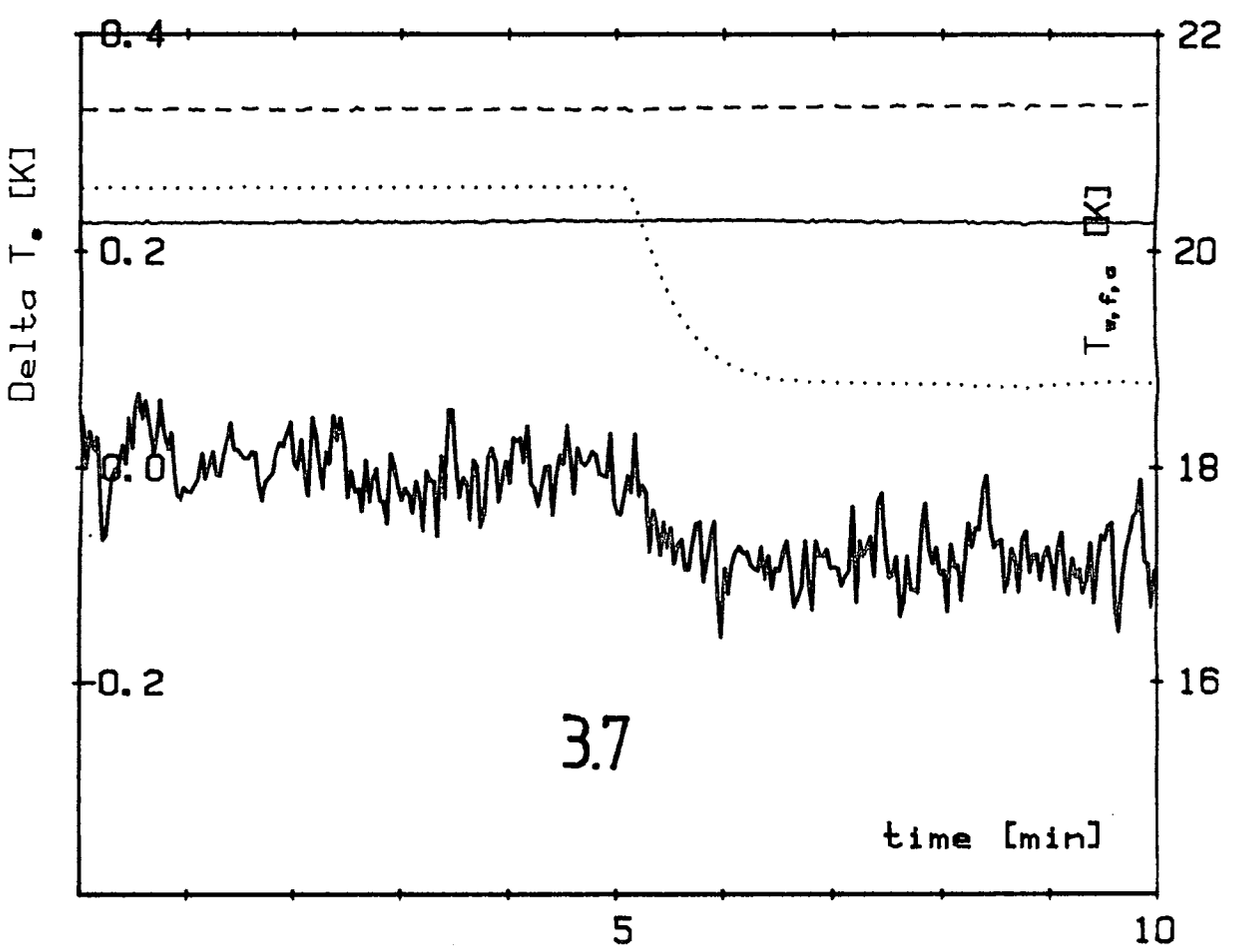

Measurement of the water friction velocity

Because of the centrifugal forces influence the friction velocity cannot be measured in the air. Instead, the water friction velocity can be measured directly by momentum balance (Jähne et al., 1979). The stress exerted on the water surface accelerates the water to a velocity at which the same amount of momentum is transferred to the walls and to the bottom. Once calibrated, the bulk water velocity is a direct measure of the friction velocity at the water surface. This calibration can be obtained by measuring the decrease of the water velocity after a sudden stop of the wind speed. If the wall and bottom friction velocity is proportional to the water velocity then the surface friction velocity is also proportional to the bulk velocity ($u_{*w}=bu_b$) and the proportional factor b is given by

$$u_b(t)/u_b(0) = (1 + t/\tau)^{-1} \quad \text{with } \tau=h\eta/[bu_b(0)]. \tag{3.3}$$

The measured velocity decrease is consistent with this universal law (Ilmberger, 1980). There are two regimes: With a smooth water surface the water velocity is much higher towards the outer wall (compare Fig. 3.4). So relatively more momentum is transferred to the wall ($\tau=\varrho u_*^2$) than with a uniformly rotating water bulk, and this results in a larger factor b. The transition to a uniformly rotating bulk occures with the onset of waves.Therefore in the transition region the accuracy of the friction velocity measurement is reduced.

The water bulk velocity is measured with a tracer method (Dutzi, 1984). A small amount of CO_2-saturated water is injected into the water. A conductivity probe "counts" the revolutions of this peak with the bulk velocity (Fig. 3.6). The decrease of the peak with time is a good measure for the uniformity of the radial velocity distribution.

Measurement of the heat transfer in water

In both circular facilities the gas flush rate through the tunnel can be controlled independently from the wind speed. This special feature can be used to measure the heat transfer in water with a simple but accurate method (Jähne, 1980). Turning on and off the gas flush changes the evaporation rate periodically. So the water surface cooling is also modulated periodically and can be followed by an IR-radiometer (Fig. 3.7). Due to the periodic changes systematic errors in the surface temperature are suppressed as well as the high

noise level of the radiometer (0.06 K, Heimann KT-16T). An accuracy of better than 0.01 K can be achieved by sufficient averaging. The evaporation rate is obtained from the gas flush rate through the air space of the facility and from the humidity. The latter is measured with a psychrometer carefully calibrated by Weißer (1980).

Measurement of the gas transfer velocity

Measurements with several gases have been carried out in our facilities in order to explore the Schmidt number dependence of the gas exchange. Since we used deionized water with a conductivity of less then 0.5 µS/cm, the CO_2-concentration in water could be measured continuously with a conductivity probe. The signal is proportional to the square root of the CO_2-concentration offering a large measuring range from 0.1 % to 100 % saturation (Jähne, 1980).

Huber (1984) designed a gas chromatographic systems to measure He, CH_4, and Kr concentrations with a sensitivity of 3 ppm, 12 ppm, and 24 ppm respectively. He made use of the gas-tightness of the wind tunnels and measured the increase of the gas concentrations in the air under evasion conditions in the small facility. With this technique he avoids any extraction of water probes.

Bösinger (1985) uses the same system in the large facility. But he measures the water concentrations of He, CH_4, and Xe putting a silicon rubber tube serving as the sampling volume of the gas chromatograph directly in the water channel of the facility. Due to the high gas permeability of silicon rubber (Müller, 1978; Heinz, 1985) the time constant for the equilibrium between the gas concentrations in the silicon tube and in the water is only a few minutes.

3.3 Transfer to a solid wall

The discussion of the boundary condition at the free surface (Chapter 2.7) has shown that the turbulent structure at a free, but surface film contaminated surface should be equal to the structure at a rigid wall. So the deviation of the measured transfer velocities from the one predicted for a solid wall is an indicator for the change of the boundary condition at a free surface. In order to put this comparison on a firmer base we have to make sure that the knowledge about the

transfer to a solid wall is well established.

The theory for a smooth wall has already been discussed at the end of chapter 2.8. A large number of measurements confirm the model. Hubbard and Lightfoot (1966), Mizushina et al. (1971) (both investigated channel flow), and Shaw and Hanratty (1977) (pipe flow) reported mass transfer measurements with electrochemical methods covering a wide Schmidt number range from 630 to 37,000. Flender and Hiby (1981) collected another set of data.

The results agree very well with each other (Fig. 3.8). The theoretical prediction (2.49) slightly overestimates the measurements of the first three investigators mentioned by maximal 20 % (Fig. 3.8a). The small, but significant deviation of the Schmidt number exponent n from 2/3 found by Shaw and Hanratty (1977) (Fig. 3.8c) will be analysed in chapter 3.5. Generally, the deviations from the model prediction are so slight that we can use it as a reliable base for the comparison with the transfer across a free surface.

Finally, the effect of surface roughness on the mass transfer to a solid wall has to be considered. Extensive studies of the heat transfer to rough walls have been carried out. As an example, the data from Sheriff and Gumley (1966) are shown in Fig. 3.9a. The graph shows the dimensionless transfer resistance in air as a function of the roughness Reynolds number ($h_r u_*/\nu$, where h_r is the height of the roughness elements) and illustrates the effects of the roughness on the transfer through the viscous layer: When in the transition region the obstacles start to jut out of the viscous layer, there is first a slight decrease of the heat transfer resistance (< 20 %). But then more momentum is transferred by form drag directly to the obstacles. This additional transfer mechanism has no analogue for heat and mass transfer, so that in the fully developed rough flow the transfer resistance increases with the roughness of the surface and is lower than in the smooth case. For higher Schmidt numbers (Fig. 3.9b) the relation between the transfer resistance and the roughness is quite similar. The only difference is that the increase of the transfer rate in the transition region is higher. But the enhancement does not exceed the smooth wall value by more than a factor 2.

Figure 3.8: Dimensionless transfer velocity k /u* at a smooth solid wall as a function of the Schmidt number Sc: (a) data collection according to Shaw and Hanratty (1977); (b) their own data showing a Schmidt number exponent n = 0.704 +- 0.013; (c) data collection from Flender and Hiby (1981). The solid line in all graphs marks the theoretical prediction according to $k_+=k/u*=12.2^{-1}Sc^{-2/3}$ (2.4)

a)

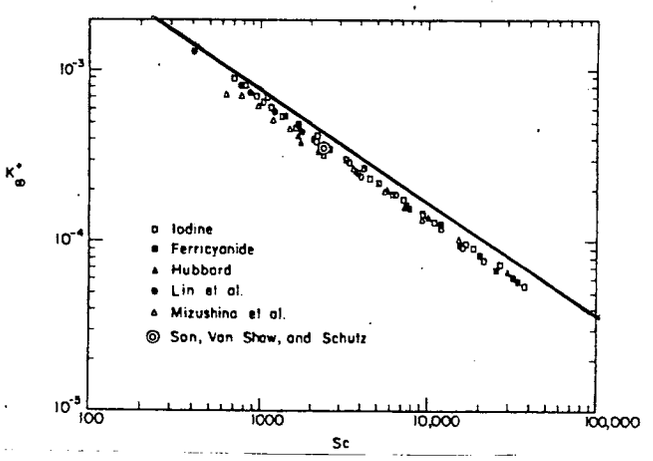

b)

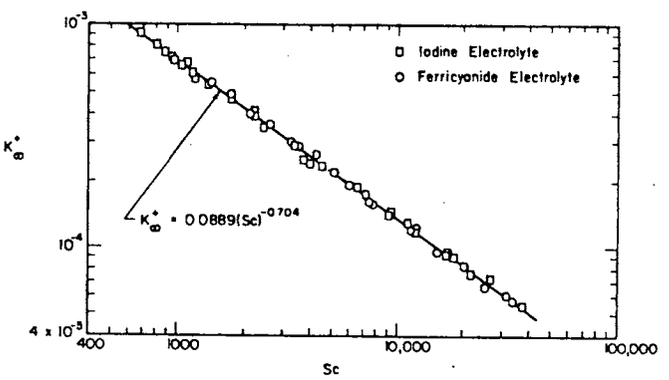

c)

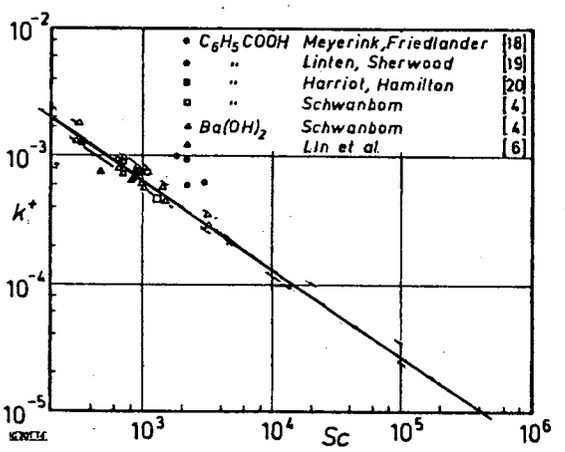

Figure 3.9: Dimensionless transfer resistance across the viscous boundary to a rough surface as a function of the roughness Reynolds number; (a) heat transfer data (Sc = 0.7) (Sherrif and Gumley, 1966); (b) and (c) mass transfer data (from O'Connor, 1984) for Schmidt numbers as indicated in the figure. The broken lines mark the smooth wall transfer resistance for comparison.

a)

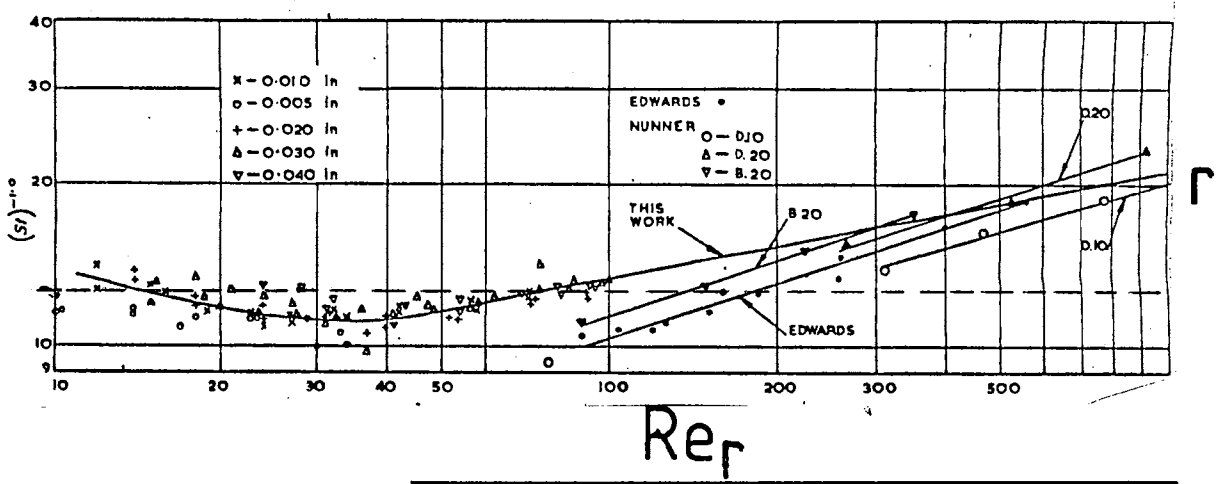

b)

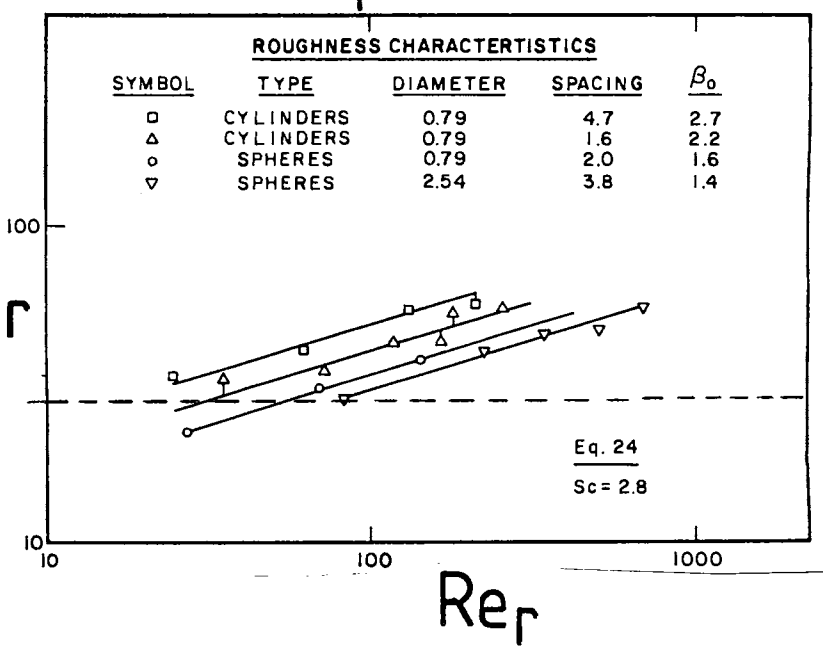

c)

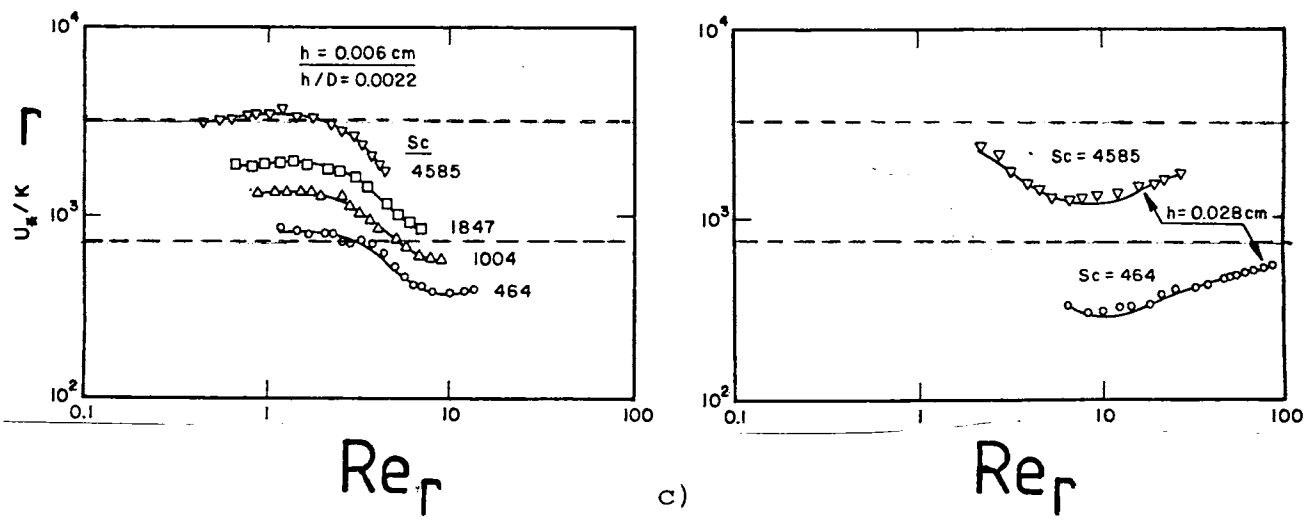

3.4 Transfer velocities in wind-wave facilities

A large number of gas exchange measurements have been carried out in the last decade in wind-wave tunnels of quite different sizes from a tiny channel with water depths less than 0.55 cm to the large I.M.S.T. wind-wave facility with a maximum fetch of 40 m and a water depth of 1 m. The basic features of the wind tunnels including the gas tracers used in the experiments are summarized in Tab. 3.1. The transfer velocities are normalized to a Schmidt number of 600 (CO_2 at 20 °C) using a square root dependence of the transfer velocity on the Schmidt number (see next chapter). The correction is not large, since the available data only span a Schmidt number range from 470 to 1180.

According to the remarks in the previous chapter the transfer velocities k are presented in dimensionless form as $k_+=k/u_*$ in order to study the deviation of the transfer process at the free surface in relation to the same process at a solid wall, where k_+ is only a function of the Schmidt number. Only in our own studies in the circular facilities u_{*w} is measured directly, in all other experiments u_{*w} has to be determined from the the friction velocity in air assuming stress continuity at the surface.

Fig. 3.10 presents k_+ as a function of the friction velocity in water. We start the discussion with the results obtained for a smooth surface in our small circular wind-wave facility. The circular facilities show the exceptional feature that wave generation is extremely sensitive to surface film contamination. This effect is not surprising, because, in contrast to linear tunnels, the surface film cannot escape to the beach at the end of the tunnel.

We did not realize this effect in the first gas exchange experiments in the small circular facility (Flothmann et al., 1979; Münnich et al., 1978; Jähne et al., 1979). So the water surface was entirely flat up to a critical wind speed of 8 m/s (u_{*w} = 1.5 cm/s), where a sudden transition to a completely rough and wavy surface occured (marked by an arrow in Fig. 3.10; in the Hamburg tunnel also experiments with an artificial surface film have been carried out (B78, x); the film breaks off at the same friction velocity as in our tunnel). The gas exchange results obtained with the smooth, surface film contaminated surface agree well with the rigid wall prediction (Fig. 3.10c). In

conclusion, they verify the theoretical considerations that the turbulent structure at a free, but surface contaminated surface and a rigid wall is equal.

Meanwhile, the wind tunnels are equipped with a facility to suck the water surface layer, which proves to be an efficient method to remove surface films. With a carefully cleaned surface, waves occur at about the same or even a lower wind speed as in linear facilities. Now at the same friction velocity, but with waves on the surface, up to 5 times higher gas exchange rates are obtained. This direct comparison illustrates the drastic change in the turbulence structure at a wavy water surface.

All other results show similar enhancement of the mass transfer process: compared to a rigid wall, mass transfer through a free wavy surface is 2.5 to 10 times faster than momentum transfer. The scatter is considerable and obviouslyx caused by differences in the wave field. It is a really a pity, that no detailed wave data (especially on capillary waves) are available from almost all investigations in so many different tunnels. The conclusions which can be drawn from this comparison are, therefore, rather poor:

Firstly, friction velocity is not the only parameter controlling mass transfer across the aqueous viscous boundary layer. Different surface conditions may change the exchange rate by a factor of 4.
Secondly, with the onset of the waves at a critical friction velocity in water between 0.2 to 0.4 cm/s the gas exchange rate varies roughly quadratic with $u*$. This rapid increase becomes smaller again and seems to reach saturation where the transfer velocity is proportional to the friction velocity. The onset of the sharp increase and the level of the saturation range seem to depend on the wind tunnel geometry and the surface contamination.

Fig. 3.10 also shows the heat transfer rates across the aqueous boundary layer. Again, the measured transfer velocities exceed the values expected for a smooth water surface, but the enhancement is lower. This leads to the conclusion that the 2/3 Schmidt number exponent has decreased to a lower value.

Table 3.1: Basic features of the wind-wave facilities previously used for gas exchange experiments including information about the experimental conditions. The abbreviation added to the reference is used in Fig. 3.10 as a key to the data points.

water fetch [m]	channel size width [m]	depth [m]	range of wind speeds [m/s]	tracer	T_w [°C]	Sc	reference
9.0	0.3	<0.0055	4 - 10	O_2	20	470	McCready and Hanratty (1984) M84 McCready (1984)
4.5	0.3	0.10	3.3 - 8.2	O_2			Liss (1973) L73
2.4	0.6	0.60	3.0 - 11.6	C_6H_6	20	1020	Cohen et al. (1978) C78
6.0	0.6	0.60	6.0 - 13.2	C_6H_6	20	1020	Mackay and Yeun (1983) MY83
3.8	-	0.30	2.6 - 10.2	O_2	20	470	Sivakumar (1984) S78
8.0	0.50	0.30	2.5 - 9.2	O_2	20	470	Liss et al. (1981) L81
			3.1 - 11.5	N_2O	14-19	~770	Merlivat, Memery (1983) MM83
18.0	1.0	0.5	3.2 - 15.5	CO_2	10	1010	Broecker et al., (1978) B78
40.0	2.6	1.0	2.5 - 13.8	Rn	23	690	Jähne et al., (1985a) J85

Figure 3.10: Comparison of mass transfer results from different wind-wave facilities. The dimensionless transfer velocity $k_+ = k/u_{*w}$ is shown as a function of the friction velocity u_{*w} in double logarithmic plots. The solid line in all graphs marks k_+ at a solid wall for comparison. Explanation of data key see Tab. 3.1. The large letters D and SR show the diffusion and surface renewal model prediction (chapter 2.8) of the transfer velocity based on the velocity profile as measured by Sivakumar (1984).

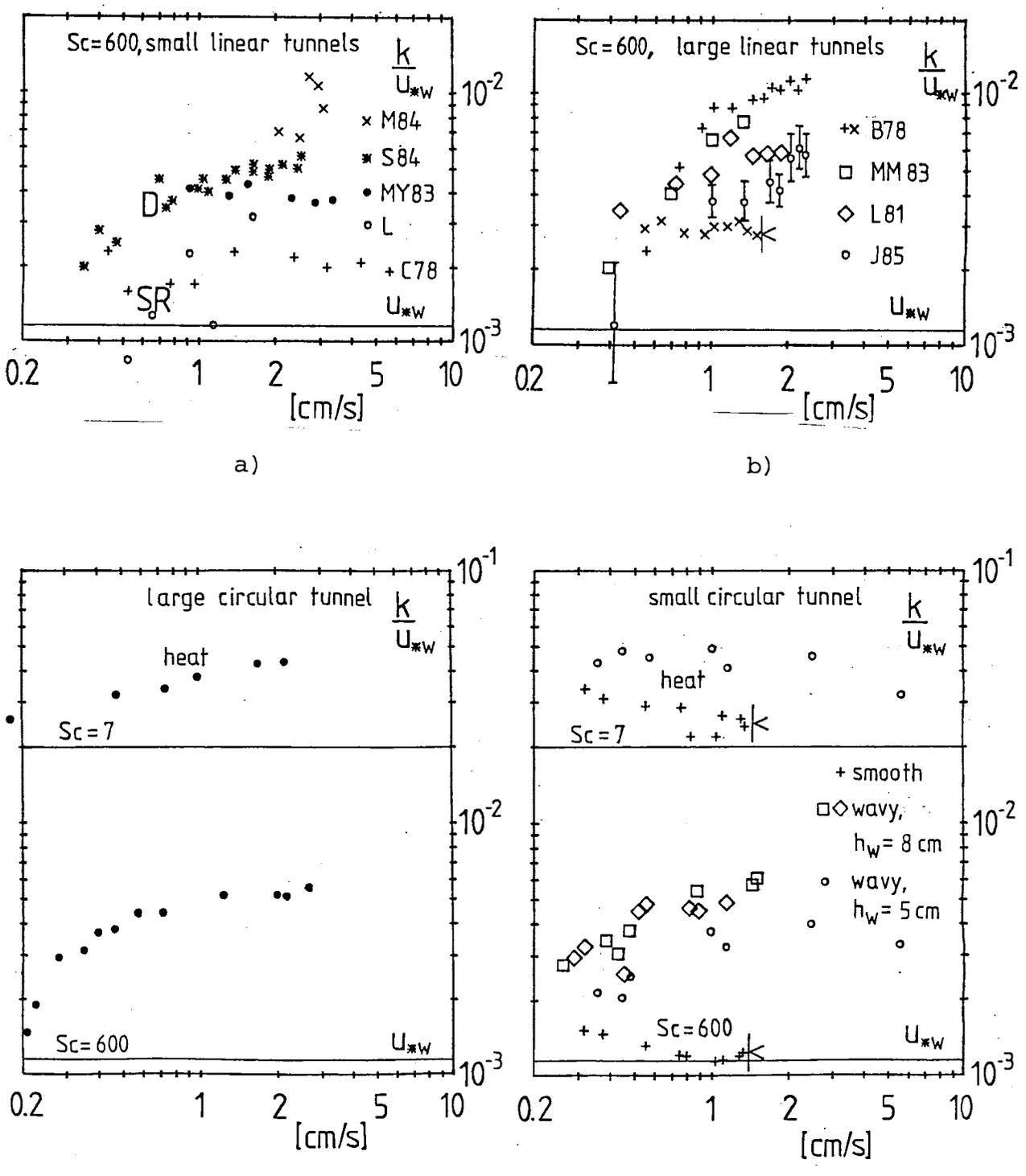

Figure 3.11: Diffusion coefficients for gases dissolved in pure water according to measurements of Heinz (1985).

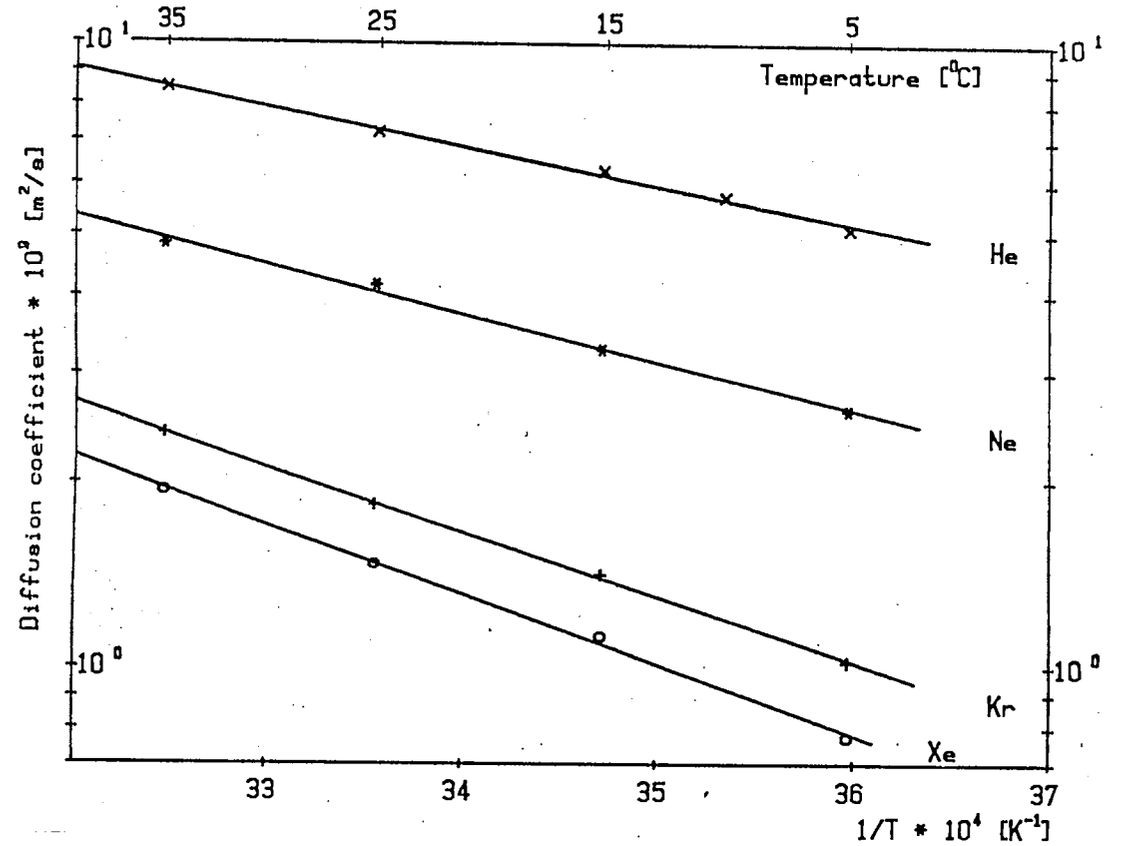

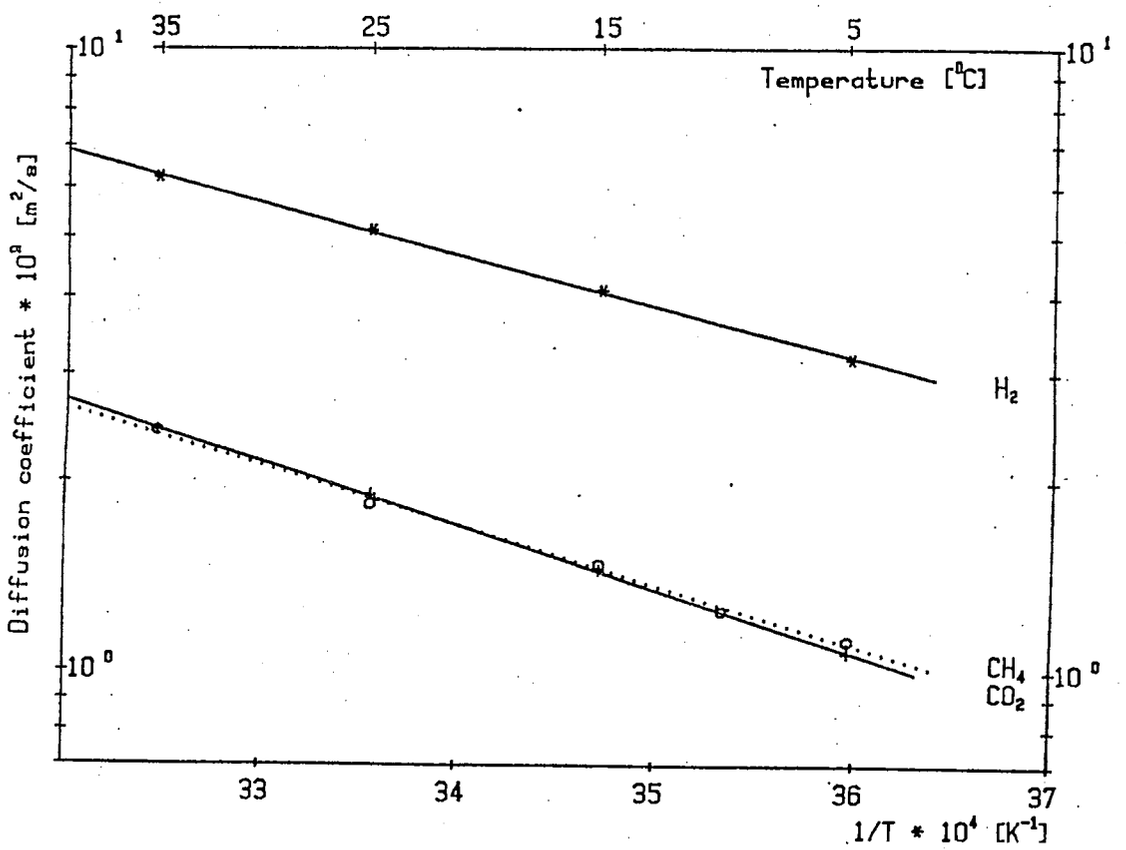

3.5 The Schmidt number dependence of the transfer

A change in the Schmidt number exponent indicates a change of the boundary conditions at the water surface, reflecting the equilibrium between the tendency of turbulent eddies and waves to put the water surface out of shape and the restoring forces caused by surface contaminations. If the turbulence intensity increases, the exponent decreases, thus being a monitor of the ratio of both opponents.

Sufficiently accurate measurements of the Schmidt number dependence of the transfer across a free aqueous boundary layer, dominated by shear stress has not been reported so far. This is not surprising, since they require both, accurate measurement of the transfer velocity and an exact knowledge of the diffusion coefficient (Jähne, 1980). The available data of diffusion coefficients for gases dissolved in water are very limited in accuracy and seem to be influenced by systematic errors (Dietrich, 1983). So the first successful determination of the Schmidt number exponent has been obtained by the comparison of heat and CO_2 transfer velocities (Jähne, 1980).

Meanwhile, new measurements of the diffusion coefficient have been carried out in our group. We developed a modified Barrer method (Dietrich, 1983), checked it carefully for possible systematic errors and measured the diffusion coefficients of the following gases in a temperature range from 5 to 35 °C: He, H_2, Ne, CO_2, CH_4, Kr, and Xe (Heinz, 1985). There is much evidence that within the experimental error of about 5 % the coefficients are free from systematic errors. The data are summarized in Fig. 3.11 and are the basis for the Schmidt numbers listed in Tab. 2.3.

Before presenting our own results, previously determined Schmidt number exponents shall be discussed.

Literature review

Siems (1980) found a 1.15 times higher transfer velocity for O_2 than for CO_2. Because of the low difference in the diffusion coefficient ($D(O_2)/D(CO_2)=1.26$) the error of the exponent is too high: $n = 0.6 \pm 0.2$. Ledwell (1982, 1984) concluded from He, CH_4, and N_2O gas exchange measurements that the transfer velocity varies with about the 1/2 power of the diffusion coefficient. But he used a much too low diffu-

Figure 3.12: Schmidt number dependency of the transfer velocity across the aqueous viscous boundary layer. The Schmidt number exponent n is shown as a function of the friction velocity u_{*w}; (a) small circular facility; circles: obtained from heat and CO_2 transfer measurements (Jähne, 1980); squares: from He and CH_4 gas exchange measurements (Huber, 1984); (b) large circular facility; circles: Bösinger (1985) from He and CH_4 gas exchange measurements; *: from heat and CO_2 transfer velocities

Figure 3.13: Temperature dependence of the gas exchange rate of CO_2. The lines mark the measured values at the different temperatures, whereas all data are shown corrected for a Schmidt number of 600 with an exponent n of 0.52 obtained by a least square fit of all data (from Dutzi, 1984).

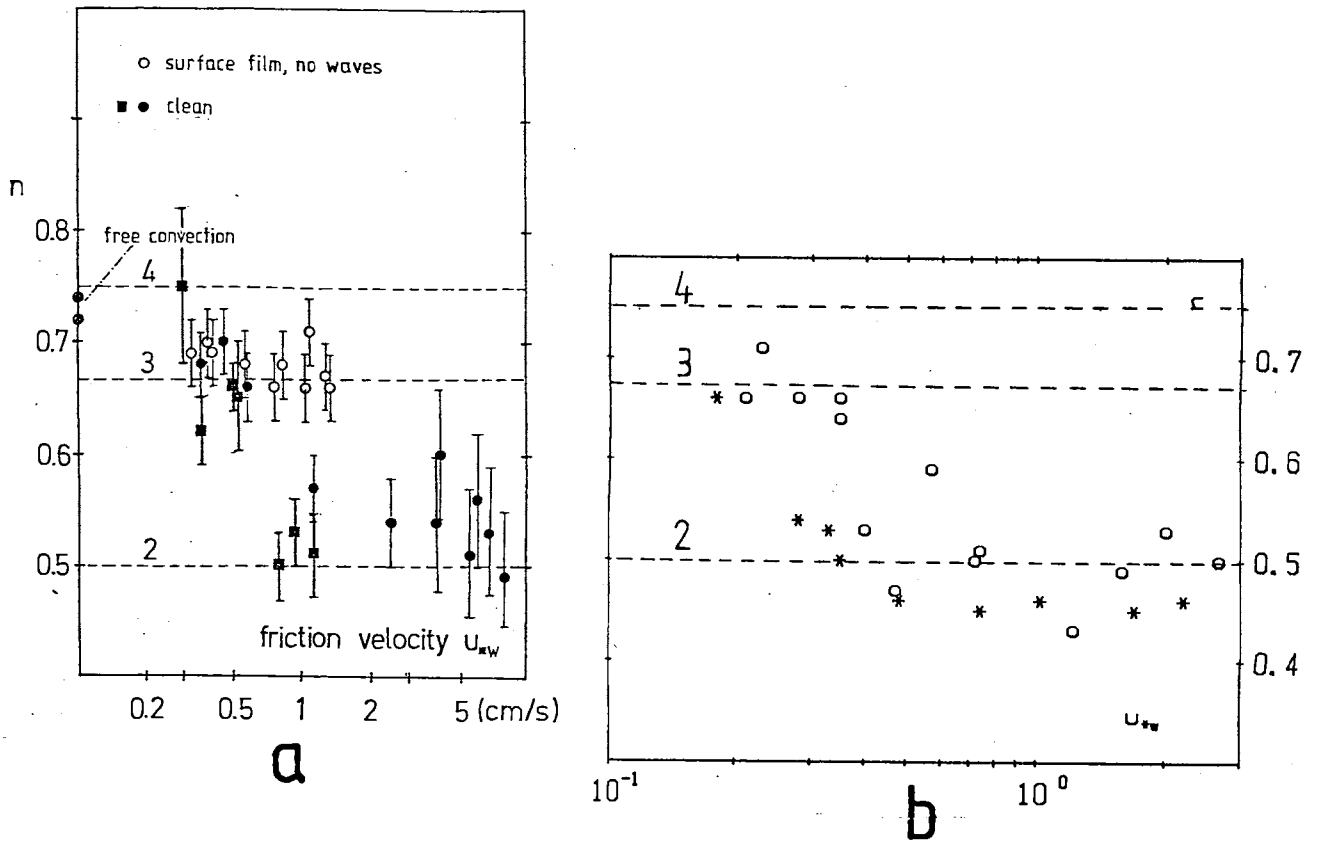

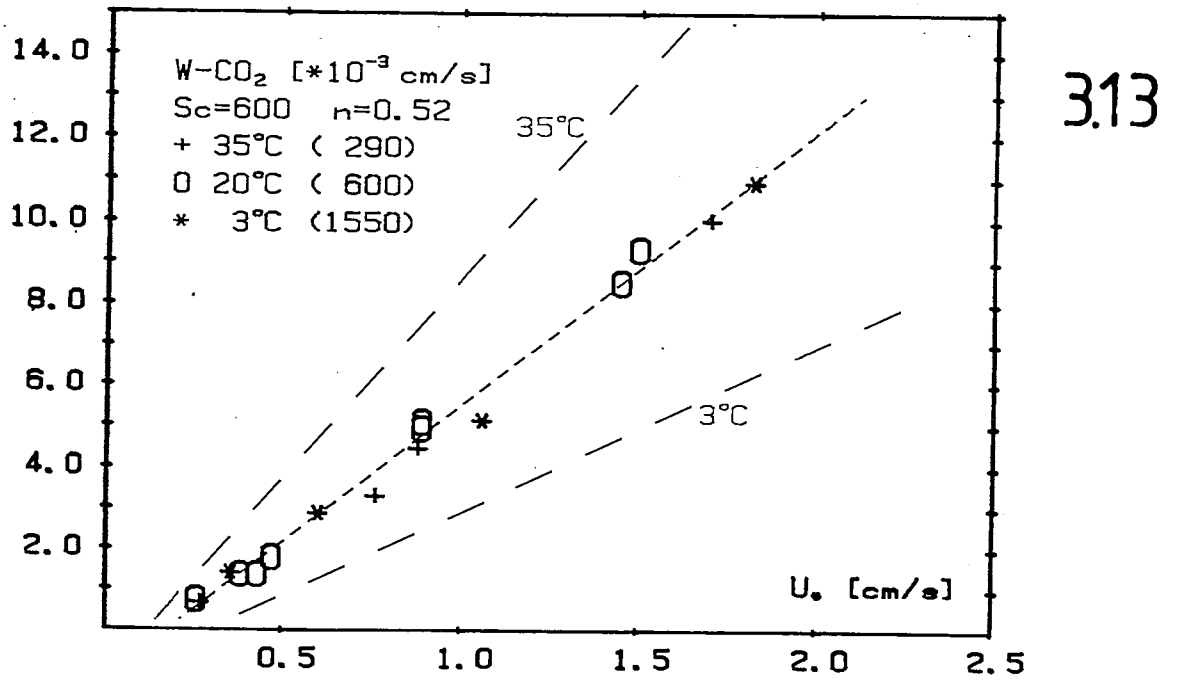

3.13

sion coefficient for He. A careful analysis of his data shows that they are difficult to interpret, since he observed a quite strong fetch dependence of the gas concentrations in water during his experiments, which may have caused systematic errors.

Finally, Torgersen et al. (1982) measured the He and Rn gas exchange ratio in a small lake to be 3.8 ± 0.4 and calculated an exponent of 1.22. But they also used an erroneous He diffusivity. A recalculation of their results with our new diffusivity data yield 0.73 ± 0.15. In conclusion, all previous determinations of the Schmidt number dependency are too inaccurate.

Own data

We used two methods to determine the Schmidt number exponent. Besides the comparison of the transfer velocities for heat and CO_2, we simultaneously measured He and CH_4 gas exchange rates. The calculated exponents from both methods and from both circular facilities are shown in Fig. 3.12 as a function of the friction velocity. The data for a smooth contaminated surface agree well with the expected 2/3 power. On a clean surface a gradual decrease is found to an exponent of 1/2.

Temperature dependence of the gas exchange

The Schmidt number for tracers in water varies strongly with temperature (compare chapter 2.6). By this effect the gas exchange rate depends on the temperature. So the temperature dependence of the gas transfer velocity of a single tracer may be used to determine the Schmidt number exponent. But other parameters may also be influenced by the temperature. Dutzi (1984) studied the temperature dependence of CO_2 gas exchange, momentum transfer, and water surface waves in the small circular tunnel.

Surprisingly he found no significant temperature variation of the waves even at the high frequency end, which might be assumed to show variation with the molecular viscosity. But obviously viscous damping is a negligible effect even for the high frequency end of the waves, and attenuation by a turbulent process seems to be dominant. This result is a hint for a strong interaction between waves and turbulence (further discussion see chapter 5).

Due to the constant wave field the momentum input does not change

either and the temperature variation of the gas transfer is only caused by the Schmidt number variation with an exponent agreeing with our other measurements (Fig. 3.13).

3.6 The relation between the velocity profile at the surface and the mass transfer velocity

The theoretical considerations in chapter 2.8 revealed a general relation between the velocity profile at the surface and the mass transfer rate (2.38, 2.39; 2.42, 2.43). If the deviation from the linear profile at the very surface can be measured accurately enough, then both the Schmidt number dependence and the absolut transfer velocities can be calculated for the diffusion model and surface model respectively.

Unfortunately, there are only two investigations of the velocity profile at the surface which are accurate enough. McLeish and Putland (1975) measured the velocity profiles with tiny hydrogen bubbles. At a wavy surface they obtained only one profile at 3.82 m fetch and 5.5 m/s wind speed. Coantic's (1985) analysis of the profile yields a cubic deviation from the linear surface profile with a constant α_3=1.8 10^{-2}. Sivakumar (1984) used surface floats of different sizes. The analysis of his profile at 3.6 m/s yields α_3= 1.5 10^{-2} +-30 % in good agreement with McLeish's profile.

Since Sivakumar also measured the gas exchange rate, the measured gas transfer velocity can be compared with the theoretical predictions. The diffusion model (2.38) yields a 1/2 power variation of the transfer velocity with the Schmidt number: k_+=0.077 $Sc^{-1/2}$ and the surface renewal model a 2/3 power and k_+=0.83 $Sc^{-2/3}$. Fig. 3.10b shows that the measured gas transfer velocity better agrees with the diffusion model.

Additional support to this finding comes from our measurements of the Schmidt number dependence. Sivakumar measured the profile at a friction velocity $u*_w$ of 0.67 cm/s where the Schmidt number exponent has already considerably decreased from 2/3 to 1/2 (Fig 3.12). If we further take into account the boundary condition calculations of chapter 2.7, we may conclude that the turbulent structure is essentially two-dimensional. All these facts suggest the existence of large two-dimen-

sional rolls, which may interact with the waves and/or the shear flow at the surface producing bursts of small eddies. But because of the large errors in the velocity profile measurements further experimental verification is needed.

Nevertheless, these considerations show that simultaneous gas exchange measurements including the Schmidt number dependence and careful velocity profile measurements seem to be one promising way to investigate the turbulent structure at a free surface. It is evident from the data comparison in chapter 3.4 that the sole measurement of the mean transfer velocity and the friction velocity, as it has been done in nearly all previous investigations, yields no insight into the turbulent structure.

The decrease of the Schmidt number exponent from 2/3 to 1/2 not only indicates a drastic change in the turbulent structure, but also partly explains the enhancement of the gas exchange: If we simply assume that momentum transfer is not changed, i. e. that β remains constant in (2.20), then the exponent decrease leads to a 2.9 times ($Sc^{1/6}$) enhanced gas exchange rate. Since considerably higher enhancements have been measured, we can conclude that the resistance for momentum transfer in the aqueous boundary layer, i. e. β in (2.20), is also decreased significantly.

4. THE INSTANTANEOUS TRANSFER VELOCITY

Turbulent processes are not only characterized by their mean values, but essentially also by the amplitude and the spectrum of their fluctuations. In this chapter we shall report our attempts to determine the instantaneous and local transfer velocity at a free surface and demonstrate that such measurements will really be a step ahead. They provide another step towards a deeper insight into the turbulence structure and further offer the possibility to measure local transfer rates both in wind tunnels and in the field.

4.1 The relaxation time for the mass transfer process

Our first step towards measurement of an instantaneous transfer velocity were attempts to make the mass balance method faster. The idea is to derive the gas flux across the interface from the mass balance in air.

In this case the concentration increase of a tracer gas in the air of the gas-tight wind tunnel is to be measured. A simple estimate shows that from this increase the transfer velocity can be obtained with a much faster response time: The mass balance in the closed air space of the wind tunnel is simply given by

$$V_g \dot{c}_g = F_g k c_l \quad \text{when } \alpha c_g \ll c_l, \tag{4.1}$$

i. e. the transfer velocity varies with the time derivative of the gas concentration. Equation (4.1) can be rewritten using the time constant τ for gas exchange in the liquid (3.2)

$$\dot{c}_g = h_l/h_g \; c_l/\tau. \tag{4.2}$$

Since the ratio h_l/h_g is approximately 1 in our large facility a 1 % concentration increase (relative to the concentration in water) takes only 1 % of the time constant for gas exchange in the water. This time constant is typically in the order of an hour. Since CO_2 has a solubility of about 1, with CO_2-saturated water concentration increases of up to 20,000 ppm/min can be achieved. The detection limit of the special heat conductivity gauge we used (Heinz, 1985) was about 100 ppm/min at

a response time of a few seconds.

So the response time for the gas transfer measurements is only limited by the time necessary to transport the tracer from the interface to the measuring level in the air. Evaporation measurements in the large wind wave facility give typical transfer velocities of 1 cm/s. At least 2/3 of the transfer resistance in the wind tunnel lies in the viscous sublayer. Consequently, the time constant for the mixing in the bulk of the air space can be estimated to be lower than 10 s.

In summary, the gas transfer velocity can be measured by the increase of the tracer concentration in air with a fast response time of less than 10 s. The procedure of our measurements was as follows: after the water had been saturated with CO_2, we flushed the air space of the tunnel with air to remove the CO_2 from air. The CO_2 concentration in air decreases to an equilibrium concentration $c_g/c_l=\tau_f/\tau$, where τ_f is the time constant for flushing of the air space, which is about one minute. When the experiment is started, the flushing is stopped by closing the air space of the tunnel.

We used this technique to study the relaxation time of the gas transfer process. The idea was to learn how fast the gas exchange decreases when the wind is turned off and how fast it increases when the wind is started in order to test several hypotheses about the critical parameters for the gas exchange (compare chapter 5.2). So we simultaneously measured the gas transfer rate and wave slope spectra (chapter 5.3).

Figure 4.1: Time traces of the CO_2 transfer velocity and the wave slope for changing wind speed conditions as indicated. Line type key for the wave slope signal: thick line: total mean square slope; the thin lines are selected frequency ranges; solid: 2 - 4 Hz; dashed: 4 - 8 Hz; dotted: 32 - 64 Hz

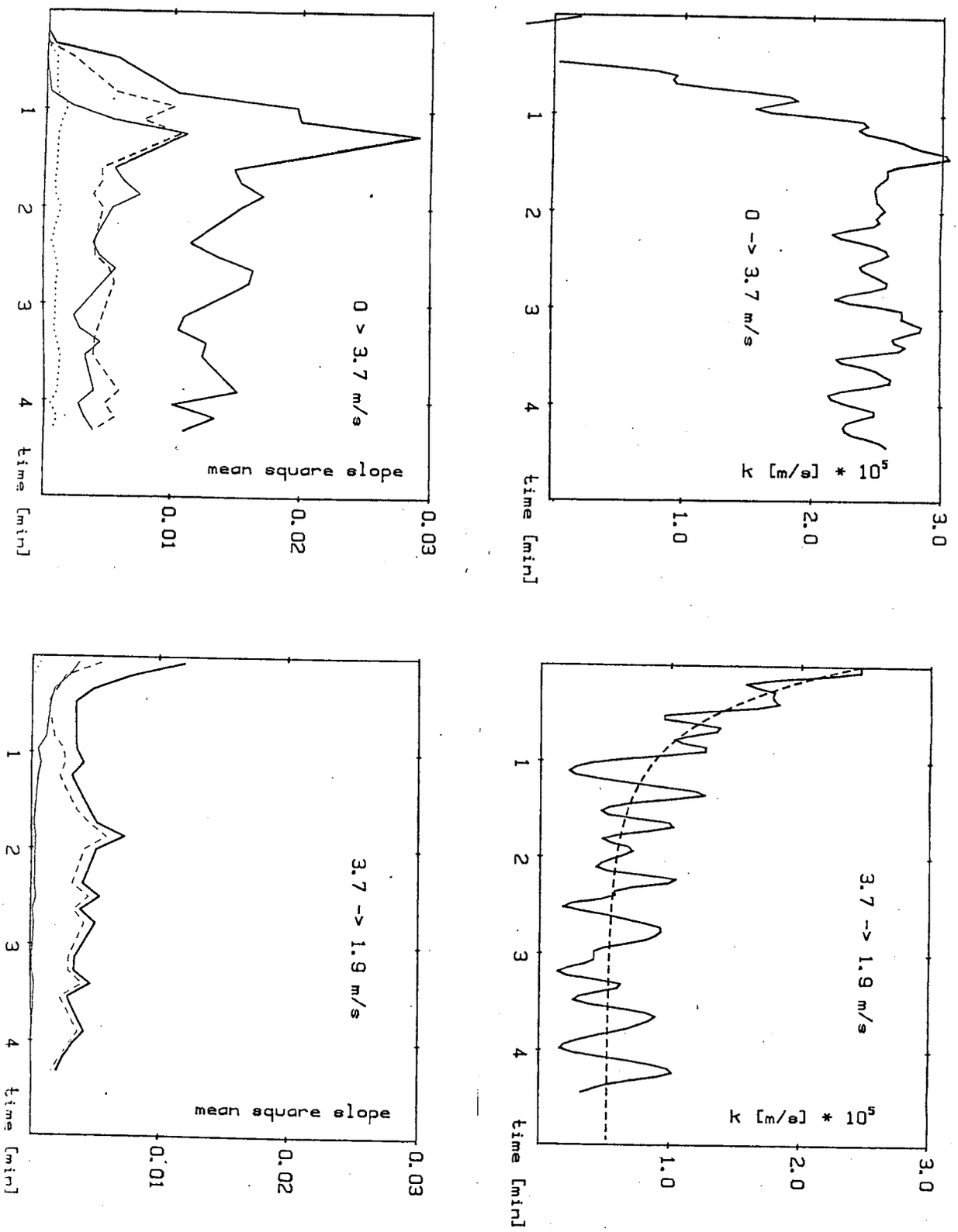

Figure 4.2: Time traces of the CO_2 transfer velocity and the wave slope for changing wind speed conditions as indicated. Line type key for the wave slope signal: thick line: total mean square slope; thin lines are selected frequency ranges; solid: < 2 Hz; long dashed: 2 - 4 Hz; short dashed: 4 - 8 Hz; dotted: 32 - 64 Hz

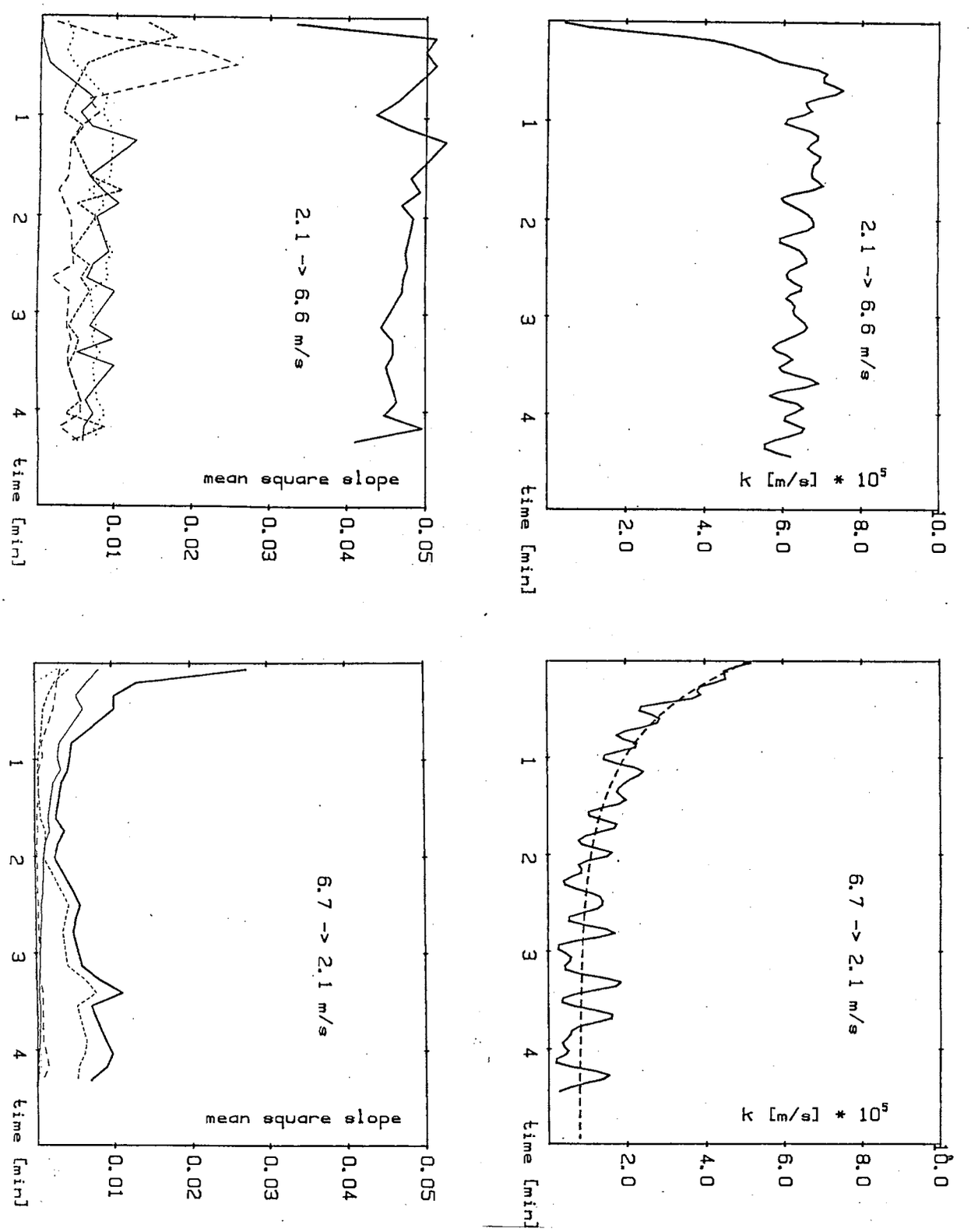

The results are shown in Fig 4.1 for a sudden start of the wind speed from 0 to 3.7 m/s and a sudden decrease from 3.7 m/s to 1.9 m/s and for the change from 2.1 to 6.6 m/s and back in Fig. 4.2. (The time constant for the wind speed change is about 1 s. The light paddle-ring of the large wind-wave facility can be accelerated to full wind speed within 2 s.) The data reveal a striking asymmetry:

When the wind is turned on, the transfer velocity increases parallel with the mean square slope of the waves, whereas the large gravity waves develop with a considerable time lag. This clearly indicates that the scale of the waves is not important, but only their mean square slope. In addition an overshoot effect is observed for both the mean square slope and the transfer velocity, which is larger for the lower wind velocity.

When the wind is turned off, the effects are entirely different. The gas transfer rate relaxes slowly with a time constant of 0.59 +- 0.08 min (3.7 -> 1.9 m/s) and 0.77 +- 0.06 min (6.7 -> 2.1 m/s) respectively. The capillary waves decay so fast that it could not be detected with the time resolution of the wave measurement (8 s). But also the mean square slope and the higher frequent gravity waves decay much faster than the gas exchange rate. The decrease of the gas exchange roughly varies with the decay of the dominant gravity waves.

At first glance, this seems to be contradictory to the behaviour of an increasing wave field. But the inconsistency is being cleared, if we assume that with the development of the large gravity wave a turbulent flow structure of similar scale develops. This is not unreasonable, since the instability of the large waves must produce a similar scale turbulence structure. The efficiency of the turbulent structure associated with the waves seems not to depend on their length scale. But once generated to a certain length scale it decays with a time constant characteristic for this length and consequently equal to that of the largest waves.

To avoid any misunderstanding: It is not believed that this large scale structure directly renews the surface layer. This process would be too slow because of the low time scales of the large structure. It is rather assumed that it triggers intense small scale turbulence in the surface layer.

The experiments also showed that bottom shear induced turbulence is not the cause for the slow decay of the gas exchange rate, since the time constant for the velocity decrease (3.3) is much lower: 5 min for 3.7 m/s and 2.5 min for 6.7 m/s wind.

Though these measurements are reliable, final evidence for the proposed turbulence structure is only given, when they can be visualized. This is why we concentrated our efforts on the visualization of the waves (chapter 5) and the mass boundary layer (chapter 6).

4.2 The forced flux method

The method discussed above to determine the transfer velocity is still too slow, if we want to analyse the dynamics of the transfer across the boundary i. e. the fluctuating instantaneous transfer velocity. This can easily be seen by the time constant t^* for the transfer process across the boundary layer as given by (2.9): For the conditions discussed above it is: 2.8 s at 3.7 m/s and 0.4 s at 6.7 m/s wind speed. Only beyond this time scale the fluctuations in the transfer velocity decay off.

In this paragraph a new method is discussed, which is capable to measure the instantaneous transfer velocity. In the next paragraph its realization for heat transfer is described, and first measurements are shown to verify the considerable advance that can be achieved with the new technique.

The basic idea: control of the flux density

The new technique is based on a simple idea, to be explained most easily by using the definition of the transfer velocity (2.6), which is given by the ratio of the flux density and the concentration difference. The conventional mass balance methods (see chapter 3.1) let the system run as it does by the given concentration difference and determine by mass balance of the gas or the liquid phase the flux density resulting from the given concentration difference.

The new method is simply the inversion of this procedure. We force a constant tracer flux onto the interface. Then, since the bulk concen-

tration remains constant, by definition the surface concentration directly represents the instantaneous transfer velocity. Because of the small time scales involved, the condition of a constant bulk concentration is fulfilled easily: the large bulk volume makes concentration changes slow. So the transfer velocity determination simply needs a surface concentration measurement and calibration of the flux density.

At first glance, it may look like a poor investigation of the boundary layer processes, since we only measure the surface concentration. But this turns out to be too pessimistic. First, the fluctuations of the transfer velocity yield information about the frequency spectrum of the turbulent fluctuations which can be compared with model predictions and will allow a distinction of large and small eddy models, since the frequency of the eddies is correlated with their length scale. Second, the method of controlled flux density allows periodic variation, thus providing an adequate tool for investigating the dynamic response of the boundary layer.

First we consider the horizontal length scale of the new method. Due to the surface drift caused by the wind stress a water surface element travels a characteristic length scale x until it is in equilibrium with the forced flux. This length scale is given to be the product of the time scale t_* of the transfer and the surface drift velocity

$$x = t_* U_S. \tag{4.3}$$

With typical drift velocities of 10 cm/s and a time constant of 1 s the length scale is in the order of 10 cm. So the footprint of the forced flux density must have a size of several length scales x.

Analysis of the frequency response for mass transfer across the boundary layer

Conventional measuring techniques yield no direct information about the time constant for the transfer. It can only be calculated by the means of (2.9) from the measured transfer velocity. With the forced flux method, however, it can be measured directly.

The idea of controlled flux density can be extended to the use of a periodically changing flux density. As long as the frequency ω ($\omega=2\pi f$)

is low compared with t_* (i. e. $\omega t_* << 1$) the amplitude of the surface concentration remains constant at the equilibrium value. If the frequency is increased, first it will lag behind the forced flux and then decrease with increasing frequency. The larger the frequency, the lower the penetration depth. It is easily seen in this way that the decrease of turbulence towards the surface is reflected in the functional dependence of the amplitude decrease and the phase shift with changing the frequency.

The basic question is how sensitively the amplitude decrease and the phase shift depend on the turbulent structure. In order to answer this question, we solved the unsteady transport equation for the diffusion and surface renewal models (2.35) with the boundary condition of a periodic varying flux density at the surface. The equations can be solved analytically only for the classical surface renewal and film model. For the other cases we used a simple box model and solved them numerically. The calculations are outlined in Jähne et al. (1985b). Only the results are presented here.

Figure 4.3: Amplitude damping (upper graph) and phase shift of the surface concentration response to a forced flux density at the surface. The figure shows the results of numerical calculation for surface renewal models (thick lines) and diffusion models (thin lines). The line type marks the Schmidt number exponent n: solid: 0.5; long-dashed: 0.6; short-dashed: 2/3; dotted: 3/4.

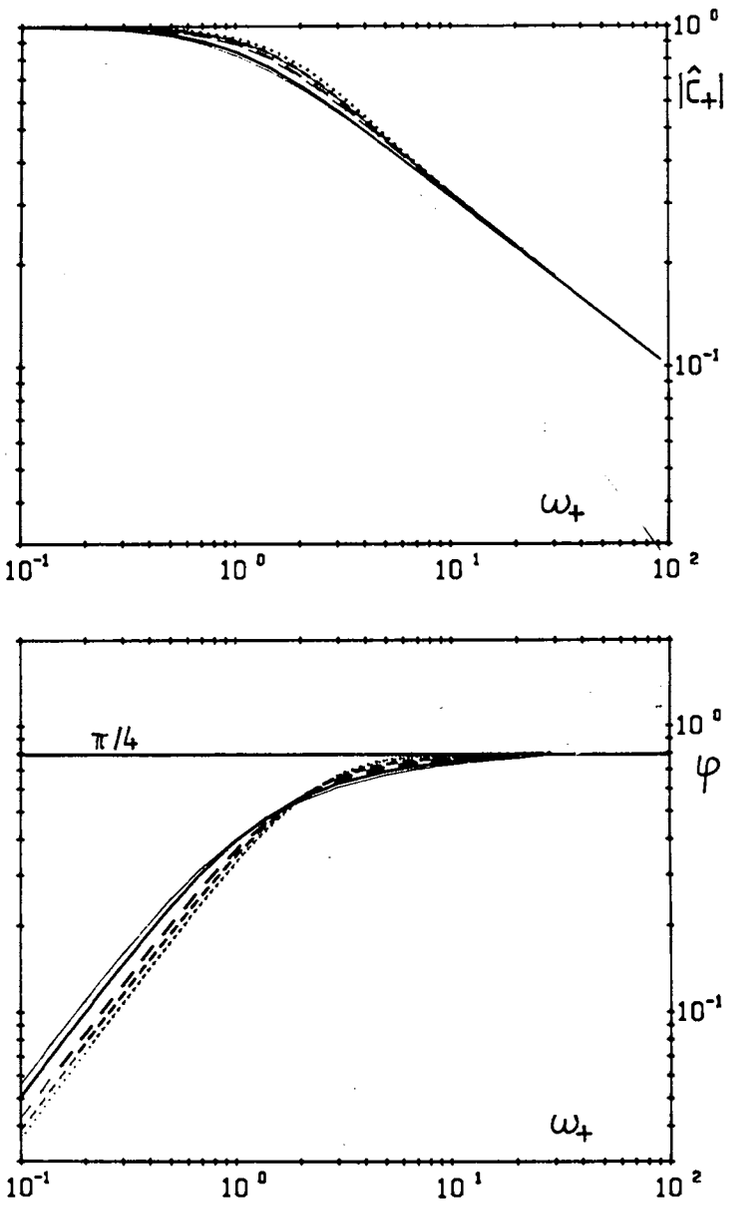

The results for the amplitude damping and for the phase shift between flux density and surface concentration are shown in Fig. 4.3 as a function of the dimensionless frequency $\omega_+ = \omega t_*$. For large frequencies ($\omega_+ > 10$) all models agree on a constant phase shift of $\pi/4$ and an amplitude damping proportional to $\omega_+^{-1/2}$. This coincidence is caused by the fact that at high frequencies the penetration depth is much lower than the boundary layer thickness. This thin region is solely controlled by molecular diffusion.

This model independent decrease in the amplitude is an important fact. It allows the direct determination of the time constant t_*: The $\omega_+^{-1/2}$-damping line crosses unity at 1, i. e. the real measured $\omega^{-1/2}$-line meets the horizontal line of the undamped amplitude at t_*^{-1}. It is important to note that it is not necessary to know the flux density in order to determine t_*. On the contrary, it is possible to calibrate the flux density in this way, since for high $_+$ the concentration amplitude is generally given by

$$c_s = j \,/\, (D\omega)^{1/2}. \qquad (4.4)$$

The only unknown in this equation is the flux density.

For low frequencies the amplitude remains constant up to $\omega_+ = 0.3$ and the phase shift φ increases linearly with ω_+ up to $\omega_+ = 0.5$. Even for such low frequencies the phase shift reaches already 1/4 to 1/3 of its maximum value. From Fig. 4.3 it is obvious that for low frequencies the phase shift distinguishes the different models most clearly. But it can also be seen that the structure of the turbulence can hardly be detected by the phase shift: The diffusion and surface renewal models more or less coincide for the same Schmidt number dependence of the transfer velocity.

Figure 4.4: Phase shift φ/ω_+ between the flux density and the surface concentration for small frequencies as a function of the Schmidt number exponent n. Thick line, •: surface renewal models; thin line, +: diffusion models

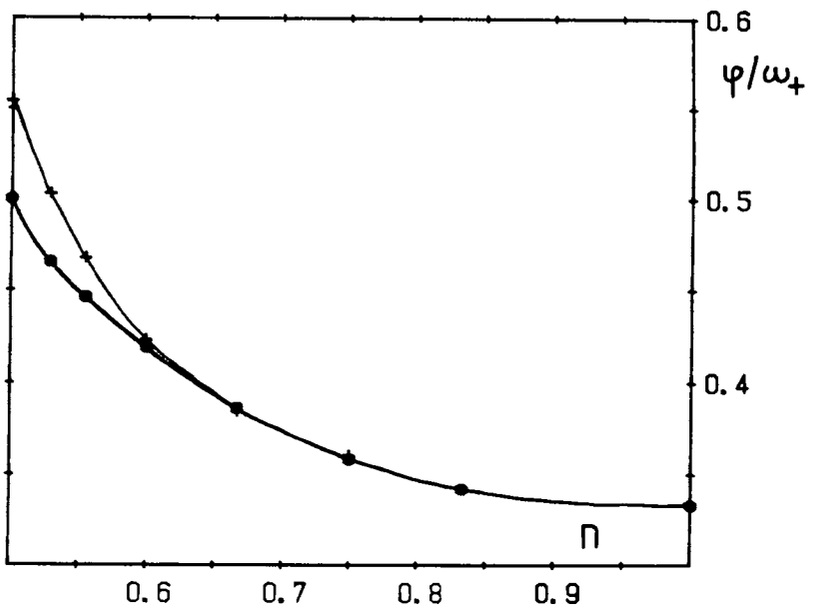

So the phase shift as well as the Schmidt number exponent only integrally reflect the general decrease of turbulence towards the surface. This is shown in a more detailed way in Fig. 4.4 giving the phase shift for low frequencies as a function of the Schmidt number exponent. The small deviations are restricted to the range of low n. Since the exponent n for free surfaces varies only between 1/2 and 2/3, it can be determined by the strongly changing phase shift in this range. An accuracy of about 5 % in the phase measurement is necessary in order to determine n with an uncertainty of about 0.03. This method determining the Schmidt number dependence needs only one single tracer.

4.3 Realization of the forced flux method for heat transfer across the aqueous boundary layer

The experimental realization of the forced flux method is determined by two questions: First, how can the flux be controlled? Second, how can the surface concentration be measured?

Both questions find a relatively easy answer for heat transfer across the aqueous boundary layer. First, the forced, periodically changing flux can be realized by a chopped infrared radiator. Second, the surface temperature can be measured by a radiometer.

Even for high wind speeds ($u*_g$ < 0.6 m/s) the thermal layer is thicker than 100 µm. The incoming artificial infrared radiation (2 - 6 µm) is absorbed in a layer of about 20 µm thickness. The radiometer, measuring in the 8 - 14 µm wavelength range, measures the temperature of about the top 10 µm. So in a good approximation both conditions for the measurement are fulfilled: The flux is focused directly onto the surface and the concentration is really measured at the surface.

It is important that the incoming radition is in a wave length region to which the radiometer is not sensitive. This can be achieved by a 1000 K radiator using appropriate filtering for a cutoff beyond 6 µm. On the other hand the IR-radiometer is used with a bandpass filter only transmitting wavelengths above 8 µm.

Results of first measurements

In order to test the new method first experiments have been carried out in the wind-wave facility of the Institut für Hydrologie und Wasserwirtschaft, Universität Karlsruhe in cooperation with E. J. Plate and R. Friedrich. Only very limited instrumentation was available for the test, but it was the only intention of these experiments to verify the capability of the new method.

The IR-radiometer consists of a 1000 W hair-dryer heating element. The radiation is filtered by two films and chopped by a rotating wheel. The footprint of the incoming radiation had a diameter of about 40 cm. The KT-16-T radiometer (Heimann, Wiesbaden) used unfortunately had a response time (90 %) of 1 s only, which is too long for studying the dynamics at higher wind speeds.

A set of experiments was carried out with wind speeds ranging from 2 to 7.5 m/s and with chopper frequencies from 0.05, 0.1, and 0.2 Hz. Sample records of the water surface temperature together with the IR-radiation from the radiator, measured by a simple bolometer are shown in Fig. 4.5 (7.5 m/s wind speed) and Fig. 4.6 (2 m/s). The different response of the water surface at the two wind speeds is clearly visible. At 7.5 m/s the transfer process is so fast that the water surface temperature follows the variation of the IR-radiation without considerable amplitude decrease. On the other hand, a strong decrease in the amplitude with increasing chopper frequency can be seen at 2 m/s.

Figure 4.5: Response of the water surface temperature to a chopped IR-radiation onto the surface for three chopper frequencies at 7 m/s wind speed. The lowest graph shows the signal without radiation. Thin dashed line: IR-radiation; thick line: IR-radiometer signal

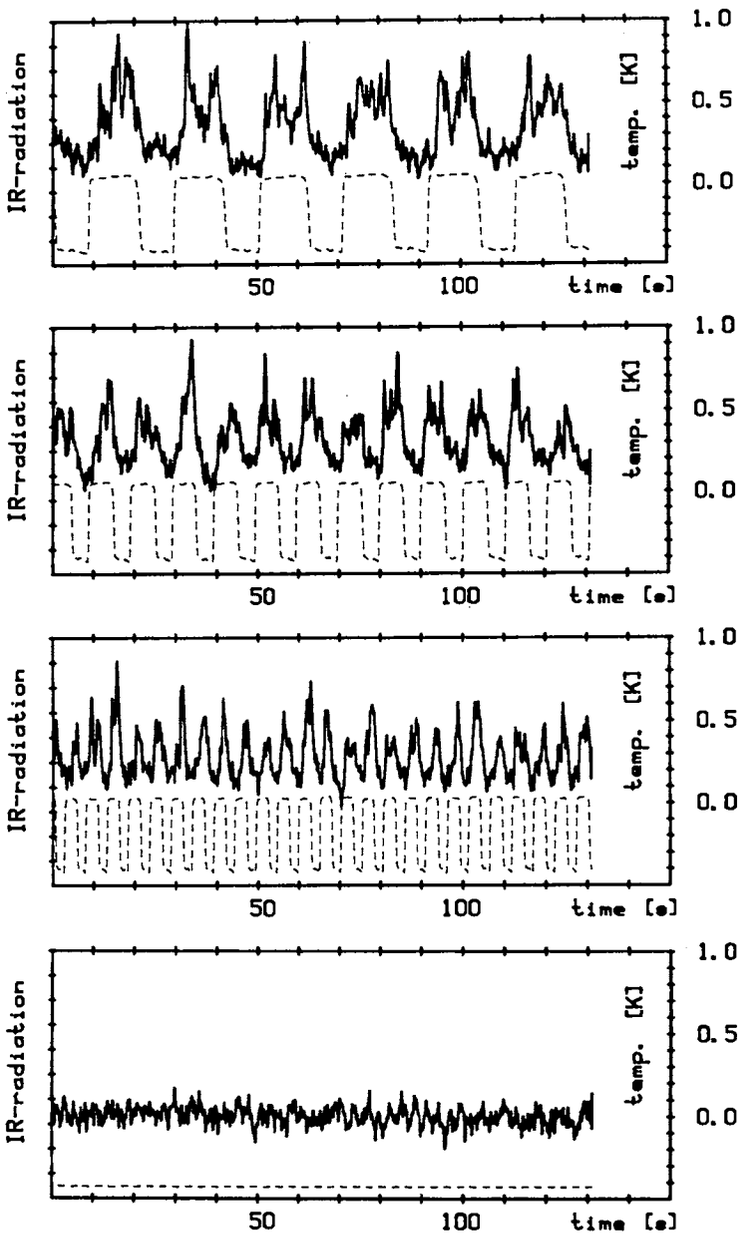

Figure 4.6: Same as Fig. 4.5, but for a wind speed of 2 m/s

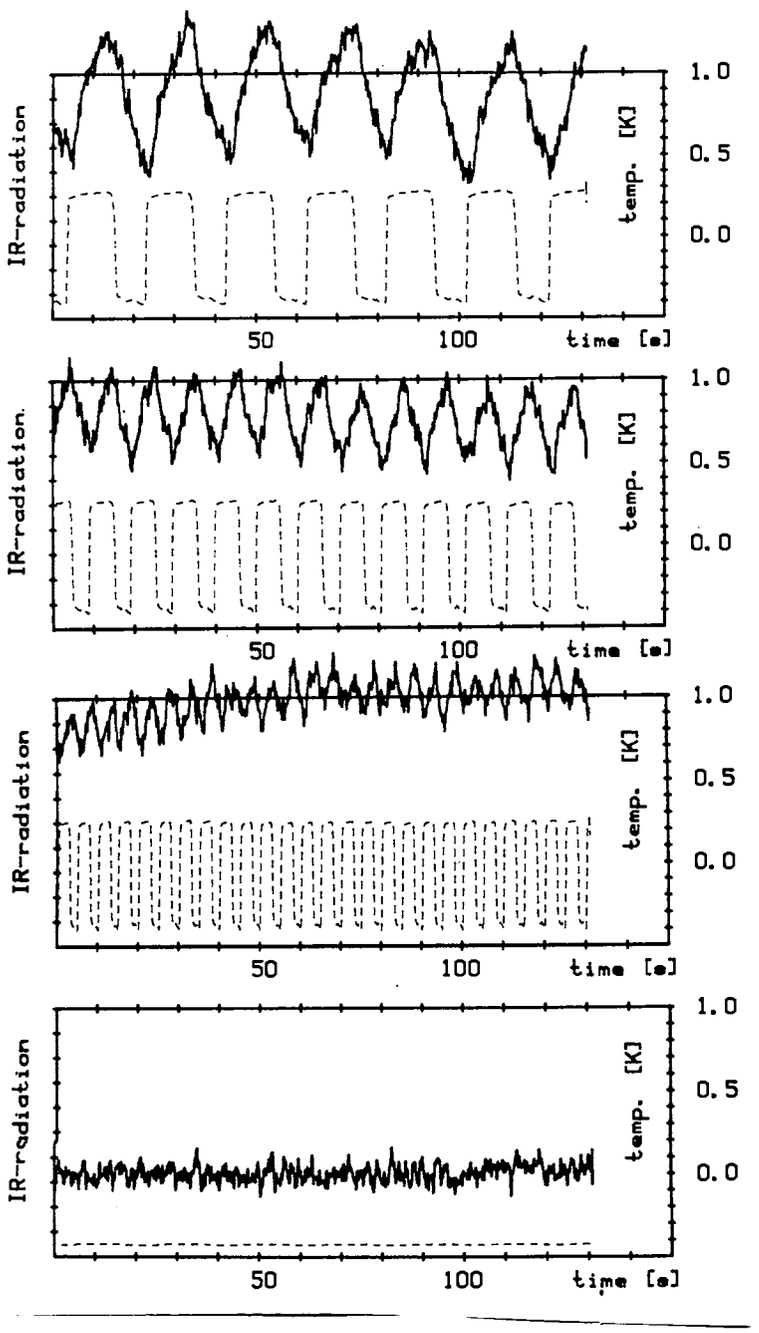

Figure 4.7: Comparison of the measured amplitude damping and phase shift of the water surface temperature with the theoretical predictions. The phase shift (thin) and the amplitude damping (thick) are shown as a function of the dimensionless chopper frequency ω_+. Key to wind speed: * 7.5, + 6, x 5, # 4, and o 2 m/s

Figure 4.8: Heat transfer velocities as calculated from the measured time scale t_* (points with error bars) and oxygen transfer velocities as a function of wind speed (thick *). Thin stars: prediction of the heat transfer velocity from the oxygen transfer velocity on the base of a square root Schmidt number dependence.

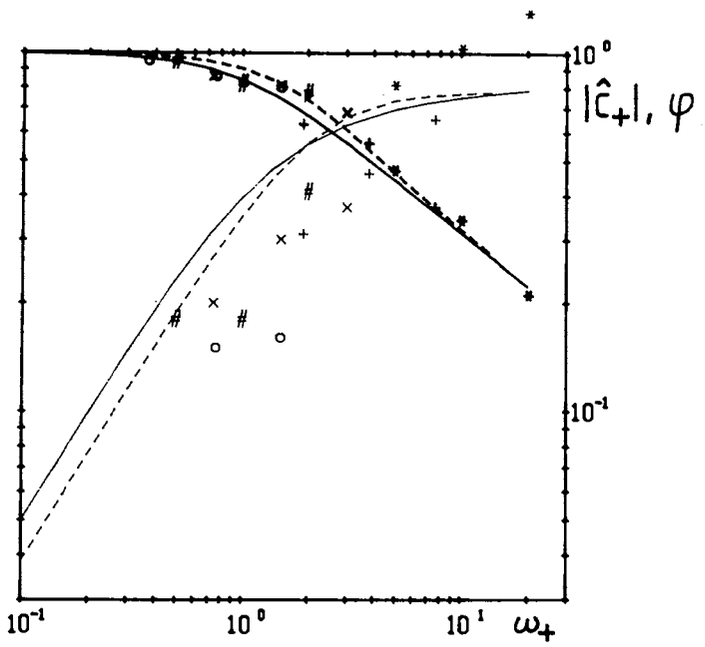

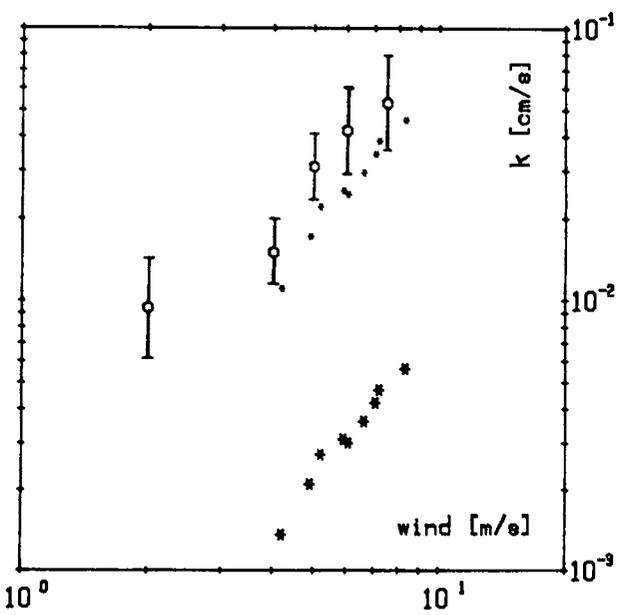

Phase shift and amplitude of the surface temperature amplitude as well as the coherency between the two signals were calculated from the sample records with the same technique as for the determination of the phase speed from two spatially separated sample records of the wave slope signal (see chapter 5.4). The results are shown in Fig. 4.7. The time constant t_* has been determined so that the deviation from the theoretical amplitude damping is minimal. It can be seen that the amplitudes nicely follow the expected decrease at higher frequencies. It is not surprising that the phase shifts are not accurate. Because of the slow response time of the radiometer the corrections were higher than the measured phase.

From the measured time constants transfer velocities have been calculated (Fig 4.8). Within the experimental error they agree with predictions based on oxygen gas transfer measurements in the same facility (Dittrich, private communication).

Conclusion

Despite the very limited instrumentation the measurements clearly verified the capabilities of the new method. So it can be expected that with a faster and less noisy radiometer the new method can be used successfully. It should be emphasized that local transfer velocities are obtained. This avoids the problems of the conventional mass balance technique (chapter 3.1) and makes the technique especially useful for parameterization of the transfer in the field. Furthermore, the fetch dependence of the transfer processes in wind-wave tunnels can be studied easily.

The potential of the method is so promising that a cooperation with the Institut für Hydrologie und Wasserwirtschaft has been set up with the aim to study the combined action of surface and bottom induced turbulence on the transfer processes across the water surface in the laboratory and in the field. This important condition is an ubiquitous phenomenon on the surface of rivers and has hardly been studied yet (Plate and Friedrich, 1984).

5. WAVES AT A FREE SURFACE: A KEY TO NEAR-SURFACE TURBULENCE?

5.1 Failure of recent models for the mass transfer across a free wavy surface

The comparison of the transfer process at a solid wall (chapter 3.3) and across a free wavy interface (chapter 3.4) reveals the basic difference of the two transfer processes:

At a solid wall the transition from smooth to rough surface flow leads (after an increase in the transition region) finally to a continuous decrease of the mass compared to momentum transfer (Fig. 3.9). At a free surface, however, a strong enhancement of mass transfer in comparison to momentum transfer is found with the onset of waves and even at high surface roughness no attenuation of this enhancement can be observed (Fig. 3.10).

This strong enhancement clearly indicates that waves cannot be regarded just as static surface roughness elements for the liquid flow. This concept, being successfully used for rough solid walls, can only be applied to air flow over water, since in this case the wave induced velocities are small compared to air velocities. But this is not true for the liquid phase. So there is no hydrodynamic similarity between the transfer processes at both sides of the gas-liquid interface and the line of models using this similarity for the liquid side (Kondo, 1976; O'Connor, 1983; Kerman, 1984) miss the essential point, though their models may fit the data by adjusting the free parameters.

The asymmetry of the transfer process is illustrated once again in Fig. 5.1 by direct comparison of the air-phase controlled evaporation with the gas transfer velocity as measured in the small circular wind-wave facility.

Figure 5.1: CO_2 gas transfer velocity as a function of the evaporation rate measured in the small circular wind tunnel under the condition as indicated; solid line: theoretical relation for a smooth water surface according to Deacon (1977) (from Jähne, 1980).

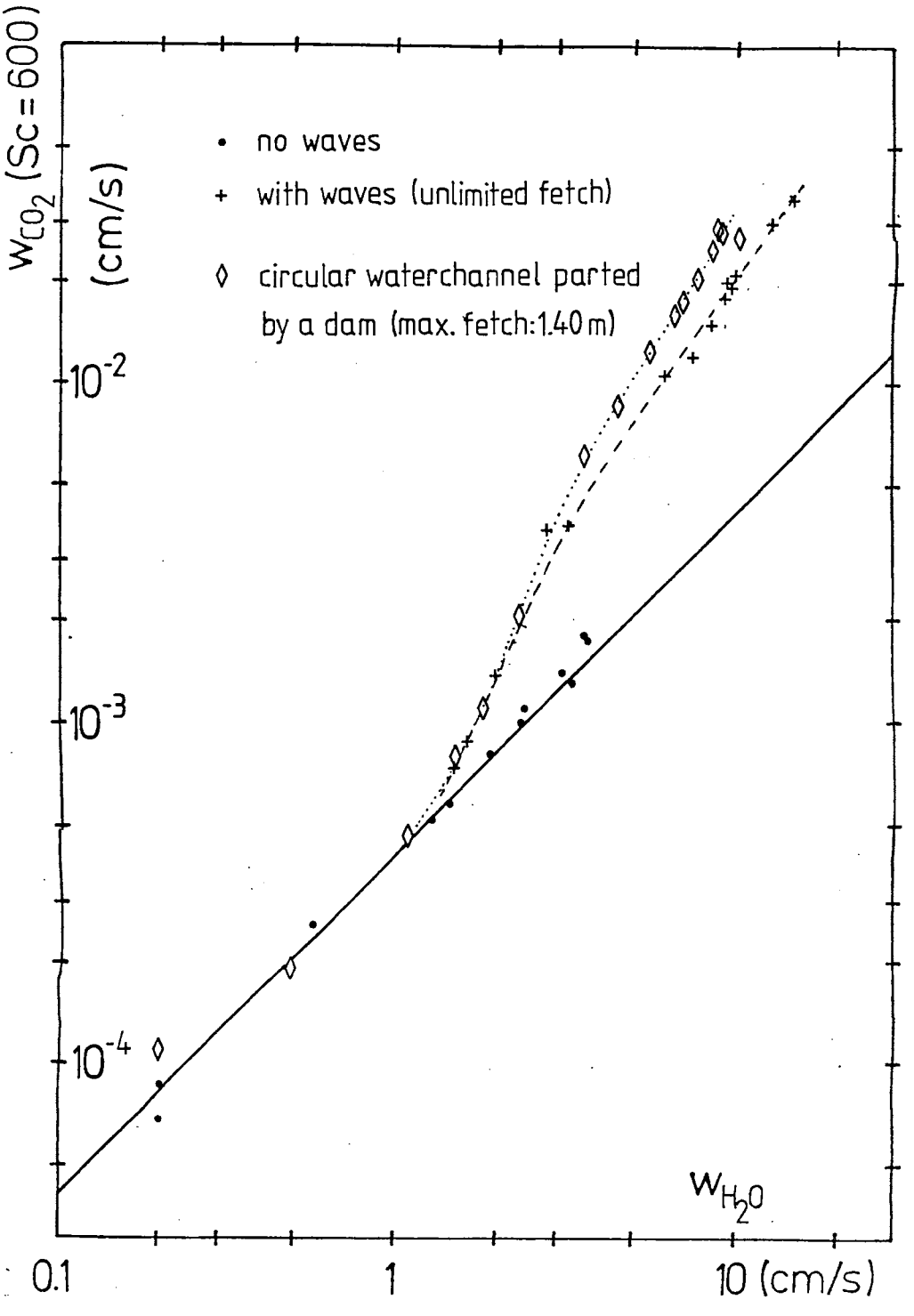

Witting (1971) proposed a "rubber cloth" model in order to explain the enhancement of mass transfer by waves. He assumes only a passive effect of the waves by means of a periodic dilation of the boundary layer, and no active interaction. The transfer rate is increased proportional to the mean square slope of the waves. He found enhancement factors up to 9 for Crapper capillary waves of maximum steepness. But it is obvious that for such high steepness the assumptions of the model are no longer valid. In any case, for the wave slopes obtained in wind tunnels the increase calculated according to his model is much lower than the measured one (Jähne, 1980).

Consequently, the water surface waves must actively take part in the mass transfer process in the liquid. They cannot be regarded just as passive roughness elements or a flow perturbation in the liquid. On the contrary, as indicated by the enhanced mass transfer, a strong additional turbulence source must be associated with them and it is necessary to study the wave dynamics in detail.

Notably, that the increase of the mass transfer starts with the onset of waves at already small wave slopes and not only with wave breaking. It looks as if a transition to another flow regime takes place with the occurance of waves opening an additional degree of freedom of the free surface with no analogue to the processes at a solid wall. This new flow regime is characterized by an interaction of the energy flows determining both the turbulent flow and the additional energy exchange system "waves".

This new free-surface flow regime is a general phenomenon being found with all kinds of a free surface. Waves generated at the surface of a falling film beyond a critical Reynolds number cause a two to three times enhanced mass transfer in comparison to a smooth film (Brauer, 1971). As in wind tunnels the onset of waves critically depends on surface contamination. Surface oscillations of bubbles are the analogue to waves on a free surface. Larger bubbles with surface oscillations also show considerably larger mass transfer velocities than small bubbles with rigid surfaces do (see Schoder, 1984 and Maiß , 1985). The wind-wave tunnel experiments already indicate that the wavy flow regime is not sensitive to the length scale, since it can be found in facilities the size of which varies over two orders of magnitude (chapter 3.4).

5.2 Interaction between the nonlinear wave field and near-surface turbulence

In chapter 2.5 (Fig. 2.2) it is briefly shown that the wave field is determined by the balance of three different energy fluxes:
- the energy input from the turbulent gas flow above the liquid
- nonlinear wave-wave interaction transferring energy between wave components of different wave lengths, and
- the energy loss by decay of the waves to turbulence and by breaking.

All theories discussed in the previous chapter neglect these energy fluxes. Since stress continuity is assumed at the interface only a small fraction of the tangential stress transfers energy to the waves. Moreover, direct turbulence production by waves is neglected.

The dissipation of waves to turbulence being the critical parameter for mass transfer across the surface will be the point of the following discussion. It is not intended and, in fact, not possible to present a full physical picture of the complex interactions.

In a stationary wave field energy input by wind, energy transfer by nonlinear interaction and energy loss must balance on the average for each individual wave number and frequency respectively. Since three fluxes must cancel each other, definitive conclusions from the spectral densities of the wave field can only be drawn, if at least one flux can be neglected or is known. In fetch limited situations, as in linear wind-wave tunnels, the balance is even more complex, because wave energy density changes with fetch. According to Hasselmann (1968) the unsteady energy balance of the wave field in this situation is given by

$$\partial F/\partial t + c_g \partial F/\partial x = J_i + J_{nl} - J_d, \qquad (5.1)$$

where F is the spectral energy density of the wave field, c_g is the group velocity, and J_i, J_{nl}, and J_d are the wind input, nonlinear transfer, and dissipation respectively. Wave growth and wind are along the x-coordinate. The form of (5.1) still assumes the waves to be basically linear, since the nonlinear interaction term only occurs in a net energy exchange term J_{nl} between one wave component and all others. In an homogenous wave field, as in the circular wind-wave facilities,

the energy transport term $c_g \partial F/\partial x$ vanishes, leading to a simpler energy balance. In addition, this balance is closer to natural conditions in the ocean.

The crucial question for the mass transfer problem concerns the source and the scale of the dissipation term. If waves dissipate only by molecular viscosity no turbulence will be generated and the mass transfer process will not be affected by waves. But the viscous dissipation is quite small. According to Phillips (1980), the attenuation rate for a clean water surface is given by

$$\gamma_v/\omega = \frac{1}{\omega} \cdot \frac{\dot{E}}{2E} = \frac{2\nu k^2}{\omega} \tag{5.2}$$

and for a surface covered by a rigid film by

$$\gamma_f/\omega = \frac{1}{2\sqrt{2}} \left(\frac{\nu}{\omega}\right)^{1/2} \cdot k \tag{5.3}$$

Both rates are shown in Fig. 5.2. Attenuation is only important for high frequency capillary waves due to the k^2-dependence. Viscous attenuation determines the ultimate high frequency cut-off of the waves. If viscous dissipation really sets the upper limit for high frequency capillary waves, the cut-off will be temperature dependent. The experiments of Dutzi (1984) (see also chapter 3.5) showed that this is not the case and suggest that small scale turbulence (expressed in a turbulent diffusion coefficient) sets an earlier cut-off.

The instability of steep waves finally leads to wave breaking and air entrainment. It is obvious that this process produces near-surface turbulence. It is a well-known fact, which can easily be observed without any instrumentation in wind tunnels, that waves become instable long before they break with air entrainment. Parasitic capillary waves are generated at the leeward face of the gravity wave both for wind waves and mechanically generated waves (see Fig. 5.9). This generation of capillary waves by steep gravity waves is an example for a strong interaction between waves (Phillips, 1978). This process is called "micro-scale wave breaking". It is important to note that this process starts quite early as soon as some dominant waves have been developed. In fact, Banner and Phillips (1974) showed that the shear flow at the surface is responsible for the destabilization of waves long before they reach their limiting steepness.

Figure 5.2: Attenuation rate of water wave at a clean surface, γ_v/ω, and at a surface covered with a solid film, γ_f/ω. In addition, the dispersion relation is shown (from Phillips, 1980).

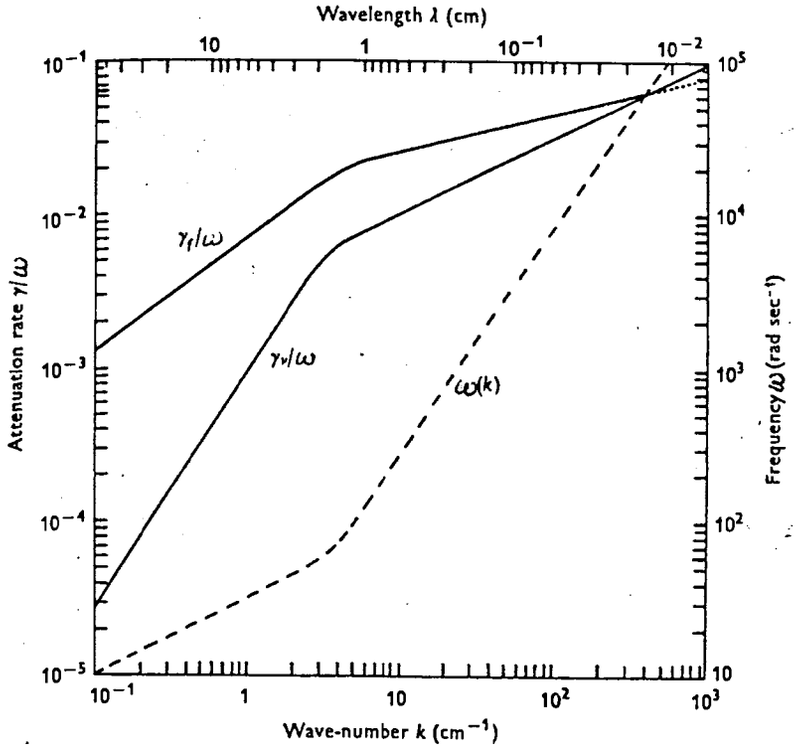

The visualization experiments of Toba et al. (1975) and Okuda et al. (1976) with hydrogen bubbles clearly demonstrate that wind waves are accompanied by forced convection. They found that the waves considerably disturb the shear flow at the surface. The shear flow grows on the windward side of the crest and converges at the lee side to form a downward thrust (with velocities in the order of 10 cm/s at 4 mm depth) associated with small scale turbulence. These results verify the importance of the turbulent processes accompanying the waves most clearly. They emphasize the close link of turbulence and wind waves in the real wave field being far away from the case of a linear superposition of periodic and turbulent motions with perhaps only weak interaction.

Another source of near surface turbulence may be the direct interaction of the shear flow with capillary waves. The orbital motions of high frequent capillary waves (50 - 200 Hz) with wave lengths from 6 to 2.5 mm have only small penetration depths $\lambda/2\pi$ from 1 to 0.4 mm being of the same order of magnitude as the viscous boundary layer thickness. So just from scale considerations it is quite reasonable to assume an interaction between capillary waves and shear flow which may result in both capillary wave damping and near-surface turbulence. Arguments of this kind have been put forward by Hasse and Liss (1980) and by McCready and Hanratty (1984). This topic was discussed in detail on the "Symposium on Capillary Waves and Gas Exchange" (Broecker and Hasse, 1980), but no definitive conclusions have been attained.

Basically, therefore we have two different hypotheses for the enhancement of the liquid-phase mass transfer coefficient. With the latter one, only small scale capillary waves are important and for the former one the large scales are rate controlling, because they contribute the energy for near surface turbulence. In any case, it can be concluded that strong interactions are more essential for the mass transfer problem.

This is an important point, since the wave spectra for gravity waves are scaled by weak interaction. For instance, Kitaigorodskii (1983) assumed that wind energy is mainly put into the dominant waves and that there exists an analogue to the Kolmogoroff inertial subrange in turbulence, where the wave energy is transferred mainly by resonant nonlinear interaction to smaller wave lengths, where it finally dissipates.

The resonant interaction between gravity waves are a very weak coupling process. It involves a set of four components in order to fulfill the resonance conditions for both the wave frequency and the wave vector (Hasselmann, 1962). By dimensional analysis (Kinsman, 1965) the characteristic time scale for the interaction is given by

$$\tau = \langle T \rangle \langle s^2 \rangle^2, \tag{5.4}$$

where $\langle T \rangle$ is a suitably defined mean wave period and $\langle s^2 \rangle$ the mean square slope. With typical mean square slopes the time constant for the interaction will be of the order hundreds of wave cycles.

McGoldrick (1965) considered resonant interaction between capillary-gravity waves. He showed that by the inclusion of surface tension as an additional restoring force resonant interactions already between three wave components are possible. This is basically caused by the dispersion relation for capillary waves ($c^2=k\sigma/\varrho$) leading to a minimum phase velocity of 23.2 cm/s for a 1.73 cm, 13.4 Hz wave on a clean water surface and pairs of waves propagating with the same phase speed. In addition, the interaction is much stronger than between pure gravity wave. The third wave component is excited in less than 5 cycles of the interacting waves.

5.3 Discussion of wave slope spectra

In this chapter we now shall analyse wave spectra in order to get some information on the turbulent dissipation of waves. The discussion is restricted to wave slope spectra, since all waves up to the high frequence cut-off have to be considered which are difficult to measure with conventional wire gauges (Sturm and Sorrell, 1973; Liu et al. 1982).

Optical slope measuring technique

The wave slope is measured with an optical device offering the advantage of avoiding any disturbance of the wave field. The slope gauge used in the experiments (Tschiersch, 1980; Lange et al., 1982; Jähne, 1983a; Jähne et al., 1985) is considerably improved in comparison to former slope gauges (Cox, 1958; Long and Huang, 1976; Hughes et al., 1977; Reece 1978; Shemdin, 1978).

Figure 5.3: Basic optical geometry for measuring wave slopes (a), and a drawing of the submerged optical receiver, used in the large wind-wave facility of the I.M.S.T., Marseille, (b).

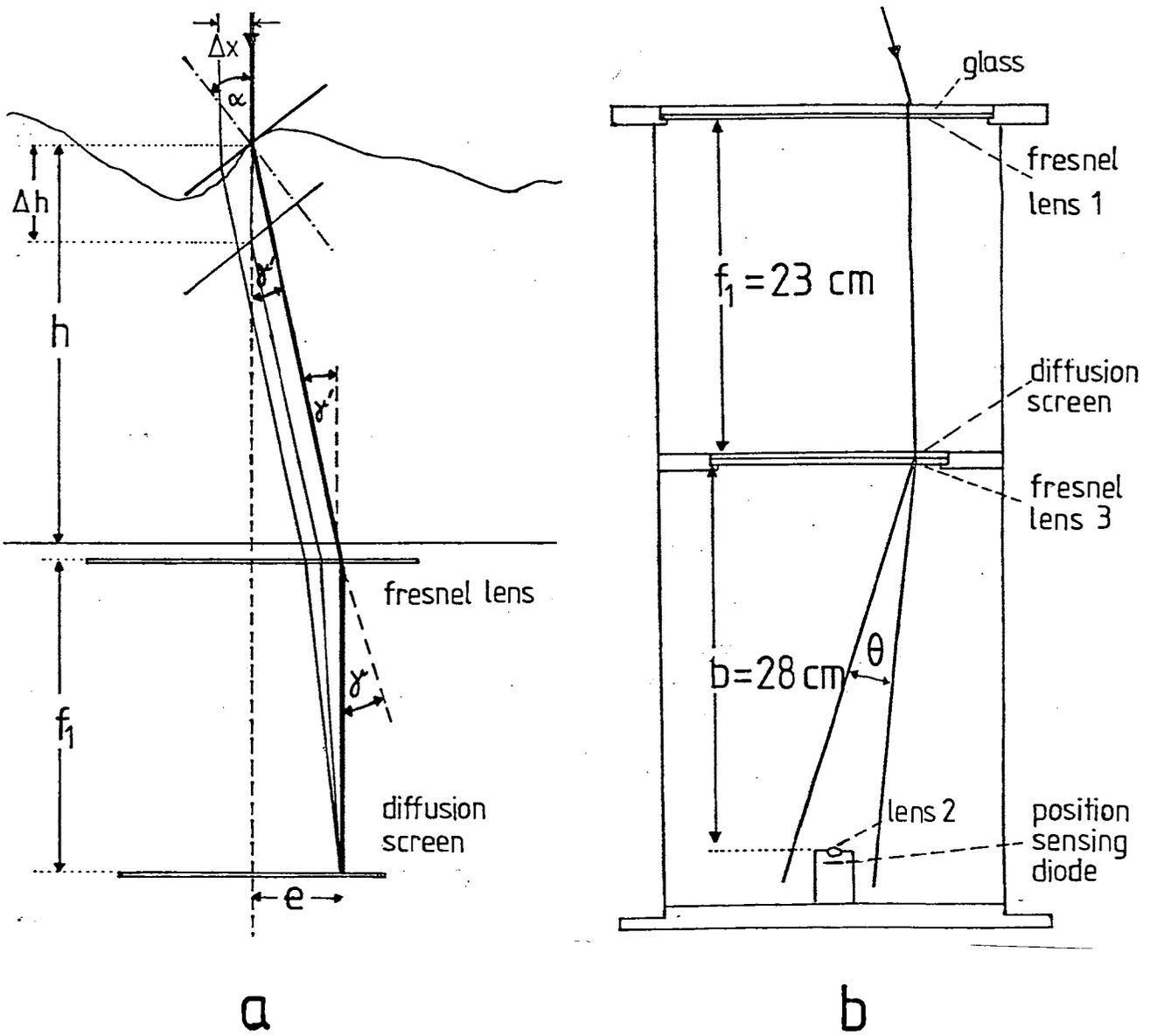

The light beam of a 5 mW He-Ne-laser vertically pierces the water surface from above and is refracted by the sloped water surface (Fig. 5.3). The tilted ray is collected by a Fresnel lens onto a diffusor, one focal length distant from the lens. So the horizontal displacement of the spot on the screen is independent of the wave height, and is only a function of the wave slope. A second lens images the spot onto a dual axis position sensing photodiode. The amplifier circuit enables the x- and y-position signals to be divided by the intensity in order to avoid systematic errors due to intensity variations.

The system has been checked carefully and is capable to measure capillary waves up to the high frequency cut-off without significant damping (Jähne, 1983a).

The slope signal

Let the water surface deflection be represented by a Fourier-Stieltjes integral

$$n(\underline{x},t) = \iint n(\omega,\underline{k}) \exp[i(\underline{kx}-\omega t)] \, d\underline{k}d\omega, \tag{5.5}$$

where $n(\omega,\underline{k})$ is the complex valued amplitude function. Since the slope is the spatial derivative of the deflection, the slope signal is given by

$$\underline{s}(\underline{x},t) = \nabla_2 \, n(\underline{x},t) = \iint i\underline{k} \, n(\omega,\underline{k}) \exp[i(\underline{kx}-\omega t)] \, d\underline{k}d\omega. \tag{5.6}$$

The slope is a vector with a component along-wind, s_1, and cross-wind, s_2. Consequently, the corresponding slope power spectra S_1 and S_2 are

$$S_1 = |s_1(\omega,\underline{k})|^2 = k^2\cos^2\theta \; |n(\omega,\underline{k})|^2 = k^2\cos^2\theta \; F(\omega,\underline{k}) \tag{5.7}$$

and

$$S_2 = |s_2(\omega,\underline{k})|^2 = k^2\sin^2\theta \; |n(\omega,\underline{k})|^2 = k^2\sin^2\theta \; F(\omega,\underline{k}),$$

where $F(\omega,k)$ is the directional wave number frequency spectrum and θ the angle between wind direction and the wave propagation.

Two basic conclusions can be drawn from these definitions:
Firstly, slope measurements yield information about the wave direction. The propagation angle θ of a single sinusoidal wave is simply given as

$$\theta = \arctan[(S_2/S_1)^{1/2}]. \qquad (5.8)$$

Secondly, the spectral amplitudes for the wave slope are multiplied by k^2 compared with the spectral amplitudes for the wave height. Phillips (1980) shows, that both gravity and capillary slope spectra, in a saturation range, should follow a f^{-1} frequency dependence. (The corresponding power laws for the amplitude are f^{-5} and $f^{-7/3}$ respectively.) The f^{-1} dependence means that all waves range up to a constant maximum slope in a logarithmic interval dlnf=df/f (if $dS/df = af^{-1}$, then dS/dlnf = a). So the dynamics of the slope signal is much lower than for the height signal.

For gravity waves, of course, the slope spectrum does not represent the wave energy density, given by

$$E_g = g\, F(\omega,\underline{k}) = g\, S(\omega,\underline{k})/k^2. \qquad (5.9)$$

But in the capillary region, the slope spectrum is proportional to the capillary wave energy

$$E_c = \sigma/\rho\, F(\omega,\underline{k})\, k^2 = \sigma/\rho\, S(\omega,\underline{k}), \qquad (5.10)$$

where σ is the surface tension. Point measurements allow the determination of frequency spectra only. With the usual assumption that the angular spread function can be taken into account by a separable spread function $K(\theta)$, the frequency spectra are given by

$$F(\omega) = \int F(\omega,k) \mid K(\theta)\, d\theta\, dk, \qquad (5.11)$$

$$S_1(\omega) = \int k^2\, F(\omega,k) \mid \cos^2\theta\, K(\theta)\, d\theta\, dk, \text{ and}$$

$$S_2(\omega) = \int k^2\, F(\omega,k) \mid \sin^2\theta\, K(\theta)\, d\theta\, dk.$$

These basic integrals are the starting point for all further calculations. An often used angular spread function is

$$K(\theta) = \frac{\Gamma(r/2+1)}{\Gamma(1/2+1/2)\sqrt{\pi}} \cos^r\theta, \quad |\theta| < \pi/2, \; r >= 0. \qquad (5.12)$$

Determination of angular spread from the slope spectra

Equations (5.11) allow the calculation of the cross-/along-wind slope ratio as a function of the angular spread function $K(\theta)$

$$S_2(\omega)/S_1(\omega) = \int \sin^2\theta\, K(\theta)\, d\theta \,/ \int \cos^2\theta\, K(\theta)\, d\theta. \qquad (5.13)$$

From this equation it is obvious that for an arbitrary spread function in the limit of small angular spread the cross-/down-wind ratio is just equal to the variance of the angle

$$S_2(\omega)/S_1(\omega) = \int \theta^2\, K(\theta)\, d\theta = \langle\theta^2\rangle \quad \text{for } \langle\theta^2\rangle \ll 1, \qquad (5.14)$$

correct to the second order (for a Gaußian distribution even to the third order). The brackets $\langle\ \rangle$ are an abbreviation for taking the mean by the integral. For the cosine-type spread function (5.12) the integral results in products of the gamma function, finally reducing to

$$S_2/S_1 = 1 / (1+r) \quad \text{or} \quad r = S_1/S_2 - 1. \qquad (5.14a)$$

So the ratio of the cross-/down-wind slope is directly related to the width of the angular spread. But only a mean information, for small angular spread the mean square variance, can be obtained. It is principally not possible to reconstruct the exact shape of the angular dispersion function. This fact may be illustrated by a simple example:

Such different angular dispersions as a single wave, propagating at an angle of 45°, a bimodal wave structure with two components travelling at $\pm$ 45°, and a homogenous distribution of waves in all directions, they all result in the same slope ratio one. So only unsufficiently structured information is obtained (compare next chapter). Wave slope visualization, therefore, is the appropriate instrument to investigate the angular dispersion of the waves (chapter 5.5).

Figure 5.4: Wave slope spectra (sum of along- and cross-wind component) as obtained in the large wind-wave facility of the I.M.S.T.; wind speeds as indicated; 6 cm/s water drift velocity; key to the fetch: long-dotted line: 2.6 m; short-dotted line: 4.6 m; short-dashed line: 9.4 m; long-dashed line: 21 m; solid line: 30.9 m

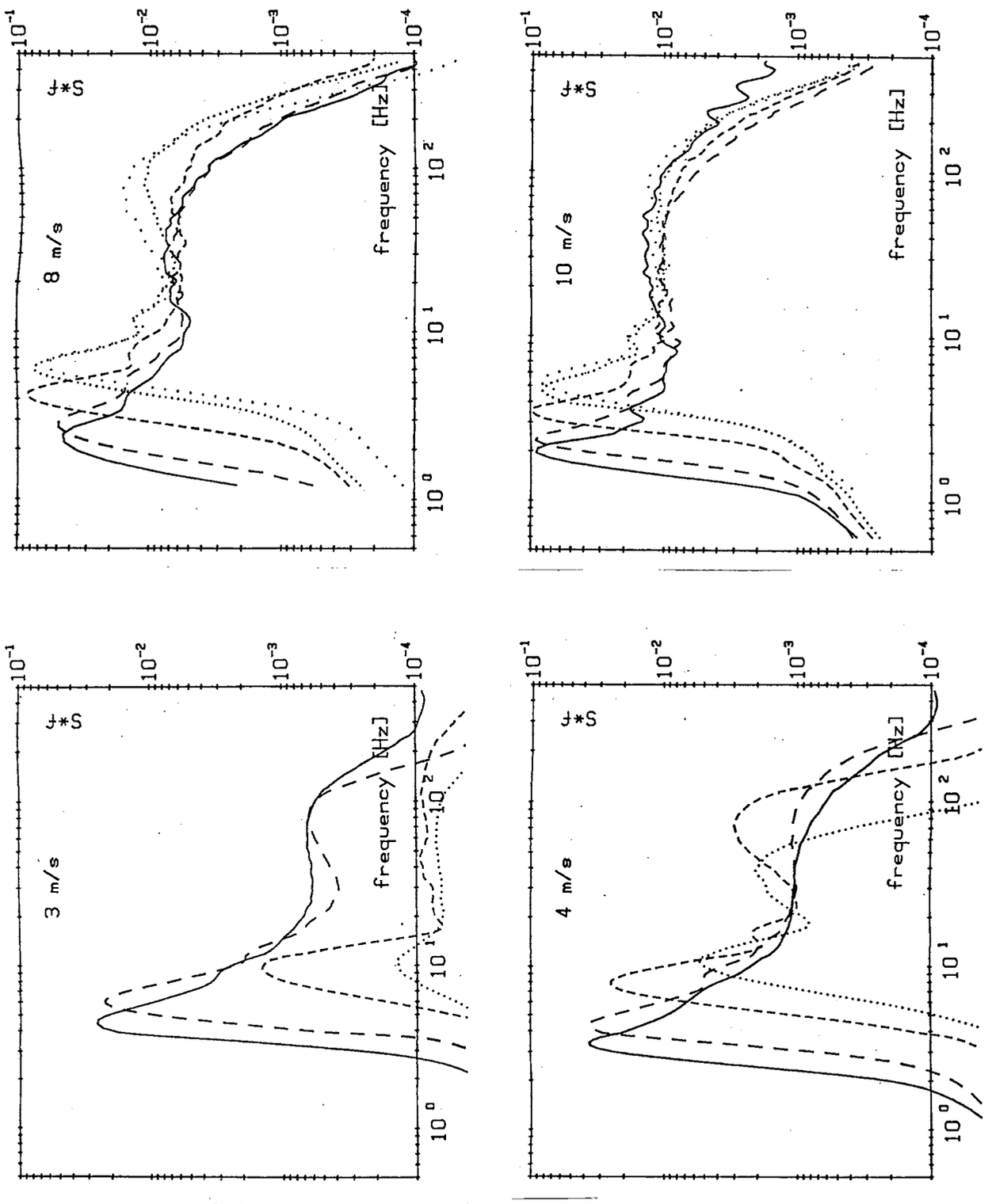

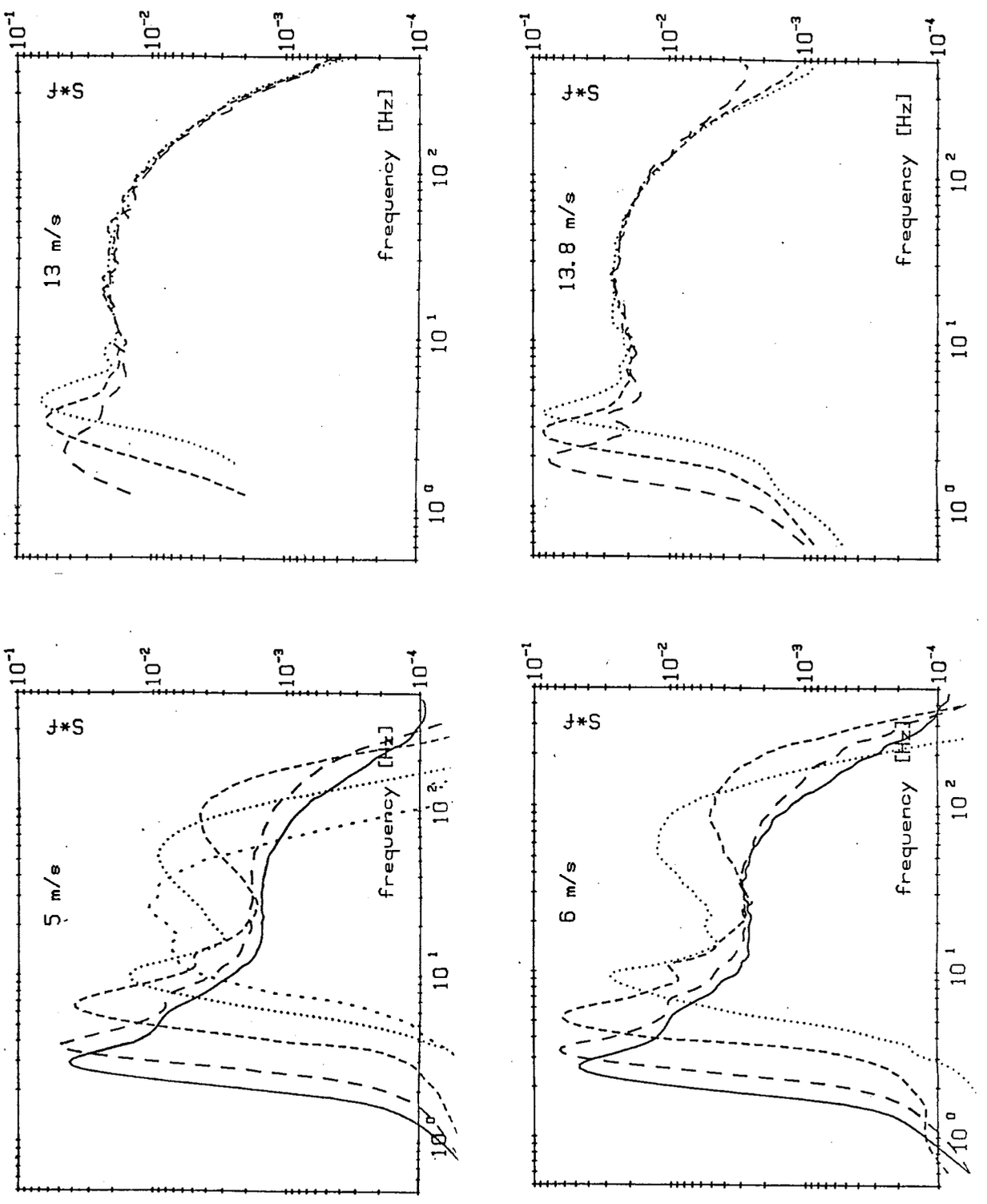
S*f
13 m/s
frequency [Hz]
S*f
13.8 m/s
frequency [Hz]
S*f
5 m/s
frequency [Hz]
S*f
6 m/s
frequency [Hz]

Figure 5.5: Wave slope spectra from the Hamburg and Marseille linear wind-wave tunnels: (a) Hamburg, 15.5 m fetch, with a surface film, wind speeds as indicated; (b) Hamburg, 15.5 m fetch, with a clean water surface; (c) I.M.S.T. large facility, pure wind waves at wind speeds as indicated; (d) I.M.S.T. large facility, 6.5 m/s wind waves superposed by different mechanically generated waves

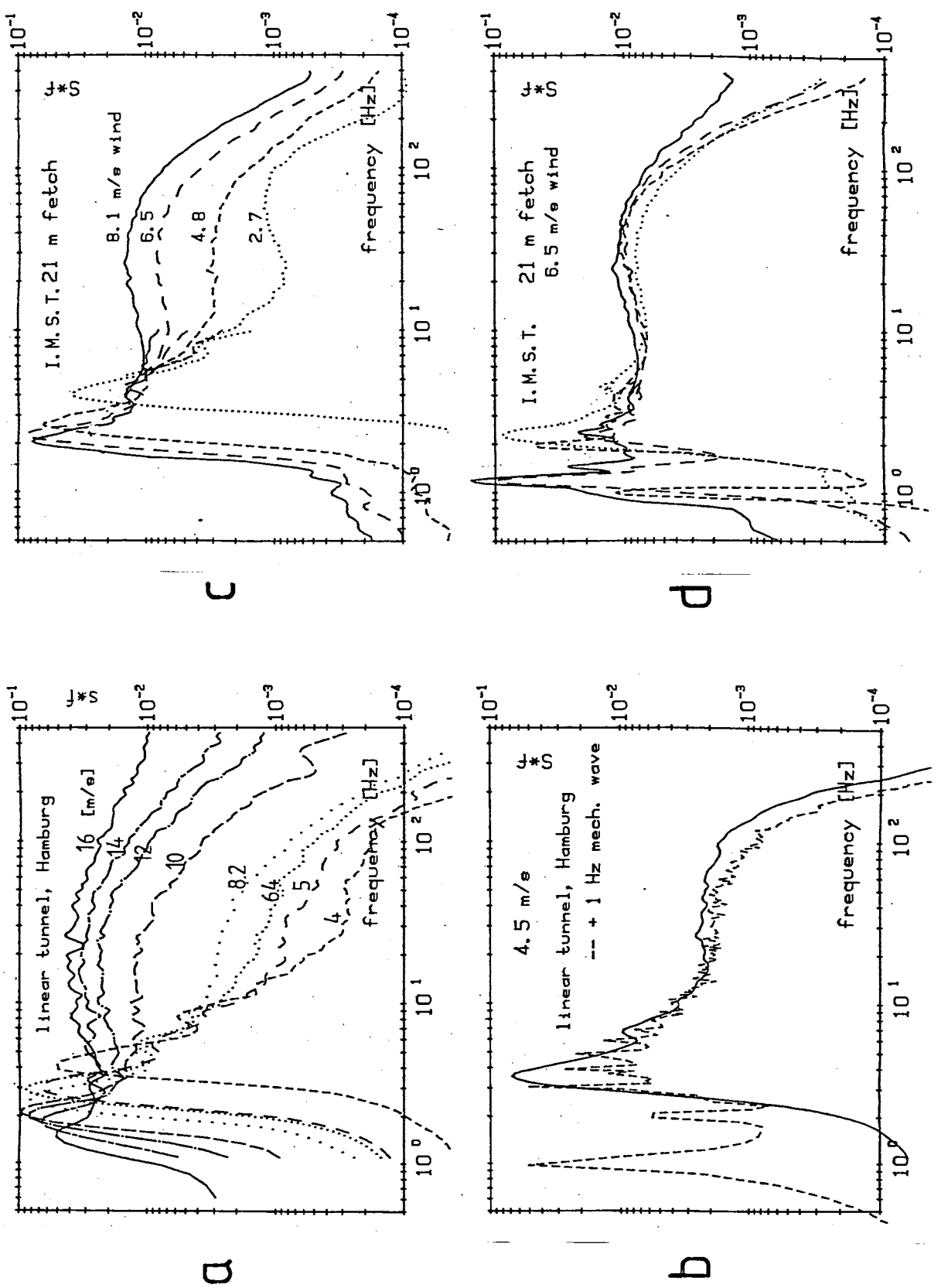

Figure 5.6: Wave slope spectra from the Heidelberg circular wind-wave facilities at wind speeds as indicated; (a) small facility; (b) large facility

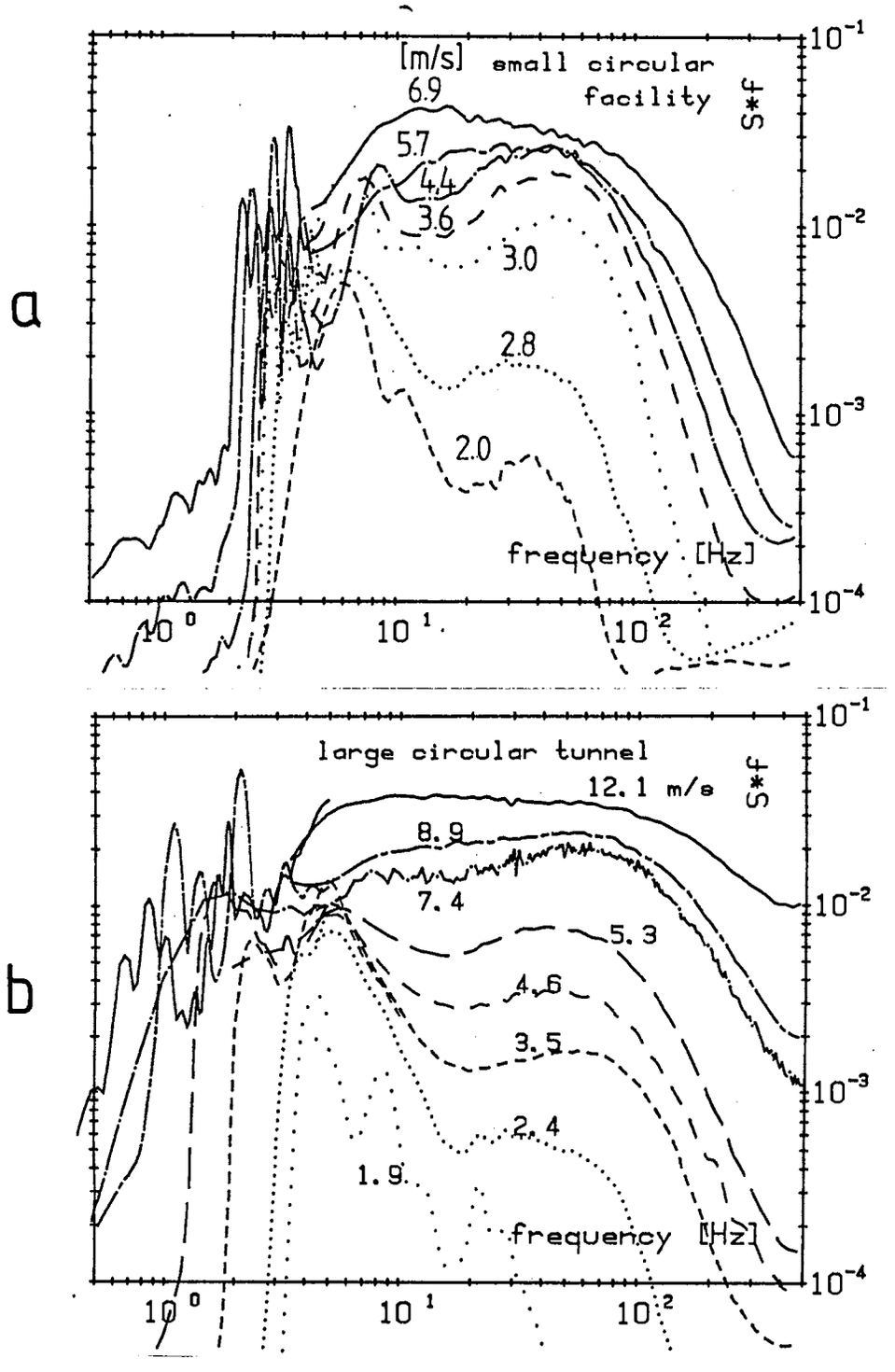

Figure 5.7: Dependence of the capillary wave equilibrium on the friction velocity in different wind tunnels; *: large circular wind-wave facility; o: small circular wind-wave facility; g: large I.M.S.T. facility with 6 cm/s water drift velocity and a slighty surface contaminated water surface; m: same channel, but without a water current and a cleaner surface; h: Hamburg wind-wave tunnel with a surface contaminated water surface; s: same tunnel with a clean surface

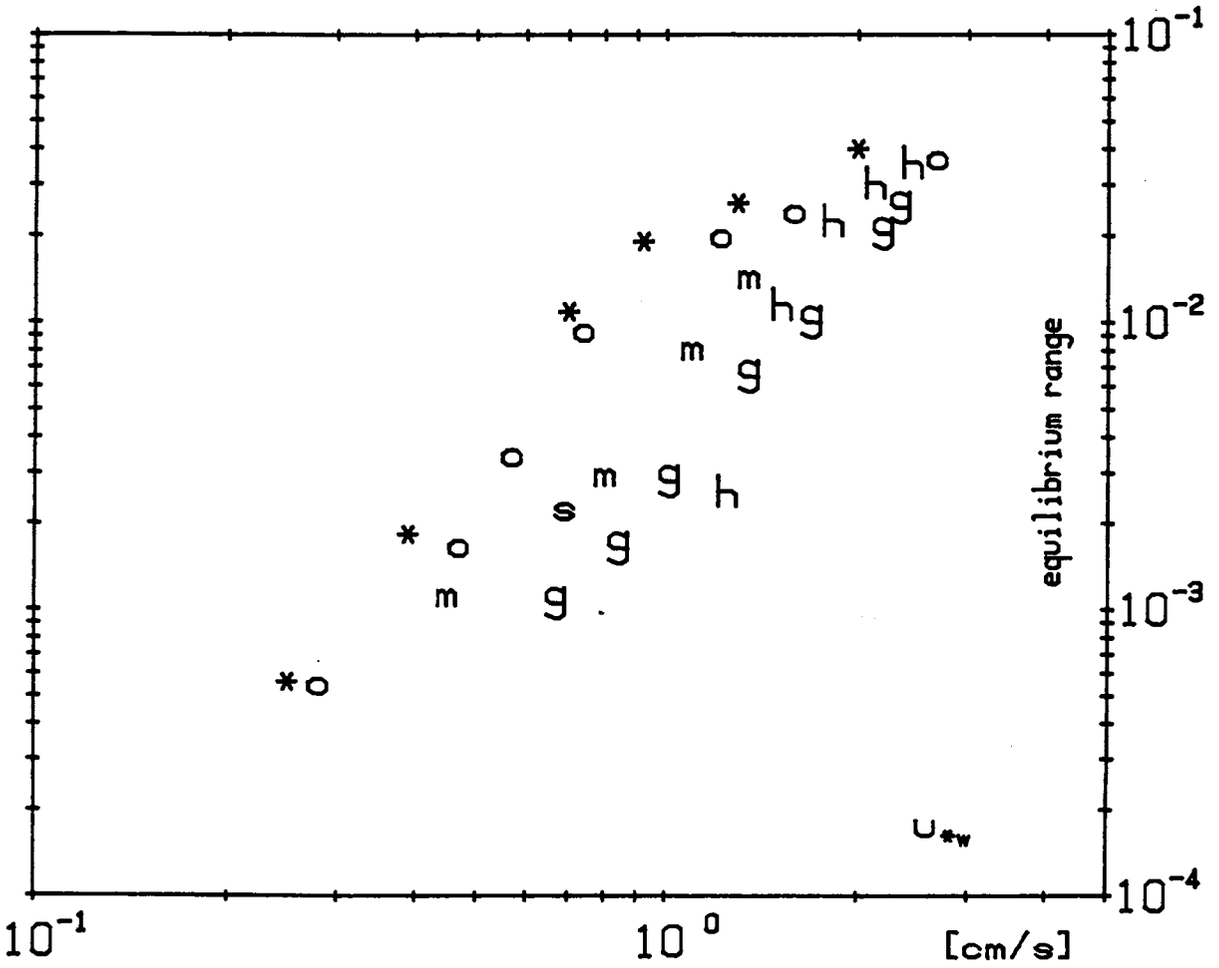

Comparison of wave slope spectra from different wind-wave tunnels

Simultaneously to gas exchange measurements in the two circular facilities and the large I.M.S.T. facility (Jähne et al., 1984a and 1985a) extensive wave slope measurements have been carried out. Additional wave slope spectra are available from yet unpublished measurements in the wind-wave facility of the Sonderforschungsbereich 94, University of Hamburg. The total slope spectra (sum of cross- and along-wind component) shown in Figs. 5.4 to 5.6 are multiplied by the frequency for the sake of a better illustration of the saturation and equilibrium range. The spectra reveal a large number of interesting phenomena, which will not discussed in detail here. We shall focus attention on the information which may be of importance for mass transfer.

Generally, the short fetch spectra of the linear wind-wave tunnels are quite different from the homogenous, fetch-unlimited spectra of the circular facilities. In all spectra of the linear facilities a sharp peak (dominant gravity wave) is found, exceeding the capillary wave slopes by at least one order of magnitude. In the circular facilities, such a peak exists only at lower wind speeds and is less distinct. The sample records (or more simply just a look at the waves) shows that the wave pattern in the circular facilities is much more random: no regular dominant wave is visible like it is in linear wind tunnels.

At lower wind speeds and smaller fetch the secondary bump in the capillary wave region clearly indicates that these waves must predominately be generated by micro-scale wave breaking of the dominant gravity waves. These capillary waves are bound at the lee side of the dominant waves crest. In the circular facilities this effect is less easily visible in the spectra, since there is no distinct dominant wave. At higher wind speeds the capillary wave spectrum becomes flatter. A fetch independent equilibrium range is gradually established. It becomes more extended with increasing wind speed. The level of the equilibrium range strongly depends on the friction velocity and is different for each wind tunnel (Fig. 5.7). But in every tunnel the capillary equilibrium range varies with $u_*^{2.5}$ for smaller friction velocities, gradually decreasing for higher u_* and finally reaching a saturation level being equal for all wind tunnels

$$S(f) = 0.04\ f. \qquad (5.15)$$

The spectra obtained in the Hamburg wind-wave tunnel demonstrate the influence of surface contamination (Fig. 5.5a,b). With a contaminated surface the development of capillary waves first is strongly hindered. But then the capillary waves increase very rapidly and reach the same values as for the clean(er) water surfaces in the other facilities (see also Fig. 5.7). This clearly shows that the wave motions first are strongly hindered by the surface film, but that with increasing turbulent surface stress the waves rapidly overcome the restoring forces of the surface film.

Fig. 5.6b,d also show that mechanically generated waves do not significantly influence the capillary wave slope at higher fetches. This is not surprising, since an equilibrium range has already been established under these conditions.

One may argue that in the circular facilities the waves may strongly be influenced by the curved channel walls and by the centrifugal forces. It can easily be shown, however, that this is not true. Fig. 5.8 shows the temporal growth of the wave spectra, Fig. 5.9 the corresponding sample records in the large circular tunnel. It is evident that the wave spectra pass quite the same structural forms of wave spectra as they are obtained in the linear facilities as a function of fetch (Fig. 5.4). The same overshoot in the capillary wave intensity is found, decreasing gradually again to an equilibrium range. The only marked difference is the lower angular spread of the waves in the circular facility (compare Fig. 5.13 and Fig. 5.14), which may be caused just by the limited width of the annular channel (see Tab. 3.1 and 3.2).

Figure 5.8: Temporal growth of the wave slope spectra in the large circular wind-wave facility at 4.5 m/s wind. The time elapsed in s from the sudden start of the wind is indicated

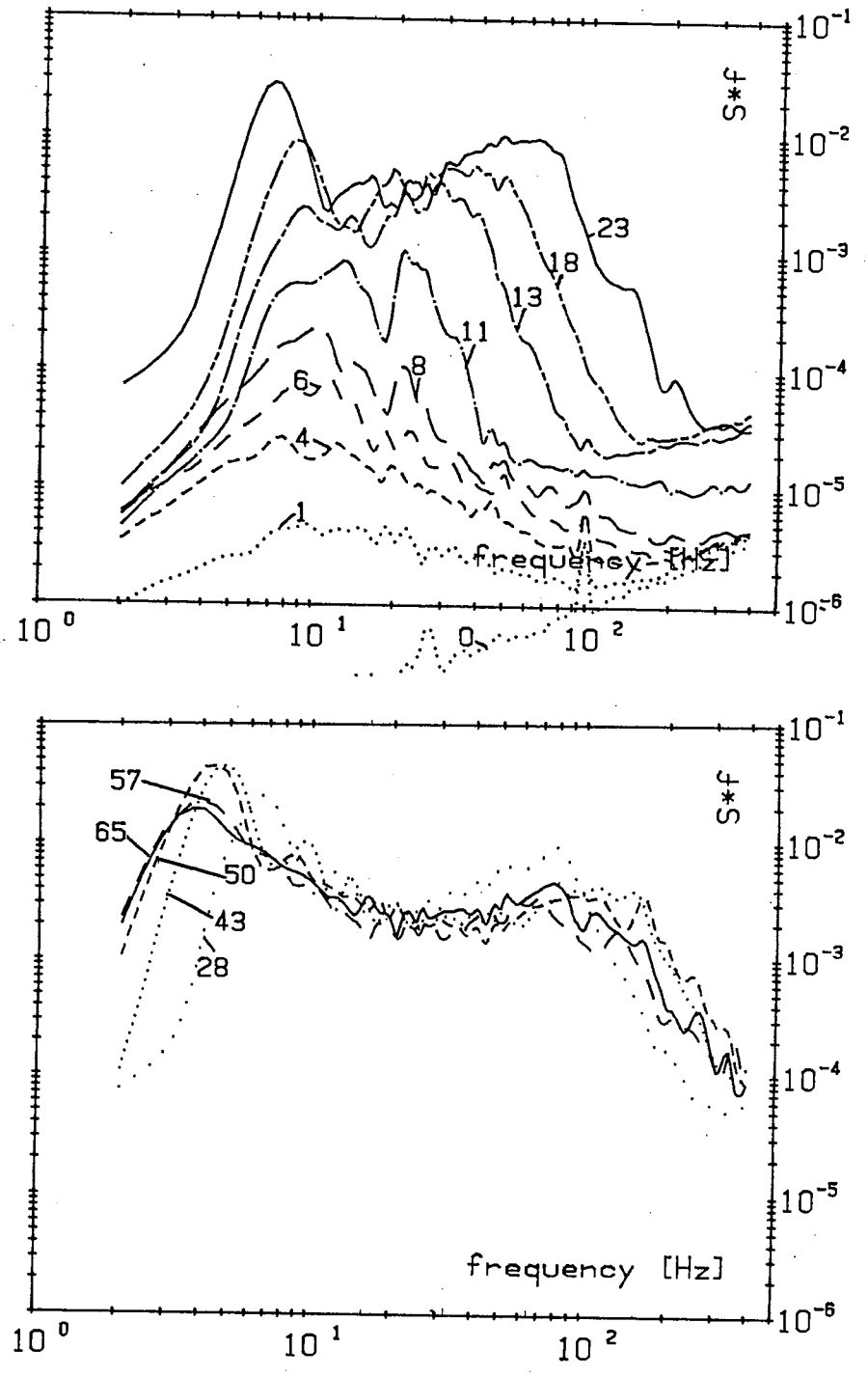

Figure 5.9: Sample records to the spectra of Fig. 5.8. One division on the ordinate is equal to a slope of 0.1. The time elapsed at the beginning of each sample record since the sudden start of the wind is indicated in the figure.

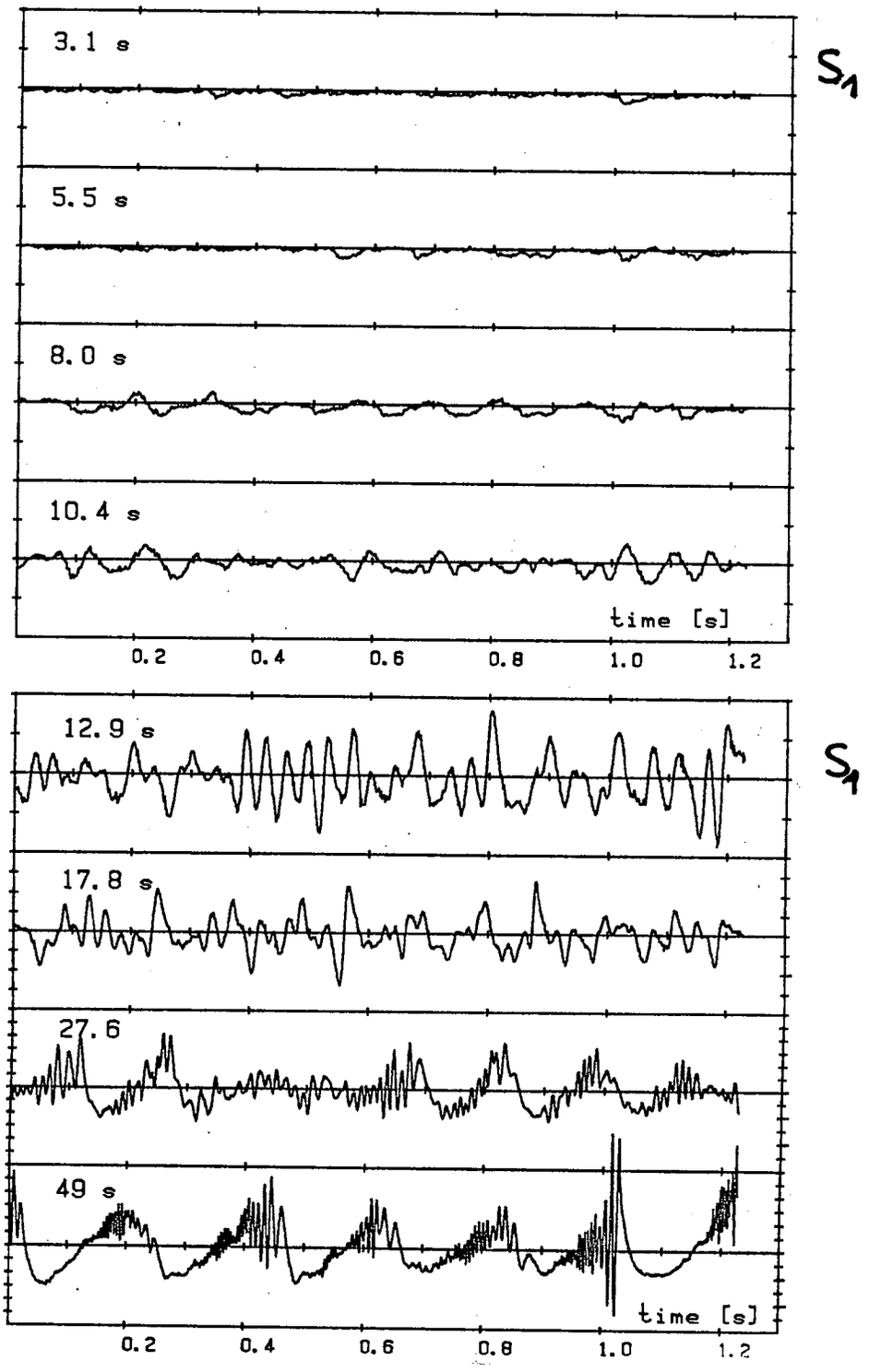

Figure 5.10: Temporal decay of the wave slope spectra in the large wind-wave facility at a sudden stop of the wind (4.5 m/s); time elapsed as indicated

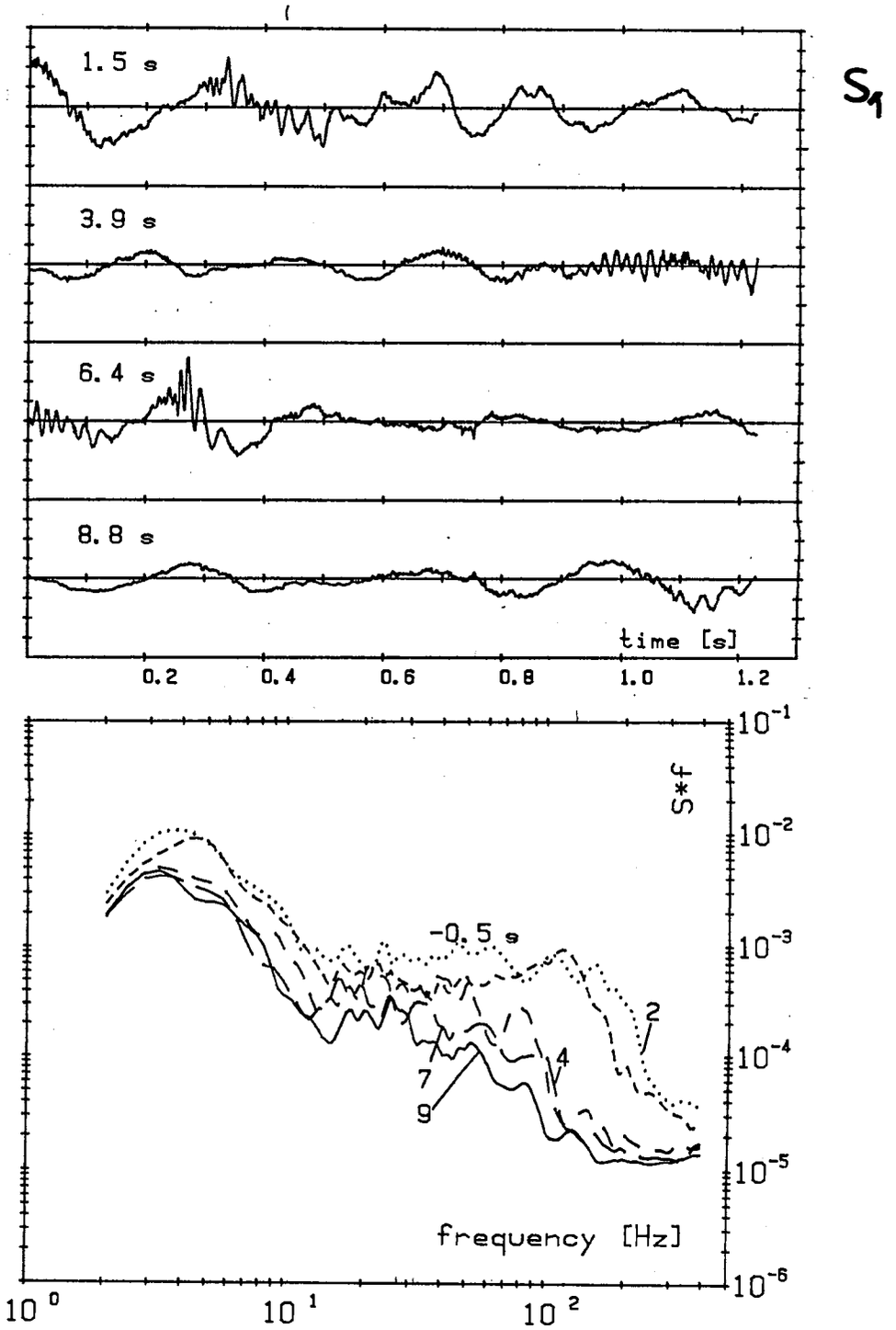

Figure 5.11: Comparison of the mean square slopes in different wind-wave facilities.

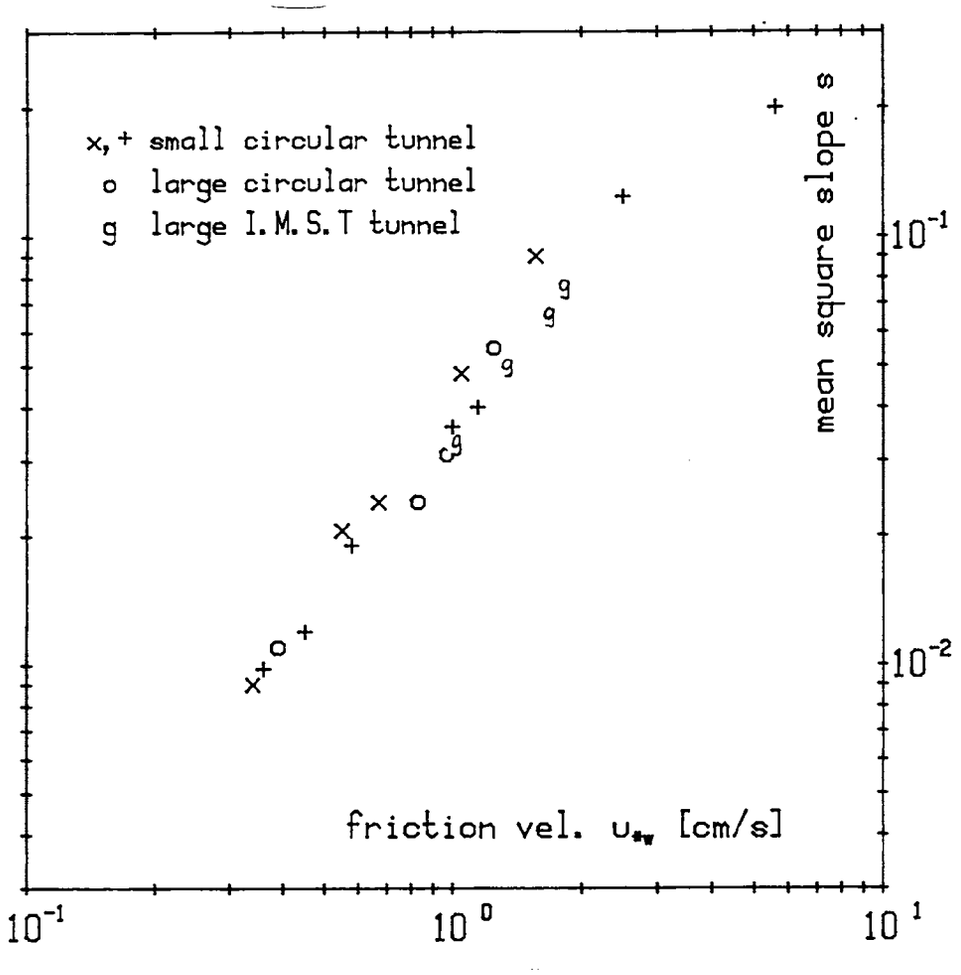

The wave spectra clearly indicate that the high frequency wave component cannot exclusively be responsible for the increase of the mass transfer. The argument is as follows: The gas exchange rates in the large I.M.S.T facility, the small, and the large circular facility agree within 20 % (Fig. 3.10), but the capillary wave equilibrium range in the large I.M.S.T. facility is up to 5 times lower than in the circular facilities (Fig. 5.7). A similar conclusion can be drawn from the integrated capillary wave slope ($f > 13$ Hz) (Jähne et al., 1984a).

This conclusion agrees well with the results discussed earlier in chapter 3.6 and 4.1. Now the question arises, which wave parameter can be used instead for the parametrization of the mass transfer. It is the basic fact that though the wave spectra are quite different (mainly concerning the dominant waves) the gas exchange rate are equal. So we have to look for a wave parameter which does not change either. This is simply the total mean square slope of the waves which proves to be fetch independent beyond the initial wave generation phase and is nearly the same in all three wind tunnels (Fig. 5.11). Clearly, this is only a first approximation. But the mean square slope seems to be a reasonable parameter for the integral near-surface turbulence, since it is a direct indicator of the wave stability.

5.4 Phase speed and coherence of the wave field

The phase velocity and the coherence of the waves are additional parameters to gain further insight into the complex wave propagation on the water surface and its interaction with near-surface turbulence and with shear flow.

The phase velocity is affected by the following mechanisms:
First, the drift velocity of the surface layer increases the phase velocity component in the direction of the water current. This increase will vary with the wave length due to the wave length dependent penetration depth of the wave motion.
Second, the phase speed is a function of the amplitude for steep nonlinear waves.
Third, the wave field may consist of dispersive and non-dispersive components.

Fourth, the phase speed of the small capillary-gravity waves is modulated by the orbital velocity of the dominant gravity wave.

Consequently, for one frequency a complete range of phase speeds will exist, but only a mean phase speed will be obtained. The most critical problem in the phase speed determination with cross-correlation analysis of sample records from wire gauges is the angular dispersion of the waves. This effect makes it very difficult to analyse the measured phase velocities and has lead to controversial discussions in the literature (Ramamonjiarisoa and Mollo-Christensen, 1979; Huang, 1981; Komen, 1980; Phillips, 1981; Dudis, 1981). Slope measurements offer new possibilities, since the width of the angular dispersion is measured directly.

Principle of the cross-spectral method

The determination of the phase speed from two sample records, $\underline{r}$ distant, is based on the fact that the spectral components of the records differ in phase. For a single wave component the phase difference $\varphi(\omega)$ is inversely proportional to the phase speed according to

$$\varphi(\omega) = \underline{kr} = kr\cos\alpha \quad \text{and} \quad c = \omega r\cos\alpha \,/\, \varphi(\omega), \tag{5.16}$$

where α is the angle between the wave propagation and the correlation direction. In a real wind wave field, waves of different directions and different wave numbers will contribute to a single wave frequency. Consequently, the phase function will be a complex integral, which is calculated from the cross-spectrum R, defined as

$$R(\underline{r},\omega) = \int n_{\underline{x}}^{*}(\omega,\underline{k})\; n_{\underline{x}+\underline{r}}(\omega,\underline{k})\; d\underline{k} = \int F(\omega,\underline{k})\, e^{ikr\cos\alpha} d\underline{k} \tag{5.17}$$

The indices $\underline{x}$ and $\underline{x}+\underline{r}$ denote the measuring positions. The phase function is then given as the arctan of the imaginary part (quadrature spectra Q) and the real part (cospectra C) of the cross-spectrum with (5.11)

$$\varphi_i(\omega) = \arctan \frac{\int w_i K(\theta) \int \sin[kr\cos(\alpha)]\, F(k,\omega)\, dk\, d\theta}{\int w_i K(\theta) \int \cos[kr\cos(\alpha)]\, F(k,\omega)\, dk\, d\theta} \tag{5.18}$$

where i denotes the three kinds of signals, the height n, along-wind

slope s_1, and cross-wind slope s_2; w_i are weighting factors for the different signals

$$w_n = 1,\ w_{s1} = \cos^2\theta, \text{ and } w_{s2} = \sin^2\theta.$$

The complicated integrals in (5.18) collapse in the limit of small spatial separation ($kr \ll 1$) to a simple formula. Correlation in wind direction ($\alpha = \theta$) yields

$$\varphi_i(\omega) = f_i\, r\, \langle k \rangle \tag{5.19}$$

with

$$f_n = \langle\cos\theta\rangle,\ f_{s1} = \langle\cos^3\theta\rangle/\langle\cos\theta\rangle, \text{ and}$$
$$f_{s2} = \langle\cos\theta\sin^2\theta\rangle/\langle\sin^2\theta\rangle.$$

The factors $f_i < 1$ take into account the effect of the angular dispersion. The brackets $\langle\rangle$ denote the mean value calculated with the appropriate dispersion function, i.e.

$$\langle k \rangle = \int F(\omega,k)\,dk \quad \text{and} \quad \langle f(\theta) \rangle = \int f(\theta)\, K(\theta)\, d\theta. \tag{5.20}$$

The phase velocity is then given by

$$c_i = \omega\, r\, f_i\, /\varphi_i(\omega). \tag{5.21}$$

A high order Taylor expansion in $kr\cos\theta$ and θ reveals that the simple formulas (5.19) respectively (5.21) are valid for surprisingly high kr, even higher than 2π, i.e. phase shifts larger than 2π, if the angular dispersion is not too wide (Jähne, 1985). This result clearly indicates that the phase speed can be determined accurately also with large spatial separation. The correction factors f_i are much larger for the cross-wind slope signal than for the along-wind component. For a given angular dispersion function they can directly be related to the cross-/along-wind slope ratio. This is an important result, since the correction factors can be derived directly from the slope signal. Only the form of the angular dispersion function can be chosen.

The coherency

A decrease in the coherency of a single frequency wave component is found, when the phase shift between the two measuring positions is fluctuating. This can be caused by three effects:

First, the angular dispersion of the wave field affects the phase shift. A wave, propagating with the same phase speed, but in a different direction, shows different phase shifts according to (5.16). For a wave field with a homogeneous angular dispersion (waves propagation forward and backward) the coherency decreases to zero, since the mean phase shift is zero.
Second, also the wave-number spread causes a decrease in the coherence. Different wave vectors for a single wave frequency may be caused by effects, discussed at the beginning of the chapter.
Finally, for larger correlation distances kr, nonlinear interaction in the wave field decreases the coherency of a wave frequency component.

The first two effects can be calculated quite similar to the effects on the phase speed. The coherency Ch is defined as

$$Ch^2(\omega) = [C^2(\omega) + Q^2(\omega)] \;/\; F^2(\omega) \tag{5.22}$$

With (5.11) and (5.17) the calculations yield for small kr (Jähne, 1985)

$$Ch^2 = 1 - \langle k\rangle^2 r^2 \,(a_i + b_i \langle k^2\rangle r^2). \tag{5.23}$$

The factors a_i and b_i depend on the correlation direction relative to the wind direction and the signal (n, s_1, or s_2). For a correlation along-wind they are given by

$$\begin{aligned} b_n &= \langle\cos^2\theta\rangle \\ b_{s1} &= \langle\cos^4\theta\rangle \;/\; \langle\cos^2\theta\rangle \qquad a_i = b_i - f_i^2 \\ b_{s2} &= \langle\cos^2\theta\,\sin^2\theta\rangle \;/\; \langle\sin^2\theta\rangle \end{aligned} \tag{5.24}$$

and for cross-wind correlation

$$\begin{aligned} b_n &= a_n = \langle\sin^2\theta\rangle \\ b_{s1} &= a_{s1} = \langle\sin^2\theta\,\cos^2\theta\rangle \;/\; \langle\cos^2\theta\rangle \\ b_{s2} &= a_{s2} = \langle\sin^4\theta\rangle \;/\; \langle\sin^2\theta\rangle. \end{aligned} \tag{5.25}$$

Consequently, the influence of the k-spread (the $\langle\Delta k^2\rangle$-term) is more pronounced in the along-wind coherency than in in cross-wind coherency, because of the compensation effect in the factor a_i for along-wind correlation. For a more detailed discussion see Jähne (1985). Here it

is only pointed out that a comparison of cross- and along-wind coherencies may be an appropriate instrument to determine the k- and angular spread effects.

Discussion of measurements

Phase speed and coherency measurements have been carried out with a chopped two-beam laser slope gauge with a distance ranging from 0.91 to 4.74 mm. The system allows simultaneous measurement of two sample records by the same optical receiver resulting in excellently matched signals at both measuring positions (Jähne, 1985).

Both short fetch (4 m in the large I.M.S.T. wind-wave facility) and large fetch wind waves (in the large circular Heidelberg facility) have been investigated. The phase velocities determinated from both the along-wind and cross-wind slope are corrected for angular dispersion as outlined above assuming a cosine-type angular spread function (5.12).

Figure 5.12: Phase velocities, coherency, and wave slope spectra as obtained at 4 and 10 m/s wind in the large I.M.S.T. facility at 4 m fetch: Keys to line types: coherency: solid line: measured value; dashed line: calculated from the angular dispersion as obtained from the slope spectra; phase speed: thin lines: uncorrected values; thick lines: corrected for the effect of angular dispersion; solid lines: calculated from along-wind slope; dashed lines: calculated from cross-wind slope; correlation distance 2.12 mm in wind direction; the theoretical phase speed for linaer waves withot an additional water drift velocity is also shown.

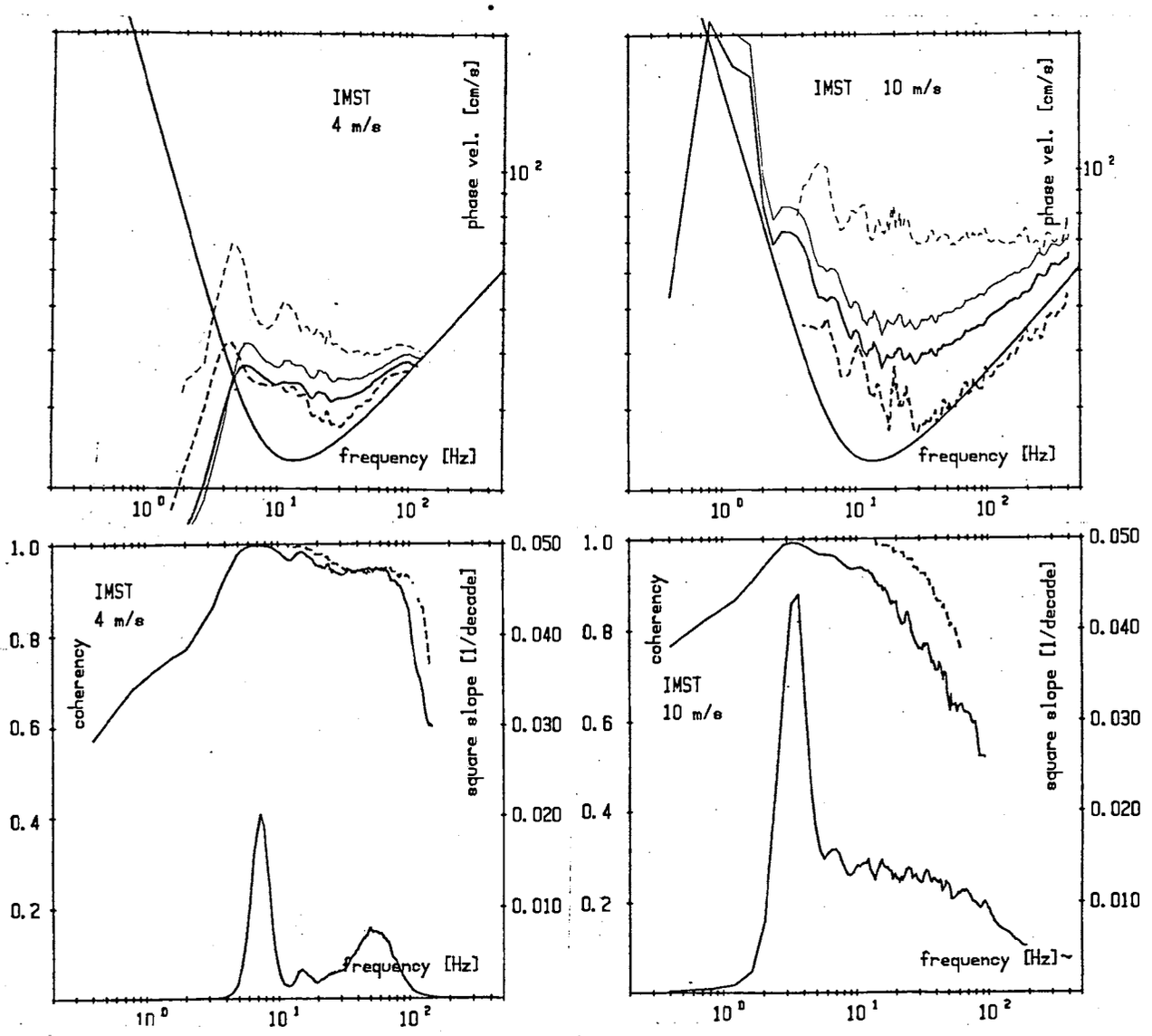

Figure 5.13: Phase velocities, coherency, and slope spectra as measured in the large circular wind-wave facility; correlation distance 2.12 mm in wind direction; different line types mark the wind speed as indicated; phase speed: thin lines: corrected values as calculated from the cross-wind slope; thick lines: dto. from the along-wind slope; coherency: thick lines: measured values; thin lines: calculated from the measured angular dispersion; dotted lines: 2.7 m/s; dashed lines: 4.5 m/s; solid lines 6.4 m/s wind

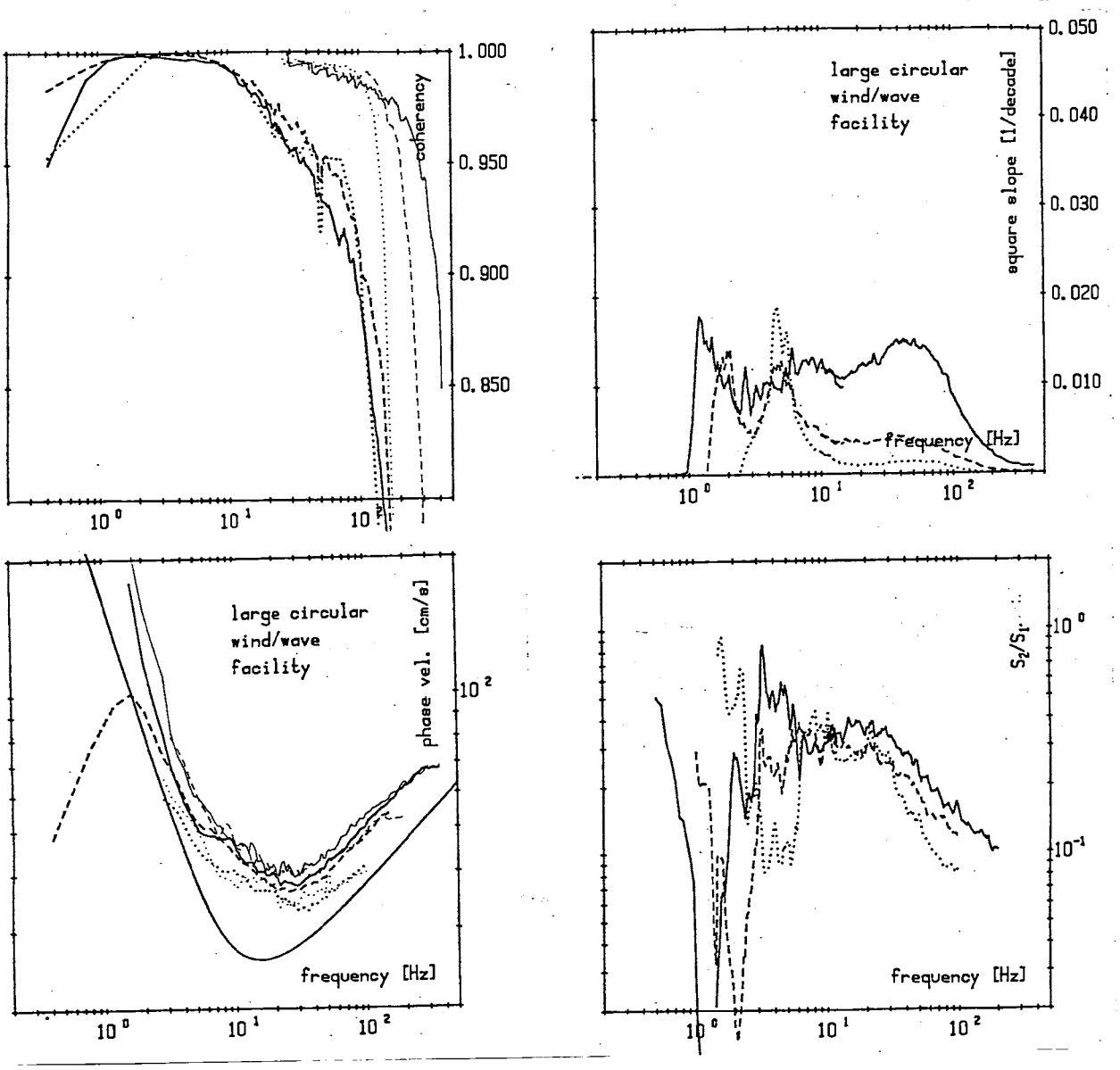

Figure 5.14: Summary of phase speed measurements in the large I.M.S.T. facility including spectral information at 4 m fetch and wind speeds as indicated. The phase speeds corrected for effects of angular dispersion are shown as obtained from the along-wind slope signal.

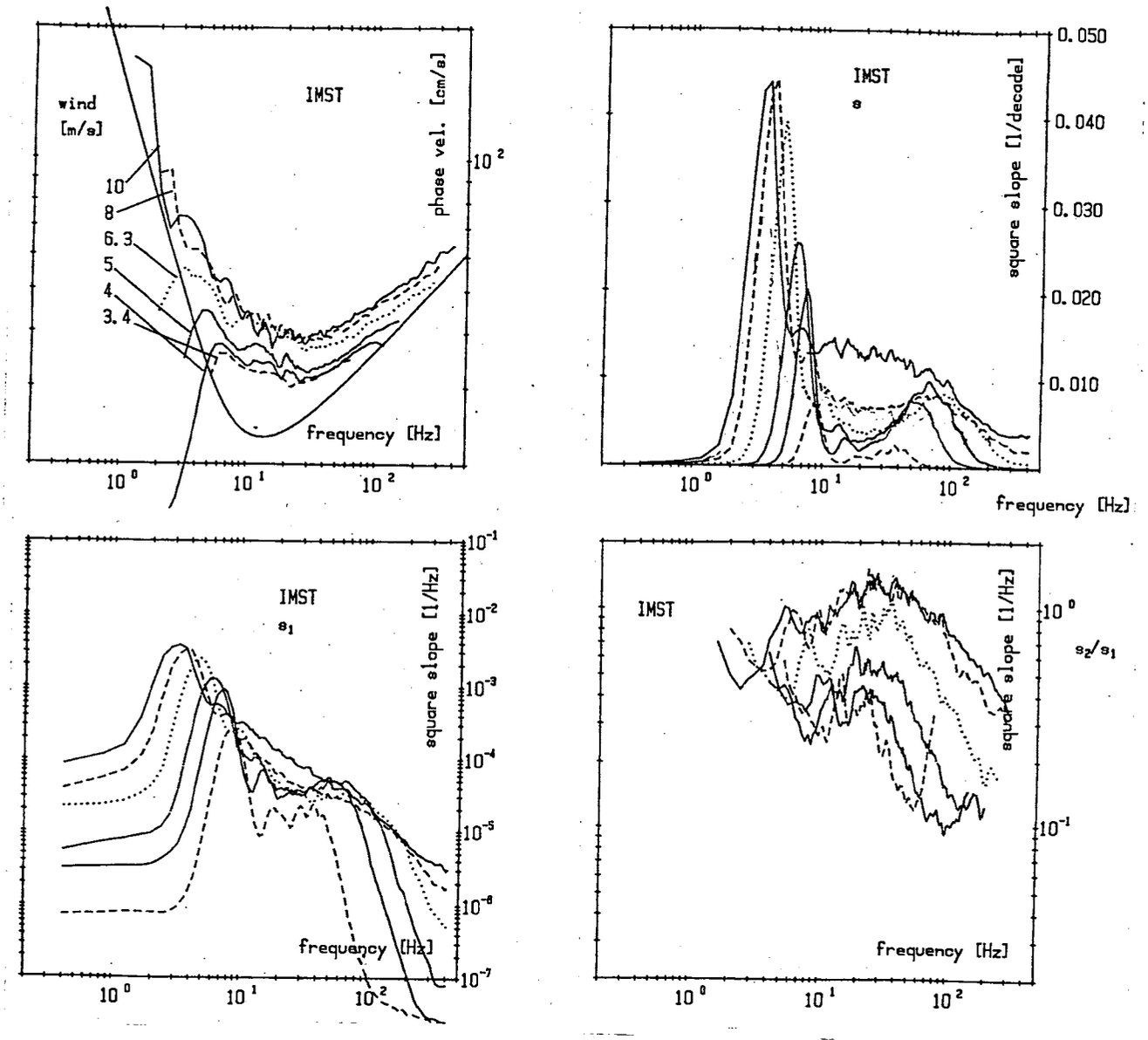

Fig 5.12 shows the results for 4 and 10 m/s wind in the I.M.S.T. facility. At 4 m/s the corrected phase speeds determined from both slope signals agree quite well. The phase speed deviates from the expected dispersion relation for linear waves: It is higher and more or less constant, giving additional support for the fact that the capillary wave are bound at the lee side of the dominant wave. The coherency decrease is mainly caused by the angular dispersion of the waves.

At 10 m/s the situation is quite different. No secondary bump exists in the capillary wave region, and the phase velocities suggest that the capillary waves propagate less strongly bound to gravity waves, since they propagate about 20 - 30 cm/s more slowly than the dominant wave. The measured coherency decrease is much larger than the one calculated caused by angular dispersion. So the coherency decrease is now dominated by the k-spread, likely caused by modulation of the phase speed due to the orbital motion of the dominant wave.

The phase speed determined from the cross-wind slope is considerably lower than the one determined by the along-wind component. This suggests that the proposed cosine angular dispersion function is no longer valid. In fact, wave visualization (next chapter) reveals that a bimodal angular dispersion is more likely given. For such a dispersion function the correction for the cross-wind determined phase speed would be smaller. But the lower phase speed from the cross-wind slope spectra may also be caused by the less strong influence of the surface drift velocity on the cross-wind slope wave components.

A summary of more phase velocity determinations in the large I.M.S.T. facility is shown in Fig. 5.14 together with the corresponding spectra in different presentations. The phase velocities clearly demonstrate the gradual transition from bound to free waves. The general rise of the capillary phase velocities with increasing wind speed is surely caused by the increased surface drift velocity. Taking into account this effect the deviations from the theoretical phase velocities for linear waves is still considerable. The increase of the capillary phase velocity is smaller than predicted and the minimum phase velocities are too high.

Fig. 5.13 shows the results for the homogeneous wave field of the large circular wind-wave tunnel. Apart from the increase of the phase

velocities due to the water drift velocity, the phase velocities follow the linear dispersion relation quite well. This fact emphasizes the random structure of the homogeneous wave field, where waves of different frequencies travel more freely. Further support for this fact comes from the large coherency decrease, which is nearly independent of the wind speed and much higher than calculated from angular dispersion, clearly indicating the considerable modulation of the small waves by the large gravity waves.

5.5 Wave slope visualization

The discussion of the point measuring technique in the previous chapters clearly shows the difficulties to reach insight into the two dimensional wave structure. Even with advanced techniques the information remains "diffuse" as far as the two dimensional structure is concerned. However, if any progress in the understanding of water surface waves and their interaction with near-surface turbulence is to be made, a detailed investigation of the two-dimensionality of the waves is needed.

Photographic techniques to study the waves have been used from the beginning, but were seriously hindered by the difficulty to obtain quantitative information. Now, progress in computer and video technology offers the chance of quantitative image processing at justifiable costs. The first step, however, is the development of an appropriate illumination system.

Figure 5.15: Outline of the wave slope visualization system as used in the large I.M.S.T. wind-wave facility

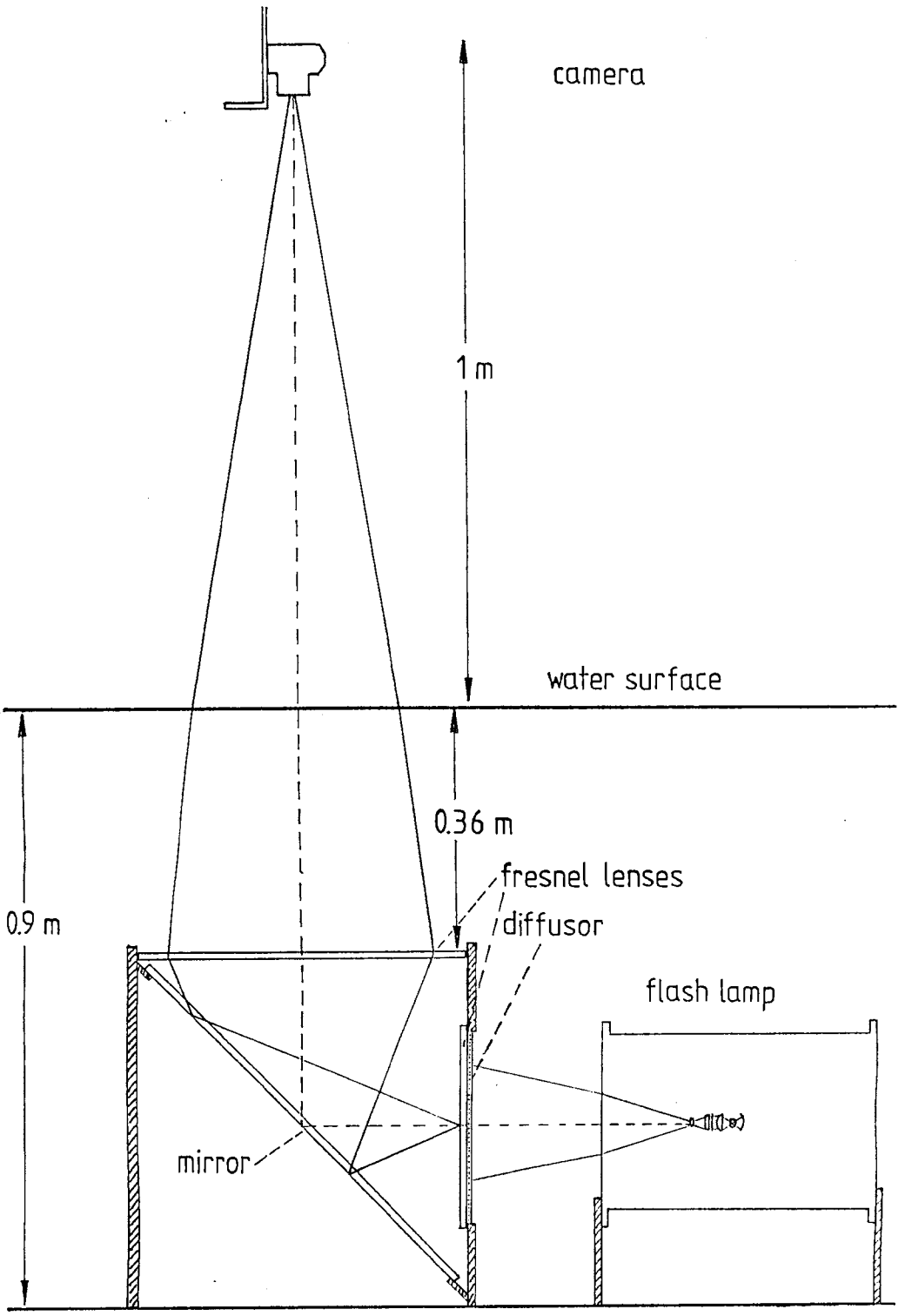

The wave slope visualization technique

Essentially, the same optical geometry is used for the wave visualization as for the spot technique (comp. Fig. 5.4). Fig. 5.15 explains the set up being used in the large wind-wave facility of the I.M.S.T., Marseille. The ray tracing is just reversed compared to the spot technique. Since a position on the diffusion screen represents a certain slope, different lighting (in colour or intensity) indicates a certain slope. The camera at the top of the wind-wave tunnel sees the waves in the corresponding colour or intensity. The performance of the system can easily be tested and calibrated with an artificial sinusoidal wave. It consists of a perspex film forced to a sinusoidal shape by a corresponding frame and put onto the water surface. An area of about 30 to 40 cm can be visualisized in the large I.M.S.T. facility.

Figs. 5.16 to 5.19 show waves photographed with an illumination technique showing the along-wind wave slope in different colours: short fetch (4.6 m) waves (Fig. 5.16) and large fetch (21 m) waves (Fig. 5.17) in large I.M.S.T facility, the temporal growth of the waves in the circular facility at about 6 m/s (Fig. 5.18), and waves at 12 m/s wind speeds in the same tunnel (Fig. 5.19). The pictures need no comment, since they provide a direct picture of to the complex two-dimensionality of the water surface waves, in contrast to the more diffuse information, laboriously derived from point measurements as discussed in the previous chapters.

Potentalities of the wave slope visualization

One may argue that the wave visualization technique were practically worthless, since it were too difficult to obtain quantitative information from the picture. It is the purpose of the following considerations to demonstrate that this is not correct, and that it needs not much more effort to do quantitative analysis of the pictures.

We use an image processing system with a resolution of 512 times 512 pixels and an accuracy of 8 bits, which is integrated into a LSI 11/23 computer system. The pictures are taken with a black and white TV-camera and are digitized in real time into the frame buffer. They can be displayed in pseudo colours on a RGB-monitor and stored on a 40 Mbyte Winchester disk for further processing. Moreover, an U-matic video recorder is used for continuous storage of pictures.

The software development is in progress. So far, the two-dimensional fast Fourier transform programs have been established allowing the calculation of the power and cross spectra of two consecutive 256 times 256 pixel pictures. The analyse of one picture sequence takes 3 minutes. Due to the resolution of 256 pixels in both axes the whole range of the small scale gravity-capillary waves from 5 cm to the high wave number cut off at about 2 mm can be investigated.

The two-dimensional wave number spectra provide much deeper information on the wave properties than the corresponding one-dimensional frequency spectra:
The angular dispersion function of the waves is obtained directly from the two dimensional spectra. The cross-spectral analysis of two consecutive pictures with a temporal separation of τ yields even more detailed information. The phase speed can be derived in amount and direction for every wave vector $\underline{k}$ without any correction terms due to the angular dispersion as with point measurements. From that conclusions can be drawn about the surface drift velocity which in the mean has only an along-wind component. In addition, a decrease in the coherency is only caused by the frequency spread of a wave mit a single wave number $\underline{k}$ and is simply given by

$$Ch(\underline{k}) = 1 - \tau^2 \langle \Delta\omega^2 \rangle + O(\omega\tau^4) \qquad (5.26)$$

This simple relation allows a direct determination of the frequency spread of the waves.

Besides the study of mean spectral parameters, it is also worthwhile to investigate single wave trains. Due to the full information provided it should be possible to study resonant nonlinear wave-wave interaction between capillary-gravity waves and the generation of capillary waves by steep gravity waves in detail. Another big advantage is the high information density of the pictures which makes the study of dynamic processes possible, such as wave generation by wind and decay of the wave field, when the wind speed is stopped. With just one-dimensional sample records in time the statistical errors are too high.
This few remarks show the very promising potentialities of a quantitative analysis of the two-dimensional structure of water surface waves.

Figure 5.16: Photographs of 4.6 m fetch wind waves in the large I.M.S.T wind-wave facility at 6.3 and 8 m/s wind. The sector shown is about 40 times 40 cm. General conditions for all pictures: slope colour key: white means a flat surface, from yellow to red the slope is increasing into wind direction, from green to blue into the opposite direction. The wind is blowing from the left to the right.

Figure 5.17: Photographs of 21 m fetch wind waves in the large I.M.S.T facility at 2.7 and 8.1 m/s wind. The sector shown is 40 times 40 cm.

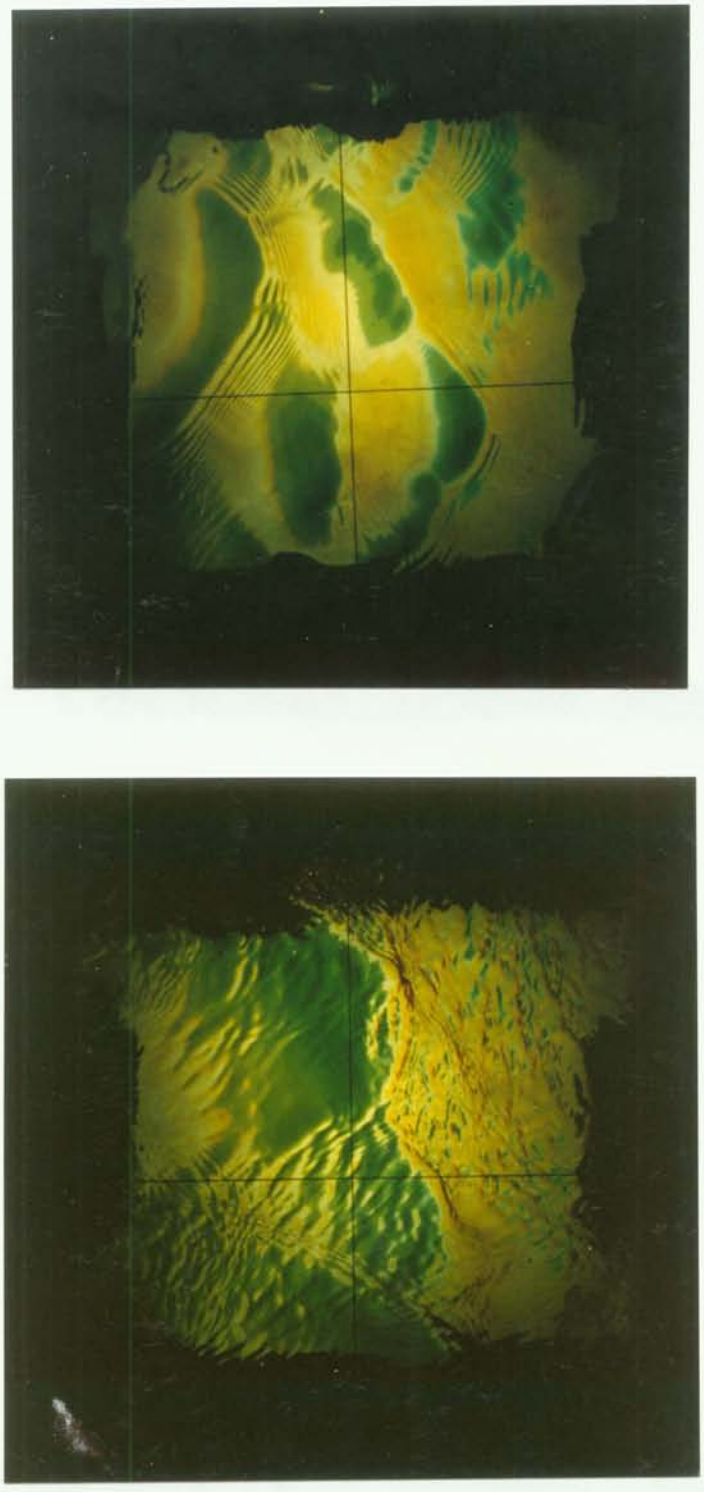

Figure 5.18: Temporal growth of the wave field in the large circular wind-wave tunnel at about 6 m/s. A sector of 20 cm in diameter is shown.

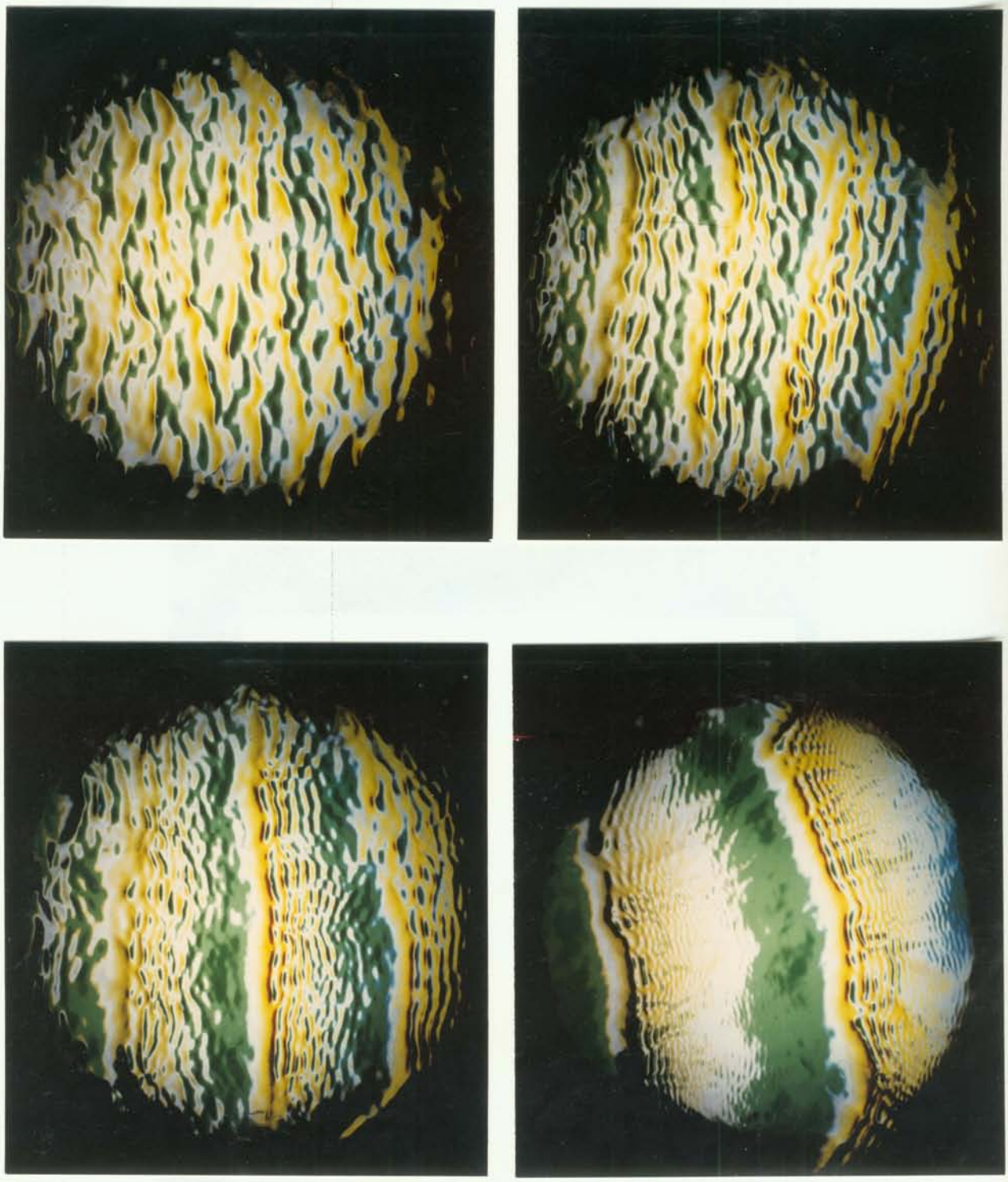

Figure 5.19: Wind waves at 12 m/s in the large circular wind-wave facility; sector: 20 cm in diameter

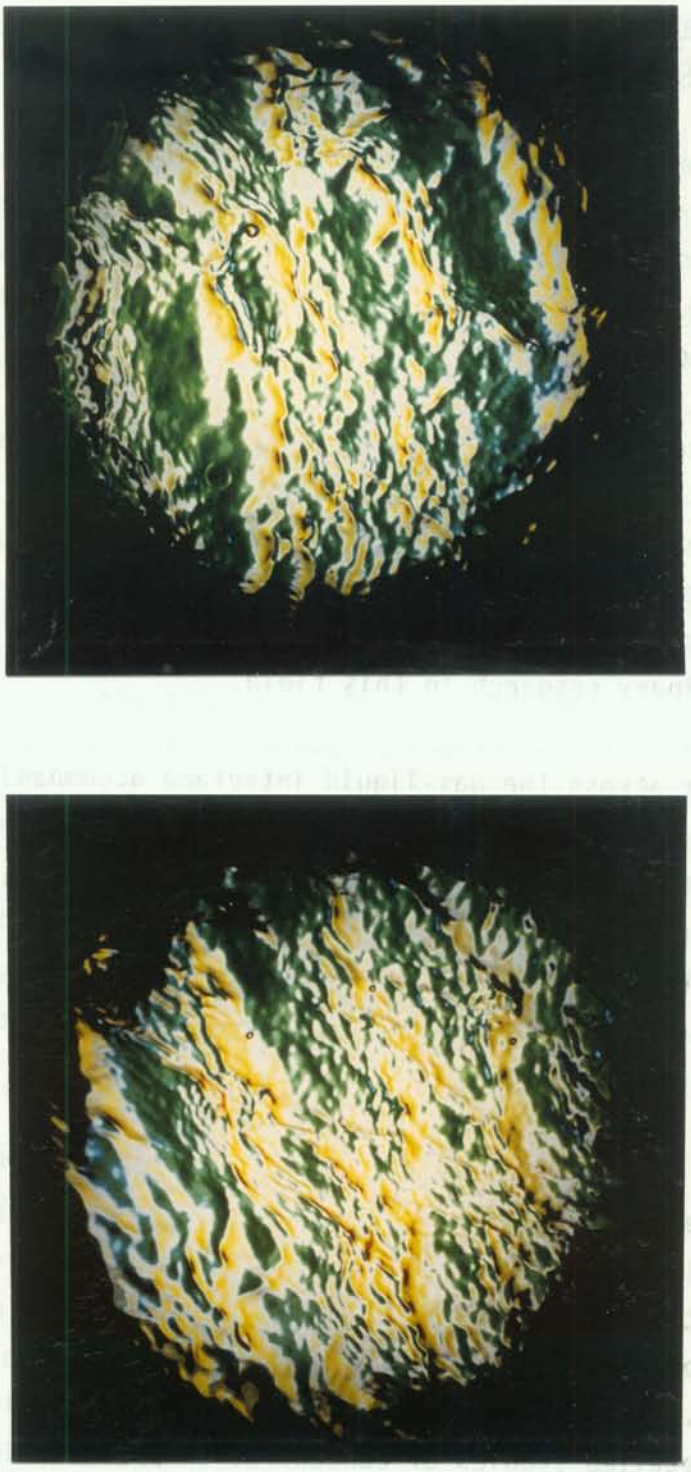

6. VISUALIZATION OF THE MASS TRANSFER PROCESS ACROSS THE AQUEOUS BOUNDARY LAYER

6.1 Mass transfer and chemical reaction: a key to detailed study of the mass transfer boundary layer

From the obvious success of the wave visualization for a detailed study of the waves the question arises, whether it is possible to visualize the mass transfer process across the boundary layer as well. Such a method would provide the missing link to a complete investigation of the aqueous boundary.

At first glance, the realization of such an instrument seems to be impossible, since it cannot be expected that it is possible to measure small gas concentrations in a moving layer of about 50 µm thickness. It is, however, possible to make the transfer process visible via a chemical reaction. This fact, once again, demonstrates the merits of interdisciplinary research in this field.

Mass transfer across the gas-liquid interface accompanied by chemical reaction is a very important branch in chemical engineering (for reviews see for instance Danckwerts (1970) or Brauer (1971)). But despite the extensive research in this field, and a quite well established knowledge about the combined action of mass transfer and chemical reactions, only few attempts have been made to use chemical reaction as a tool to study mass transfer.

To the best of the authors knowledge Hiby (1967 and 1968) was the first to use a fluorescence method for investigating the transport mechanisms in falling films. With this technique he successfully demonstrated that both mean and fluctuating concentrations can be measured. In a later paper the technique was improved (Schwanbom et al. 1971). Braun et al. (1971) used it to measure the surface velocity in falling films and detailed studies of concentration profiles in falling films were carried out (Fahlenkamp, 1979; Hiby, 1983). In addition, Flender and Hiby (1981) investigated the solid/liquid mass transfer with a photometric method. A similar technique was used by Petermann et al. (1978) to study the absorption of gases in fluid films.

These investigations clearly prove that chemical reaction can be used as a key for mass transfer studies across the gas-liquid interface. In the following chapter the basic principle of one method is described, its potentialities and application for wind-wave tunnels are dicussed, and first results are presented.

6.2 Visualization of the mass transfer with the aid of pH-indicators

Conversion of the gas concentration gradient into a pH-gradient

The basic idea of the visualization is the conversion of the gas concentration gradient in the aqueous boundary layer into a pH gradient. This can be achieved by the adsorption of an alkaline gase in an acid liquid or vice versa.

It is a surprising effect that chemical reactions do not make the transport even more complex as long as the time constants of the reactions are faster than the time scale of the transport across the boundary layer. This results from mass conservation. For instance, if a component A reacts with B and produces C during the transport as many moles of A and B disappear as moles of A appear. Consequently, the concentration difference A-B, and A+C and B+C behave like conservatives tracer since concentration changes by reaction are compensated for these concentration combinations.

This basic feature together with reaction equilibria will be used to analyse the absorption of a reactive gas in a liquid. Most hydration reactions of alkaline or acidic gases are so fast that the gas is dissociated at the very surface (exception: CO_2). Consequently, the gas concentration at the water surface is zero and the gas flux density is controlled by the gas-sided transfer velocity

$$j_g = k_g c_g, \tag{6.1}$$

where c_g is the bulk tracer concentration in the gas space. In the following, we shall consider the adsorption of an acidic gas in a base. (Similar considerations are valid for the inverse case.) Two reactions determine the system: First, the acid gas dissociates at the surface

$$HA > H^+ + A^-. \tag{6.2}$$

As long as there are OH^--ions at the surface, the H^+-ions produced are neutralized. This reaction forces an OH^--ion flux from the bulk heading for the surface being equal to the gas flux from the air to the surface (Fig. 6.1a). If the transfer process in the water is too slow to establish the necessary flux density of the OH^--ions for the given concentrations, the surface layer becomes acid, and the H^+-ions diffuse into the bulk towards the OH^--ions (Fig. 6.1b). Since the dissociation reaction takes place only at the surface the only chemical reaction in the boundary layer is the self-dissociation of water

$$OH^- + H^+ \leftrightarrow H_2O \quad \text{with} \quad [OH^-]\,[H^+] = K_W = 10^{-14}\ (\text{mol/l})^2. \tag{6.3}$$

Therefore, the difference concentration $[OH^-]$-$[H^+]$ must behave like a conservative tracer and the following flux density holds in the liquid

$$j_l = k_l\,([OH^-]_s - [OH^-]_w - [H^+]_s + [H^+]_w). \tag{6.4}$$

For sufficiently large alkalinity in the water (pH > 9) practically only H^+- or OH^--ions can exist at a certain depth, because of the equilibrium (6.3), apart from a very thin reaction layer, where OH^-- and H^+-ions neutralize each other. In effect, a $[H^+]$-$[OH^-]$ gradient is established as if a non-reactive gas would be transported through the aqueous boundary layer.

Measurement of the mean concentration profile

The condition for the surface to become neutral ($[OH^-]_s = [H^+]_s \approx 0$) is derived by equalizing the air- and water-sided fluxes (6.1), (6.4)

$$c_{gn} = [OH^-]_l\, k_l/k_g. \tag{6.5}$$

Since the ratio of the transfer velocities in air and water is about 400 for a wavy surface (Fig. 5.1), only low gas concentrations are needed to attain a neutral zone at the surface: with a 10^{-3} molar liquid base 50 ppm gas tracer concentration in the air is sufficient. Such low gas concentrations allow the handling of reactive gases even in the large circular wind-wave facility with an air-space of about 1 m^3. In addition, disturbances of the transfer processes by the reaction heat are ruled out, by keeping the concentrations low.

Figure 6.1: Schematic representation of the adsorption of HCl in NaOH with the two film model. The case of low (a) and high (b) HCl concentrations are shown. The scale of the HCl concentration in air is stretched by a factor 1000.

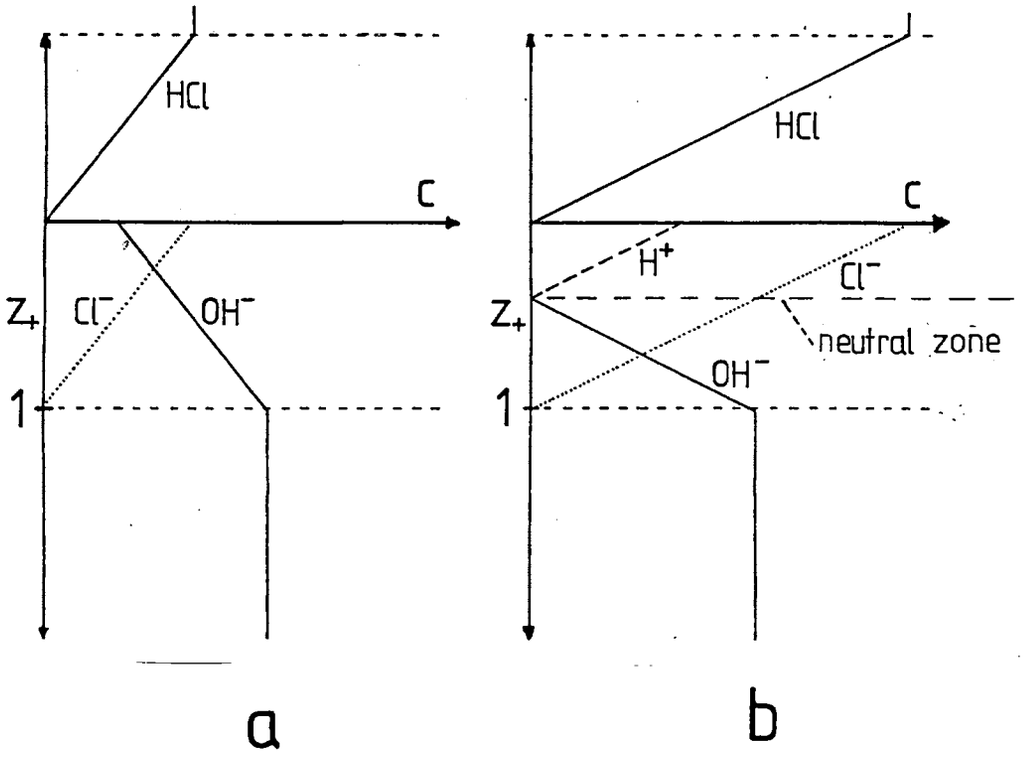

With increasing concentration of the acidic gas in the air, the surface layer becomes acid and the neutral zone moves into the bulk liquid. Now the flux density is given by

$$j_l = k_l \, ([H^+]_s + [OH^-]_l). \tag{6.6}$$

From the surface to the neutral zone the concentration difference is only $[H^+]_s$, so that the fraction

$$c_+(z_n) = [H^+]_s/([H^+]_s+[OH^-]_l) \tag{6.7}$$

of the transport resistance lies between the surface and the neutral zone. (The index n denotes the depth of the neutral zone.) This fraction means nothing else than a dimensionless concentration. For example: if the concentration of the acidic gas in the air is twice the neutralization concentration, the neutral zone lies in a depth to which half of the transport resistance is used.

Generally, the mean concentration profile can be measured from the mean depth of the neutral zone by variation of the concentration of the acidic gas in the air. With (6.5) the dimensionless concentration profile is given by

$$c_+(z_n) = 1 - (k_l/k_g) \, [OH^-]_l/c_l. \tag{6.8}$$

From this equation it is evident that the concentration profile can be determined, if the depth of the neutral zone can be measured. It should be emphasized that the measurement of the concentration profile is a sensitive instrument to distinguish different models of turbulent structure. Fig. 6.2 shows concentration profiles for diffusion and surface renewal models with different Schmidt number exponents n (compare chapter 2.8).

Figure 6.2: Concentration profiles in the mass boundary layer for diffusion models (dashed lines) and surface renewal models (solid lines) for a given Schmidt number exponent as indicated. The concentration is scaled with the concentration difference and the depth with mass boundary layer thickness.

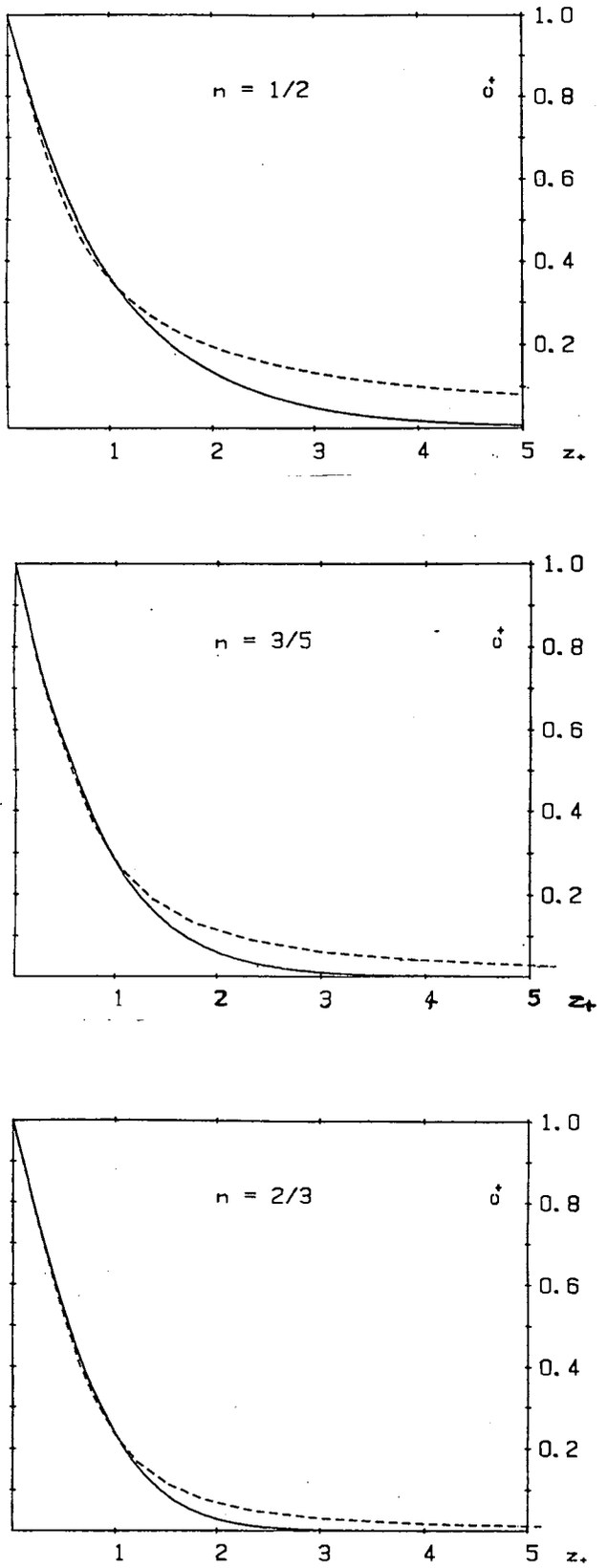

Measurement of the depth of the neutral zone with pH-indicators

A linear change of the concentration difference betwen the OH^-- and H^+-ions with depth means a sudden change of the pH near the neutral zone. So the depth of the neutral zone can be measured with a pH-indicator. Colour indicators are less suitable to detect thin layers. The estimated minimum detectable layer thickness is 50 µm (Jähne, 1983b). Fluorescence indicators are more sensitive. Hiby (1968) reported a sensitivity limit of about only 1 µm. The change of the fluorescence intensity is shown in Fig. 6.3 for indicators with different indicator exponents, clearly demonstrating the sudden change of the fluorescence intensity at the neutral zone.

Nevertheless, the high ratio of the water height to the boundary layer thickness of roughly 1000 to 10000 presents a problem. If there is only a small remaining fluorescence in the bulk, it would easily exceed the intensity from the thin boundary layer. Since the fluorescence is activated by UV-radition onto the water surface from above, this difficulty can be avoided by solving UV-adsorbing chemicals in the water, thus limiting the penetration depth of the UV-radiation to some millimeters.

Figure 6.3: Detection of the thickness of the acid surface layer with fluorescence indicators. Besides the concentration profiles for the ions, the relative fluorescence intensity for two indicators with different exponents pK_I is shown.

Figure 6.4: Absorption of NH_3 in HCl. Both the concentrations of the different components and the relative fluorescence intensity of two indicators are shown as a function of the depth.

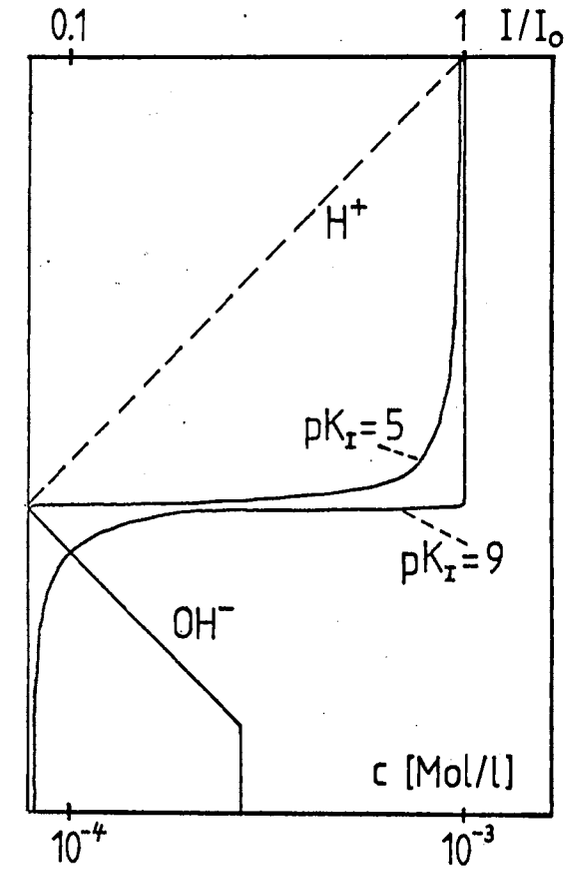

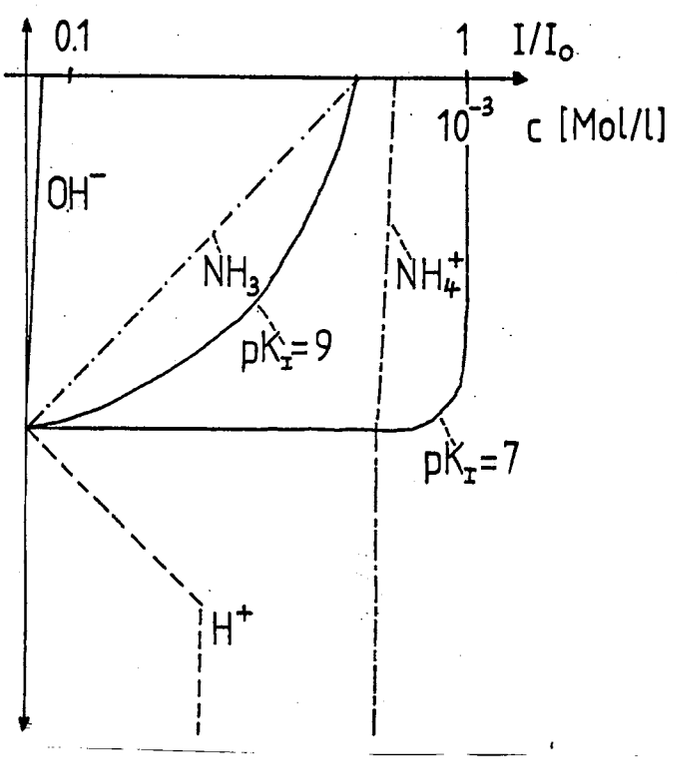

Further potential of the method

Hiby and coworkers used the fluorescence method mainly for point measurements. But from the previous discussion it is evident that its true strength is the investigation of the two-dimensional structure of the mass transfer boundary layer. Quite similar techniques can be used as for the wave visualization: Two dimensional Fourier transformation will provide information about the length scales of the eddies important for the mass transfer process and cross-correlation analysis gives informations on the velocities in the boundary layer. Indeed, it is just the combination of wave and boundary layer visualization which seems to make a powerful tool for the investigation of the boundary layer processes.

First results of the visualization technique

So far, test measurements have been carried out in the small circular wind wave facility. Jähne (1983b) showed that the adsorption of NH_3 in HCl is a suitable tracer pair (Fig. 6.4). A colour pH-indicator was used. The measurements confirmed the theoretical estimates about the necessary concentrations of the reactive gas in air to achieve a change of the pH in the boundary layer. In addition, observations by eye showed that the thickness of the mass boundary layer is modulated by large eddies. So the measurements proved that the visualization techniques can sucessfully be applied in wind-wave tunnels.

At present, the equipment for fluorescence measurements is installed at the large circular wind-wave facility, and the optimal fluorescence indicator is being selected.

7. SUMMARY AND CONCLUSIONS

It is the aim of this thesis to discuss the transfer processes across a free gas-liquid interface.

After some basic considerations, the state of the art presented in the literature is discussed. The only quantities studied so far are mean parameters like the transfer velocity for mass transfer and the friction velocity as a measure for momentum exchange. The discussion of the data obtained shows that this experimental approach is completely insufficient to explain the effects observed, mainly the large enhancement of mass transfer across the aqueous boundary layer for a free surface if compared to a solid one.

Therefore methods providing a deeper insight into the complex transfer mechanisms have been developed. Special emphasize is put on their capabilities and their significance in proving and disproving theoretical concepts:

- the study of the Schmidt number dependence of the mass transfer process, in order to obtain the shape of the turbulence increase at the surface
- a comparison of the Schmidt number dependence and the velocity profile in the boundary layer, leading to a distinction of multi- and single-stage transport models
- the measurement of the local and instantaneous transfer velocity across the boundary layer
- a detailed study of water surface waves including the measurement of the phase speed and the coherency
- the visualization of the surface waves and
- the visualization of the mass transfer across the aqueous boundary layer both providing a direct insight into the two-dimensional structure of the processes.

From the results obtained so far a clearer picture of the exchange processes and the turbulent structure at the free, wavy surface can be drawn already: With the onset of the waves at the free surface a new flow regime is established which has no analogue in flow at a solid surface. Eddies with length scales comparable to the dominant waves

and closely linked to the wave field are an important feature of this structure. Kitaigorodskii's concept (1984) that turbulent patches generated by wave instability cause the enhanced gas exchange rates is in agreement with these findings.

The development of the new methods promises further progress in understanding near-surface transport processes in the liquid.

8. ACKNOWLEDGMENTS

This work would be incomplete without grateful acknowledgment to all people who helped me to carry out this work.

Any experimental work would not be possible without the assistance of the workshops. So I want to thank the staff of the mechanical workshop of the Institut für Umweltphysik, especially Mr. Fletterer. They have taken care of the many small and large technical problems of the large circular wind-wave facility and considerably contributed to its construction and instrumentation. Likewise, I want to thank Mr. Mantsch and his staff for the construction of various electronic equipment, especially the stroboscope for the wave and boundary layer visualization techniques. Thanks are also due to the technical staff of the I.M.S.T., Marseille, who very efficiently helped me to become familiar with this large wind tunnel and also constructed part of the equipment for our wave- and gas exchange experiments.

I would also like to express my gratitude to the students who worked together with me in the last eight years. Their names can be found in the list of the theses of the wind tunnel group.

I would like to thank Prof. Coantic and Dr. Ramamonjiarisoa for the many stimulating discussions they had with me during my research visit at the I.M.S.T., Marseille.

I owe much to Prof. Münnich who encouraged me to do this work, supported me generously, and gave me much freedom in which to develop my own research. I would like to thank him cordially. To all other people who contributed in one way or another and whom I cannot all mention by name, I likewise offer my sincere thanks.

Moreover, I gratefully acknowledge financial support from the following organisations: The Deutsche Forschungsgemeinschaft (German Science Foundation), the NATO Air-Sea-Interaction Panel, and the C.N.E.X.O., Paris.

But what scientific discoveries would have been made, if not ideas, questions, or concepts arised from a helpful intuition at the right

moment? - They are the base from which a man with a scientific consciousness can work on with staying power and without presumptions, even if he goes new ways. So I gratefully and humbly acknowledge the substantial help of several dreams knowing that everybody owes his ideas to God according to the dream statement: Keep in mind that God has to do with everything and everybody (Dorn, 1982).

An honest and unprejudiced (i.e. a truly scientific) review of the development of ideas is a continuous proof of the above dream statement. I would like to mention just one example of my own experience:

Long before I realized the importance to study the two-dimensional structure of waves, I had a dream in which I was carrying out wave measurements with laser slope gauges in the large I.M.S.T. wind-wave facility. Contrary to my expectation the measurements only yielded diffuse results and I started wave visualization measurements. - This dream triggered the development of the wave visualization technique, which my consciousness, without this dream, regarded as less important.

As a matter of fact, any scientific progress depends on such helpful intuition.

9. REFERENCES

Banner, M. L. and O. M. Phillips, On the incipient breaking of small scale waves, J. Fluid Mech., 65, 647-656, 1974

Bösinger, R., Gasaustauschmessungen in einem großen ringförmigen Windkanal, Diplomarbeit, Institut für Umweltphysik der Universität Heidelberg, 1985 (in Vorbereitung)

Brauer, H., Stoffaustausch einschließlich chemischer Reaktionen, Sauerländer, Aarau, 1971

Braun, D., H. Eckstein und J. W. Hiby, Messung der Oberflächengeschwindigkeit von Rieselfilmen, Chem.-Ing.-Techn., 43, 324-329, 1971

Broecker, H.-C., J. Petermann, and W. Siems, The influence of wind on CO_2-exchange in a wind-wave tunnel, including the effects of monolayers, J. Marine Res., 36, 595-610, 1978

Broecker, H.-C., L. Hasse, eds., Symposium on capillary waves and gas exchange, Berichte aus dem Sonderforschungsbereich 94 "Meeresforschung", Universität Hamburg, Heft Nr. 17, 1980

Coantic, M., A model of gas transfer across air-water interfaces with capillary waves, 1985 (in preparation)

Cohen, Y., W. Cocchio, and D. Mackay, Laboratory study of liquid-phase volatilization rates, Environ. Sci. Technol., 12, 553-558, 1978

Cox, C. S., Measurements of slopes of waves, J. Marine Res., 16, 199-230, 1958

Danckwerts, P. V., Significance of liquid-film coefficients in gas absorption, Industrial and Engineering Chemistry, 43, 1460-1467, 1951

Danckwerts, P. V., Gas-liquid reactions, McGraw-Hill, New York, 1970

Deacon, E. L., Gas transfer to and across an air-water interface, Tellus, 29, 363-374, 1977

Dietrich, W., Aufbau und Erprobung eines neuartigen Diaphragmaverfahrens zur Messung der Diffusionskonstanten von in Wasser gelösten Gasen, Diplomarbeit, Institut für Umweltphysik der Universität Heidelberg, 1983

Dorn, S., Halt fest, daß Gott mit allem und jedem zu tun hat, edited by W. Dorn and A. Erdmann, 1982
(French edition: Retiens que Dieu a affaire à tout et à chacun, 1985, in preparation)

Dudis, J. J., Interpretation of phase velocity measurements of wind generated surface waves, J. Fluid Mech., 113, 241-249, 1981

Dutzi, A., Untersuchungen zum Einfluß der Temperatur auf den Gasaustausch, Diplomarbeit, Institut für Umweltphysik der Universität Heidelberg, 1985

Fahlenkamp, H., Zum Mechanismus des Stofftransports im laminar-welligen Rieselfilm, Dissertation, Technische Hochschule Aachen, Fakultät für Maschinenwesen, 1979

Flender, J. F. and J. W. Hiby, Investigation of solid/liquid mass transfer by a photometric method, Ger. Chem. Eng., 4, 370-379, 1981

Flothmann, D., E. Lohse, and K. O. Münnich, Gas exchange in a circular wind/water tunnel, Naturwissenschaften, 66, 49-50, 1979

Hasse, L. and P. S. Liss, Gas exchange across the air-sea interface, Tellus, 32, 470-481, 1980

Hasselmann, K., On the non-linear energy transfer in a gravity-wave spectrum, part I, general theory, J. Fluid Mech., 12, 481-500, 1962

Hasselmann, K., Weak interaction theory of ocean waves, Basic Developments in Fluid Dynamics, 2, Academic Press, 117-182, 1968

Heinz, G., Messung der Diffusionskonstanten von in Wasser gelösten Gasen mit einem modifizierten Barrerverfahren, Diplomarbeit, Institut für Umweltphysik der Universität Heidelberg, 1985 (in Vorbereitung)

Hiby, J. W., D. Braun und K. H. Eickel, Eine Fluoreszenzmethode zur Untersuchung des Stoffübergangs bei der Gasabsorption im Rieselfilm, Chemie-Ing.-Techn., 39, 297-301, 1967

Hiby, J. W., Eine Fluoreszenzmethode zur Untersuchung des Transport-mechanismus bei der Gasabsorption im Rieselfilm, Wärme- und Stoffübertr., 1, 105-116, 1968

Hiby, J. W., The chemical indicator: a tool for the investigation of concentration fields in liquids, Ann. N. Y. Acad. Sci., 404, 348-349, 1983

Higbie, R., The rate of absorption of a pure gas into a still liquid during short periods of exposure, Trans. A. I. Ch. E., 31, 365-389, 1935

Huang, N. E., Comment on 'modulation characteristics of sea surface waves' by A. Ramamonjiarisoa and E. Mollo-Christensen, J. Geophys. Res., 86, 2073-2075, 1981

Hubbard, D. W. and E. N. Lightfoot, Correlation of heat and mass transfer data for high Schmidt and Reynolds numbers, Ind. Eng. Chem. (Fund.), 5, 370, 1966

Huber, W., Aufbau eines gaschromatographischen Meßsystems für Gas-austauschmessungen; Windkanalmessungen zur Schmidtzahl- und Wellenbildabhängigkeit des Gasaustausches, Diplomarbeit, Institut für Umweltphysik der Universität Heidelberg, 1984

Hughes, B. A., H. L. Grant, and R. W. Chappell, A fast response surface-wave slope meter and measured wind-waves moments, Deep-Sea Res., 24, 1211-1223, 1977

Ilmberger, J., Impulsübertrag und Strömungsverhältnisse in einem runden Wind-Wasser Kanal, Diplomarbeit, Institut für Umweltphysik der Universität Heidelberg, 1980

Jähne, B., K. O. Münnich, and U. Siegenthaler, Measurements of gas exchange and momentum transfer in a circular wind-water tunnel, Tellus, 31, 321-329, 1979

Jähne, B., Zur Parameterisierung des Gasaustausches mit Hilfe von Laborexperimenten, Dissertation, Institut für Umweltphysik der Universität Heidelberg, 1980

Jähne, B., Trockene Deposition von Gasen über Wasser (Gasaustausch), Austausch von Luftverunreinigungen an der Grenzfläche Atmosphäre / Erdoberfläche (trockene Deposition), D. Flothmann, ed., Battelle Institut Frankfurt am Main, BleV-R-64.284-2, 1982

Jähne, B., Optical water wave measuring techniques, paper presented at "International symposium on gas transfer at water surfaces", Cornell University, Ithaca, NY, June 1983a

Jähne, B., Messung des Gasaustausches und der Turbulenz an der Oberfläche durch Sichtbarmachung der Grenzschicht, Report, Institut für Umweltphysik der Universität Heidelberg, 1983b

Jähne, B., W. Huber, A. Dutzi, T. Wais, and J. Ilmberger, Wind/wave-tunnel experiments on the Schmidt number and wave field dependence of air-water gas exchange, in: "Gas transfer at water surfaces", W. Brutsaert and G. H. Jirka, eds., Reidel, Dordrecht, 303-309, 1984a

Jähne, B., K. H. Fischer, J. Ilmberger, P. Libner, W. Weiss, O. Imboden, U. Lemnin, and J. M. Jaquet, Parameterization of air/lake gas exchange, in: "Gas transfer at water surfaces", W. Brutsaert and G. H. Jirka, eds., Reidel, Dordrecht, 459-466, 1984b

Jähne, B., Phase speed and angular dispersion of wind waves as determined with an optical slope gauge, 1985 (in preparation)

Jähne, B., T. Wais, L. Memery, G. Gaulliez, L. Merlivat, K. O. Münnich, and M. Coantic, He and Rn gas exchange experiments in the large wind-wave facility of I.M.S.T., accepted by J. Geophys. Res., 1985a

Jähne, B., P. Libner, E. J. Plate, and R. Friedrich, A new, fast and locally measuring method to study mass transfer processes across the free aqueous viscous boundary layer, 1985b (in preparation)

Jones, E. P. and S. D. Smith, A first measurement of sea-air CO_2 flux by eddy correlation, J. Geophys. Res., 82, 5990-5992, 1977

Kerman, B. R., A model of interfacial gas transfer for a well-roughened sea, J. Geophys. Res., 89, 1439-1446, 1984

King, C. J., Ind. Eng. Chem. (Fund.), 5, 1, 1966

Kinsman, B., wind waves, their generation and propagation on the ocean surface, Prentice-Hall, Englewood Cliffs, N. J., 1965

Kitaigorodskii, S. A., On the theory of the equilibrium range in the spectrum of wind-generated gravity waves, J. Phys. Oceanogr., 13, 816-827, 1983

Kitaigorodskii, S. A., On the fluid dynamical theory of turbulent gas transfer across an air-sea interface in the presence of breaking wind-waves, J. Phys. Oceanogr., 14, 960-972, 1984

Komen, G. J., Spatial correlations in wind generated water waves, J. Geophys. Res., 85, 3311-3314, 1980

Kondo, J., Parameterization of turbulent transport in the top meter of the ocean, J. Phys. Oceanogr., 6, 712-720, 1976

Kromer, B. and W. Roether, Field measurements of air-sea gas exchange by the radon deficit method during JASIN 1978 and FGGE 1979, Meteor Forsch. Erg. A/B, 24, 55-75, 1983

Lange, P. A., B. Jähne, J. Tschiersch, and J. Ilmberger, Comparison between an amplitude-measuring wire and a slope-measuring laser water wave gauge, Rev. Sci. Instrum., 53, 651-655, 1982

Ledwell, J. R., Gas exchange across the air-water interface, Ph.-D.-thesis, Harvard University, Cambridge, 1982

Ledwell, J. R., The variation of the gas transfer coefficient with molecular diffusity, in: "Gas transfer at water surfaces", W. Brutsaert and G. H. Jirka, eds., Reidel, Dordrecht, 293-302, 1984

Liss, P. S., Processes of gas exchange across an air-water interface, Deep-Sea Res., 20, 221-238, 1973

Liss, P. S. and P. G. Slater, Flux of gases across the air/sea interface, Nature, 247, 181-184, 1974

Liss, P. S., P. W. Balls, F. N. Martinelli, and M. Coantic, The effect of evaporation and condensation on gas transfer across an air-water interface, Oceanol. Acta, 4, 129-138, 1981

Liu, H. T., K. B. Katsaros, and M. A. Weissman, Dynamic response of thin-wire wave gauges, J. Geophys. Res., 87, 5686-5698, 1982

Long, S. R. and N. E. Huang, On the variation and growth of wave-slope spectra in the capillary-gravity range with increasing wind, J. Fluid Mech., 77, 209-228, 1976

Mackay, D. and A. T. K. Yeun, Mass transfer coefficient correlations for volatilization of organic solutes from water, Environ. Sci. Technol., 17, 211-217, 1983

Mai ß , M., Modelluntersuchungen zum Einfluß von Blasen auf den Gasaustausch zwischen Atmosphäre und Meer, Diplomarbeit, Institut für Umweltphysik der Universität Heidelberg, 1985 (in Vorbereitung)

McCready, M. J., Mechanisms of gas absorption at a sheared gas-liquid interface, thesis, University of Illinois, 1984

McCready, M. J. and T. J. Hanratty, A comparison of turbulent mass transfer at gas-liquid and solid-liquid interfaces, in: "Gas

transfer at water surfaces", W. Brutsaert and G. H. Jirka, eds., Reidel, Dordrecht, 283-292, 1984

McGoldrick, L. F., Resonant interactions among capillary-gravity waves, J. Fluid Mech., 21, 305-331, 1965

McLeish, W. L. and G. E. Putland, The initial water circulation and waves induced by an airflow, NOAA Technical Report, ERL 316-AOML16, 1975

Merlivat, L., L. Memery, Gas exchange across an air-water interface: experimental results and modeling of bubble contribution to transfer, J. Geophys. Res., 88, 707-724, 1983

Mizushina, T., F. Ogino, Y. Oka, and N. Fukuda, Turbulent heat and mass transfer between wall and fluid streams of large Prandtl and Schmidt numbers, Int. J. Heat Mass Transfer, 14, 1705, 1971

Monin, A. S. and A. M. Yaglom, Statistical fluid mechanics, Mechanics of turbulence, Vol. 2, MIT Press, Cambridge, 1975

Müller, W., Die Diffusions-, Löslichkeits- und Permeabilitäts-Koeffizienten von ^{222}Rn in handelsüblichen Kunststoffen, Staatsexamensarbeit, Institut für Umweltphysik der Universität Heidelberg, 1978

Münnich, K. O. and D. Flothmann, Gas exchange in relation to other air-sea interaction phenomena, SCOR Workshop on "Air/sea Interaction Phenomena", Miami, Dec. 8th-12th, 1975

Münnich, K. O., W. B. Clarke, K. H. Fischer, D. Flothmann, B. Kromer, W. Roether, U. Siegenthaler, Z. Top, and W. Weiss, Gas exchange and evaporation studies in a circular wind tunnel, continuous radon-222 measurements at sea, and tritium, helium-3 measurements in a lake, in: "Turbulent fluxes through the sea surface, wave dynamics, and prediction", A. Favre, K. Hasselmann, eds., Plenum Press, 1978

O'Connor, D. J., Wind effects on gas-liquid transfer coefficients, J. Environ. Eng., 109, 731-752, 1983

O'Connor, D. J., Turbulent transfer across smooth and rough surfaces, in: "Gas transfer at water surfaces", W. Brutsaert and G. H. Jirka, eds., Reidel, Dordrecht, 321-331, 1984

Okuda, K., S. Kawai, M. Tokuda, and Y. Toba, Detailed observation of the wind-exerted surface flow by use of flow visualization methods, J. Oceanogr. Soc. Japan, 32, 53-64, 1976

Peng, T.-H., W. S. Broecker, G. G. Mathieu, and Y.-H. Li, A. E. Bainbridge, Radon evasion rates in the Atlantic and Pacific oceans as determined during the GEOSECS program, J. Geophys. Res., 84, 2471-2486, 1979

Petermann, J., H.-C. Broecker, and H. Sinn, A spectroscopic method for investigating the absorption of gases in fluid films, Ger. Chem. Eng., 1, 312-317, 1978

Phillips, O. M., The equilibrium range in the spectrum of wind-generated waves, J. Fluid Mech., 4, 426-434, 1958

Phillips, O. M., Strong interactions in wind-wave fields, in: "Turbulent fluxes through the sea surface, wave dynamics, and prediction", A. Favre, K. Hasselmann, eds., Plenum Press, 373-384, 1978

Phillips, O. M., The dynamics of the upper ocean, Cambridge University Press, 3. edition, 336 pp., 1980

Phillips, O. M., The dispersion of short wavelets in the presence of a dominant long wave, J. Fluid Mech., 107, 465-485, 1981

Plate, E. J. and R. Friedrich, Reaeration of open channel flow, in: "Gas transfer at water surfaces", W. Brutsaert and G. H. Jirka, eds., Reidel, Dordrecht, 333-346, 1984

Ramamonjiarisoa, A. and E. Mollo-Christensen, Modulation characteristics of sea surface waves, J. Geophys. Res., 84, 7769-7775, 1979

Reece, A. M., Modulation of short waves by long waves, Boundary-Layer Meteorol., 13, 203-214, 1978

Roether, W., Field measurement of air-sea gas exchange: a methodical search, Boundary-Layer Meteorol., 27, 97-103, 1983

Roether, W. and B. Kromer, Optimum application of the radon deficit method to obtain air-sea gas exchange rates, in: "Gas transfer at water surfaces", W. Brutsaert and G. H. Jirka, eds., Reidel, Dordrecht, 447-457, 1984

Schoder, M., Messung der Transfergeschwindigkeit des Gasaustausches durch Blasenoberflächen, Staatsexamensarbeit, Institut für Umweltphysik der Universität Heidelberg, 1984

Schwanbom, E. A., D. Braun, E. Hamann, and J. W. Hiby, A double-ray technique for the investigation of liquid boundary layers, Int. J. Heat Mass Transfer, 14, 996-998, 1971

Shaw, D. A. and T. J. Hanratty, Turbulent mass transfer rates to a wall for large schmidt numbers, A. I. Ch. E. J., 23, 28-37, 1977

Shemdin, O. H., Modulation of centimetric waves by long gravity waves: progress report on field and laboratory results, in: "Turbulent fluxes through the sea surface, wave dynamics, and prediction", A. Favre, K. Hasselmann, eds., Plenum Press, 235-255, 1978

Sheriff, N. and P. Gumley, Heat-transfer and friction properties of surfaces with discrete roughnesses, Int. J. Heat Mass Transfer, 9, 1297-1320, 1966

Siems, W., Modelluntersuchungen zur Verdunstung und zum Gasaustausch zwischen Wasser und Luft. Der Einfluß von Wellen und Oberflächenverunreinigungen, Dissertation, Universität Hamburg, 1980

Sivakumar, M., Reaeration and wind induced turbulence shear in a contained water body, in: "Gas transfer at water surfaces", W. Brutsaert and G. H. Jirka, eds., Reidel, Dordrecht, 369-377, 1984

Smith, S. D. and E. P. Jones, Evidence for wind-pumping of air-sea gas exchange based on direct measurements of CO_2-fluxes, J. Geophys. Res., 90, 869-875, 1985

Sturm, G. V. and F. Y. Sorrell, Optical wave measurement technique and experimental comparison with conventional wave height probes, Appl. Optics, 12, 1928-1933, 1973

Toba, Y., M. Tokuda, K. Okuda, and S. Kawai, Forced convection accompanying wind waves, J. Oceanogr. Soc. Japan, 31, 192-198, 1975

Torgersen, T., Z. Top, W. B. Clarke, W. J. Jenkins, and W. S. Broecker, A new method for physical limnology - tritium/helium-3 ages - results from Lakes Erie, Huron, and Ontario, Limnol. and Oceanog., 22, 181-193, 1977

Torgersen, T., G. Mathieu, R. H. Hesslein, and W. S. Broecker, Gas exchange dependency on diffusion coefficient: Direct ^{222}Rn and ^{3}He comparisons in a small lake, J. Geophys. Res., 87, 546-556, 1982

Tschiersch, J., Optische Messung von Kapillarwellen im Hinblick auf den Gasaustausch, Diplomarbeit, Institut für Umweltphysik der Universität Heidelberg, 1980

Weißer, F., Verdunstungsmessungen in einem ringförmigen Wind-Wasser-Kanal mit Hilfe von Psychrometern und einem WLD-System, Diplomarbeit, Institut für Umweltphysik der Universität Heidelberg, 1980

Wesely, M. L., D. R. Cook, R. L. Hart, and R. M. Williams, Air-sea exchange of CO_2 and evidence for enhanced upward fluxes, J. Geophys. Res., 87, 8827-8832, 1982

Whitman, W. G., The two-film theory of gas absorption, Chemical and Metallurgical Eng., 29, 146-148, 1923

Witting, J., Effects of plane progressive irrotational waves on thermal boundary layers, J. Fluid Mech., 50, 321-334, 1971

10. LIST OF OWN PUBLICATIONS AND THESES OF THE WIND TUNNEL GROUP

10.1 Own publications (in chronological order)

Jähne, B., Gaschromatographische Tritiumanreicherung; Trennung der Wasserstoffisotope bei Adsorption, Diplomarbeit, Institut für Umweltphysik der Universität Heidelberg, 1977

Jähne, B., K. O. Münnich, and U. Siegenthaler, Measurements of gas exchange and momentum transfer in a circular wind-water tunnel, Tellus, 31, 321-329, 1979

Jähne, B. and K. O. Münnich, Momentum induced gas exchange through a smooth water surface, models and experimental results from linear and circular wind-water tunnels, in: "Symposium on capillary waves and gas exchange", H.-C. Broecker and L. Hasse, eds., Berichte aus dem Sonderforschungsbereich 94 "Meeresforschung", Universität Hamburg, Heft Nr. 17, 55-62, 1980

Tschiersch, J. and B. Jähne, Gas exchange through a rough water surface in a circular wind tunnel; wave characteristics under limited and unlimited fetch; preliminary results, in: "Symposium on capillary waves and gas exchange", H.-C. Broecker and L. Hasse, eds., Berichte aus dem Sonderforschungsbereich 94 "Meeresforschung", Universität Hamburg, Heft Nr. 17, 63-70, 1980

Jähne, B. and U. Siegenthaler, The influence of surface tension on gas exchange: measurements of gas exchange with alcohol/water mixtures in a circular wind-water tunnel, in: "Symposium on capillary waves and gas exchange", H.-C. Broecker and L. Hasse, eds., Berichte aus dem Sonderforschungsbereich 94 "Meeresforschung", Universität Hamburg, Heft Nr. 17, 103-108, 1980

Jähne, B., Zur Parameterisierung des Gasaustausches mit Hilfe von Laborexperimenten, Dissertation, Institut für Umweltphysik der Universität Heidelberg, 1980

Lange, P. A., B. Jähne, J. Tschiersch, and J. Ilmberger, Comparison between an amplitude-measuring wire and a slope-measuring laser water wave gauge, Rev. Sci. Instrum., 53, 651-655, 1982

Jähne, B., Trockene Deposition von Gasen über Wasser (Gasaustausch), Austausch von Luftverunreinigungen an der Grenzfläche Atmosphäre / Erdoberfläche (trockene Deposition), D. Flothmann, ed., Battelle Institut Frankfurt am Main, BleV-R-64.284-2, 1982

Jähne, B., Optical water wave measuring techniques, paper presented at "International symposium on gas transfer at water surfaces", Cornell University, Ithaca, NY, June 1983a

Jähne, B., Messung des Gasaustausches und der Turbulenz an der Oberfläche durch Sichtbarmachung der Grenzschicht, Report, Institut für Umweltphysik der Universität Heidelberg, 1983b

Jähne, B., W. Huber, A. Dutzi, T. Wais, and J. Ilmberger, Wind/wave-tunnel experiments on the Schmidt number and wave field dependence of air-water gas exchange, in: "Gas transfer at water surfaces", W. Brutsaert and G. H. Jirka, eds., Reidel, Dordrecht, 303-309, 1984a

Jähne, B., K. H. Fischer, J. Ilmberger, P. Libner, W. Weiss, D. Imboden, U. Lemnin, and J. M. Jaquet, Parameterization of air/lake gas exchange, in: "Gas transfer at water surfaces", W. Brutsaert and G. H. Jirka, eds., Reidel, Dordrecht, 459-466, 1984b

Jähne, B., T. Wais, and M. Barabas, A new optical bubble measuring device; a simple model for bubble contribution to gas exchange, in: "Gas transfer at water surfaces", W. Brutsaert and G. H. Jirka, eds., Reidel, Dordrecht, 237-246, 1984c

Jähne, B., T. Wais, L. Memery, G. Gaulliez, L. Merlivat, K. O. Münnich, and M. Coantic, He and Rn gas exchange experiments in the large wind-wave facility of I.M.S.T., accepted by J. Geophys. Res., 1985a

Jähne, B., P. Libner, E. J. Plate, and R. Friedrich, A new, fast and locally measuring method to study mass transfer processes across the free aqueous viscous boundary layer, 1985b (in preparation)

Jähne, B., Phase speed and angular dispersion of wind waves as determined with an optical slope gauge, 1985 (in preparation)

Jähne, B., A simple model for bubble contribution to air-sea gas transfer, in preparation

10.2 Theses of the wind tunnel group (in chronological order)

Tschiersch, J., Optische Messung von Kapillarwellen im Hinblick auf den Gasaustausch, Diplomarbeit, 1980

Weißer, F., Verdunstungsmessungen in einem ringförmigen Wind-Wasser-Kanal mit Hilfe von Psychrometern und einem WLD-System, Diplomarbeit, 1980

Ilmberger, J., Impulsübertrag und Strömungsverhältnisse in einem runden Wind-Wasser Kanal, Diplomarbeit, 1980

Bönisch, K., Gasaustausch und Wärmetransfer bei freier Konvektion und unter Einfluß von Wellen; Aufbau einer Apparatur und erste Ergebnisse, Staatsexamensarbeit, 1981

Wais, T., Aufbau eines optischen Verfahrens zur Messung von Gasblasen in Wasser; Einfluß von Gasblasen auf den Gasaustausch, Diplomarbeit, 1983

Dietrich, W., Aufbau und Erprobung eines neuartigen Diaphragma-verfahrens zur Messung der Diffusionskonstanten von in Wasser gelösten Gasen, Diplomarbeit, 1983

Schoder, M., Messung der Transfergeschwindigkeit des Gasaustausches durch Blasenoberflächen, Staatsexamensarbeit, 1984

Huber, W., Aufbau eines gaschromatographischen Meßsystems für Gas-austauschmessungen; Windkanalmessungen zur Schmidtzahl- und Wellenbildabhängigkeit des Gasaustausches, Diplomarbeit, 1984

Libner, P., Entwicklung eines optischen Systems zur Erfassung von Wellenparametern bei Feldmessungen im Hinblick auf den Gasaustausch, Diplomarbeit, 1984

Dutzi, A., Untersuchungen zum Einfluß der Temperatur auf den Gasaustausch, Diplomarbeit, 1985

Barabas, M., Aufbau und Weiterentwicklung von optischen Verfahren zur Messung von Gasblasen in Wasser; Messungen von Blasendichtespektren in Windkanälen in Marseille und Heidelberg, Diplomarbeit, 1985

Bösinger, R., Gasaustauschmessungen in einem großen ringförmigen Windkanal, Diplomarbeit, 1985 (in Vorbereitung)

Heinz, G., Messung der Diffusionskonstanten von in Wasser gelösten Gasen mit einem modifizierten Barrerverfahren, Diplomarbeit, 1985 (in Vorbereitung)

Maiß, M., Modelluntersuchungen zum Einfluß von Blasen auf den Gasaustausch zwischen Atmosphäre und Meer, Diplomarbeit, 1985 (in Vorbereitung)

Ilmberger, J., Zur Parameterisierung des Gasaustausches und der Wellen in Seen, Dissertation, 1985 (in Vorbereitung)

Libner, P., Labor- und Feldmessungen der Austauschprozesse durch die wasserseitige viskose Grenzschicht mit Hilfe einer neuen Infrarotmethode, Dissertation, in Vorbereitung

Huber, W., Visualisierung der Mechanismen des Gasaustausches an einer wellenbewegten Wasseroberfläche, Dissertation, in Vorbereitung